

The role of FAM134B for intracellular organelle architecture and axon function

Dissertation

zur Erlangung des akademischen Grades

doctor rerum naturalium (Dr. rer. nat.)

**vorgelegt dem Rat der Medizinischen Fakultät
der Friedrich-Schiller-Universität Jena**

von M. Sc. Theresa Heinrich

geboren am 17.10.1987 in Karl-Marx-Stadt

Gutachter:

1. Herr Prof. Dr. Christian A. Hübner (Jena)
2. Herr Prof. Dr. Reinhard Wetzker (Jena)
3. Herr Prof. Dr. Quan Chen (Beijing)

Tag der öffentlichen Verteidigung: 03.05.2016

Table of contents

Table of contents	I
List of abbreviations	III
1 Summary	1
2 Zusammenfassung	3
3 Introduction	5
3.1 Hereditary sensory and autonomic neuropathies	5
3.2 FAM134B.....	7
3.2.1 Clinical relevance of FAM134B	7
3.2.2 FAM134B protein topology and function.....	8
3.3 Endoplasmic reticulum and Golgi apparatus	9
3.3.1 Architecture of the ER and Golgi apparatus	10
3.3.2 Membrane shaping processes.....	11
3.3.3 ER stress responses	12
3.4 Autophagy	13
3.4.1 Formation of autophagosomes	14
3.4.2 Regulation of autophagic activity	14
3.4.3 Pathways and mechanisms of selective autophagy	15
3.4.4 ER stress-induced autophagy	16
3.4.5 Involvement of autophagy in pathologies	17
3.5 Aims	18
4 Materials and Methods	19
4.1 Materials.....	19
4.1.1 Transgenic knockout mouse model.....	19
4.1.2 Cell lines.....	19
4.1.3 Bacteria.....	19
4.1.4 DNA plasmids	20
4.1.5 Antibodies	20
4.1.6 Kits	21
4.1.7 Chemicals and reagents.....	21
4.2 Methods.....	22
4.2.1 Molecular biology	22
4.2.2 Primary cultures and continuous cell lines.....	23
4.2.3 Protein biochemistry	25
4.2.4 Fam134b topology assay by fluorescence live cell imaging.....	28

4.2.5	Liposome-shaping assay	29
4.2.6	Mouse studies	29
4.2.7	Statistical analysis	31
5	Results	32
5.1	Phenotypic characterization of <i>Fam134b</i> knockout mice	32
5.1.1	Phenotype assessment and knockout verification	32
5.1.2	Analyses of peripheral sensory function <i>in vivo</i>	32
5.1.3	Histological analysis of afferent sensory fibers	34
5.1.4	Ultrastructural analysis of sensory neurons	35
5.1.5	Analysis of motoneuron histology and efferent motor function	38
5.2	Cellular localization and protein-interaction partners of Fam134b	41
5.2.1	Subcellular localization studies	41
5.2.2	Investigation of protein-protein interactions	44
5.2.3	Analysis of the Fam134b membrane topology	47
5.2.4	Membrane shaping function of FAM134B	49
5.3	Functional studies of autophagy in <i>Fam134b</i> knockout tissue and cells	50
6	Discussion	56
6.1	<i>Fam134b</i> knockout mice develop a progressive sensory neuropathy	56
6.2	Changes in the architecture of the ER and Golgi apparatus	58
6.3	Functional domains of Fam134b	60
6.4	Fam134b is involved in selective autophagic pathways	61
6.5	Molecular mechanisms involved in Fam134b-mediated HSAN	63
6.6	Conclusion and further perspectives	65
	References	V
	Appendix Figures	XIII
	Index of Figures	XV
	Index of Tables	XVI
	Curriculum Vitae	XVIII
	Danksagung	XX

List of abbreviations

Atg	autophagy related gene
β -NGF	β -nerve growth factor
BSA	bovine serum albumin
CLSM	confocal laser scanning microscopy
CMAP	compound muscle action potential
CNS	central nervous system
COP	coat protein
DMEM	Dulbecco's modified Eagle's medium
DRG	dorsal root ganglion
EBSS	Earles's buffered salt solution
ECL	enhanced chemiluminescence
ER	endoplasmic reticulum
ERAD	ER-associated protein degradation
ERES	ER exit sites
ERGIC	ER-Golgi intermediate compartment
ERQC	ER quality control compartment
ES cells	embryonic stem cells
FBS	fetal bovin serum
GA	glutaraldehyde
HBSS	Hank's buffered salt solution
HMN	hereditary motor neuropathy
HMSN	hereditary motor and sensory neuropathy
HSAN	hereditary sensory and autonomic neuropathy
HRP	horseradish peroxidase
HSP	hereditary spastic paraplegia
IF	immunofluorescence
IP	immunoprecipitation
KO	knockout
LIR	LC3-interacting region
mc	monoclonal

MEFs	mouse embryonic fibroblasts
MVBs	multivesicular bodies
NCV	nerve conduction velocity
O/N	overnight
PFA	paraformaldehyde
PAS	preautophagosomal structure
PBS	phosphate-buffered saline
pc	polyclonal
PCR	polymerase chain reaction
PLL	poly-L-lysine
PNS	peripheral nervous system
P/S	penicillin/streptomycin
RER	rough endoplasmic reticulum
RT	room temperature
SDS PAGE	sodium dodecyl sulfate polyacrylamide gel electrophoresis
SEM	standard error of the mean
TBS	Tris-buffered saline
TEM	Transmission electron microscopy
TGN	trans-Golgi network
TSNCVs	tail sensory nerve conduction velocities
UPR	unfolded protein response
WB	Western Blotting
w/o	without
WT	wild-type

1 Summary

Degeneration of sensory fibres is characteristic for hereditary sensory and autonomic neuropathies (HSANs). Affected patients share typical symptoms featured by a diminished sensation of temperature, touch and pain. However, the spectrum of disease-associated genes in patients is broad and frequently remains unclear. A previous study had shown that homozygous loss-of-function mutations of FAM134B are causative for severe HSAN classified as type 2B (HSAN2B).

Within this thesis the pathophysiology of HSAN2B was addressed by analyzing transgenic *Fam134b*-knockout mice with biochemical approaches and cell culture assays in combination. The aim was to resolve the Fam134b protein localization, its topology, possible interaction partners and function.

Fam134b-knockout mice manifested a progressive sensory neuropathy. First, a behavioral test for nociception showed a reduced sensitivity towards heat stimuli in aged mice. Secondly, nerve conduction studies addressing the function of large diameter sensory fibres showed smaller and delayed responses, whereas motoneuron action was found to be unaffected. The detailed analysis of sensory ganglion tissue sections of aged animals revealed ultrastructural alterations of the endoplasmic reticulum (ER) and Golgi cisternae by electron microscopy. In agreement with this observation, Fam134b was enriched in subcellular fractions of the ER and Golgi compartment isolated from tissue of wild-type mice.

Another functional study aimed to verify protein interaction partners, which had been identified previously by a yeast two-hybrid screening. Co-immunoprecipitation studies demonstrated binding of FAM134B to autophagy-related ubiquitin-like proteins - also known as LC3-like modifiers or Atg8s. These interactions were mediated by the LC3-interacting region (LIR) that is conserved among members of the FAM134 protein family. Moreover, experiments addressing the topology of FAM134B showed that the C-terminally located LIR of FAM134B faces towards the cytoplasm and thus is accessible to various cytosolic proteins such as LC3.

However, the expression levels of the autophagy marker proteins Beclin-1, p62 and LC3 were unaffected by loss of *Fam134b* in murine cells and tissues. Further, immunohistochemical studies were not indicative of an impaired non-selective autophagic process.

Overexpression studies in cell culture systems revealed FAM134B-mediated delivery of ER fragments into autophagosomal compartments, which was dependent on its functional LIR domain. Further, endogenous *Fam134b* protein expression was decreased under conditions of starvation.

In conclusion, our data suggest that FAM134B serves as an ER-specific autophagy receptor. Hence, FAM134B may regulate ER turnover and maintain long-term homeostasis and survival especially of long-projecting sensory neurons.

Future work may address if *Fam134b* promotes selective degradation of Golgi fragments similar as shown for the ER. Moreover, the identification of additional molecular players as well as specific triggers that contribute to the process named '*ER-phagy*' would be of great interest to study.

2 Zusammenfassung

Hereditäre sensorische und autonome Neuropathien (HSAN) sind seltene, erbliche Erkrankungen, die sich durch Degeneration peripherer, sensorischer Nervenzellen auszeichnen. Betroffene Patienten weisen typischerweise ein erheblich beeinträchtigtes Schmerz- und Temperaturempfinden auf. Bisher konnte nur eine geringe Anzahl HSAN-assoziiierter Gene identifiziert werden, daher bleibt die genetische Ursache oft ungeklärt. Für eine besonders schwere HSAN-Form, die als Typ 2B klassifiziert wird, sind im Jahr 2009 erstmals Mutationen im *FAM134B*-Gen bei Patienten identifiziert worden. Diese Mutationen führen zum Funktionsverlust des kodierten Proteins.

Im Rahmen dieser Promotionsarbeit erfolgte die Untersuchung der HSAN2B zugrunde liegenden Pathophysiologie anhand der Analyse transgener *Fam134b*-Knockout-Mäuse sowie biochemischer und zellbiologischer Studien. Ziel war es, die zelluläre Lokalisation und Topologie, potentielle Interaktionspartner sowie die Funktion von FAM134B zu charakterisieren.

An transgenen *Fam134b*-Knockout-Mäusen gelang der Nachweis einer progressiven, sensorischen Neuropathie. Zum einen wurde dies durch die Untersuchung des nozizeptiven Verhaltens auf einen Hitzestimulus an Mäusen verschiedener Altersgruppen nachgewiesen. Zum anderen zeigte sich eine verzögerte Latenz und Amplitude evozierter sensorischer Potentiale in Knockout-Mäusen im Alter von einem Jahr, wohingegen die motorischen Fasern nicht beeinträchtigt waren. Elektronenmikroskopische Studien an Zellen sensorischer Ganglien ergaben ultrastrukturelle Veränderungen des endoplasmatischen Retikulums (ER) und Golgi Apparates. Das Vorhandensein des *Fam134b* Proteins konnte damit übereinstimmend in Membranen beider Kompartimente, die aus Geweben von Wildtyp-Mäusen isoliert wurden, nachgewiesen werden.

Eine weitere funktionelle Untersuchung hatte das Ziel, potentielle Protein-Interaktionspartner zu verifizieren, die in einem vorausgegangenen Hefe-2-Hybrid-System identifiziert worden waren. Ko-Immünpräzipitationsstudien bestätigten die Interaktion von FAM134B mit Autophagie-assoziierten Proteinen – bekannt als Atg8-Orthologe oder LC3-Proteine. Als molekulare Basis für diese Interaktion konnte eine hoch konservierte LC3-Interaktions-

Region (LIR) in der Aminosäuresequenz von FAM134B identifiziert werden. Darüber hinaus wiesen FAM134B-Topologiestudien nach, dass die C-terminale LIR zytosolisch exponiert vorliegt und somit eine Interaktion mit LC3-Proteinen im zellulären Umfeld ermöglicht.

Die prominenten Komponenten der Autophagie-Maschinerie Beclin-1, p62 und LC3 waren jedoch in ihrem Expressionsniveau in Knockout-Zellen oder Knockout-Geweben unverändert. Ebenso wiesen immunhistochemische Analysen auf keine Beeinträchtigung zellulärer, nicht-selektiver Autophagieprozesse hin.

Gleichzeitig gelang in Überexpressionsstudien der Nachweis einer FAM134B-vermittelten Translokation von ER-Fragmenten in Autophagosomen. Dieser Prozess konnte durch Überexpression einer LIR-defizienten FAM134B-Variante supprimiert werden. Weiterhin war die Expression endogenen Fam134bs unter Nährstoffentzug erheblich verringert.

Ausgehend von diesen Ergebnissen kann die Hypothese aufgestellt werden, dass Fam134b als ER-spezifischer Autophagierezeptor fungiert. Fam134b ist demnach an der ständigen Erneuerung des ERs beteiligt und ist wahrscheinlich entscheidend für die Langzeithomöostase sensorischer Neurone mit besonders langen Zellfortsätzen.

Festzustellen bleibt, dass der Nachweis einer möglichen Regulation des Golgi-Apparates durch die Fam134b-vermittelte, selektive Autophagie weiterer Untersuchung bedarf. Auch die Rolle anderer Proteine, die an diesem spezifischen Abbauprozess beteiligt sind, sowie die Identifizierung spezifischer Auslöser der sogenannten „ER-phagie“ werden Gegenstand weiterer Forschung sein.

3 Introduction

3.1 Hereditary sensory and autonomic neuropathies

The central nervous system (CNS) comprises the brain and spinal cord, while the peripheral nervous system (PNS) is composed of nerves that transmit motor, sensory and autonomic information back and forth between CNS and peripheral organs or tissues. Peripheral autonomic and sensory neuron somata reside in distinct clusters called ganglia. The axon fiber tracts of peripheral neurons are typically long to bridge huge distances within the body.

Peripheral nerve disorders can have tremendous effects and are featured by a wide clinical spectrum. Symmetrical polyneuropathies are relatively common conditions affecting around 2.4% of the human population (Hughes 2008). Peripheral neuropathies may either be acquired (e.g. diabetic neuropathies) or inherited whereby the latter genetic disorders have a relatively low prevalence (Martyn and Hughes 1997). According to the degree of functional impairment in the motor, sensory and autonomic nerve fibers, hereditary peripheral neuropathies are categorized as hereditary motor neuropathies (HMNs), hereditary motor and sensory neuropathies (HMSN) and hereditary sensory and autonomic neuropathies (HSANs) as reviewed in Rotthier et al. (2012).

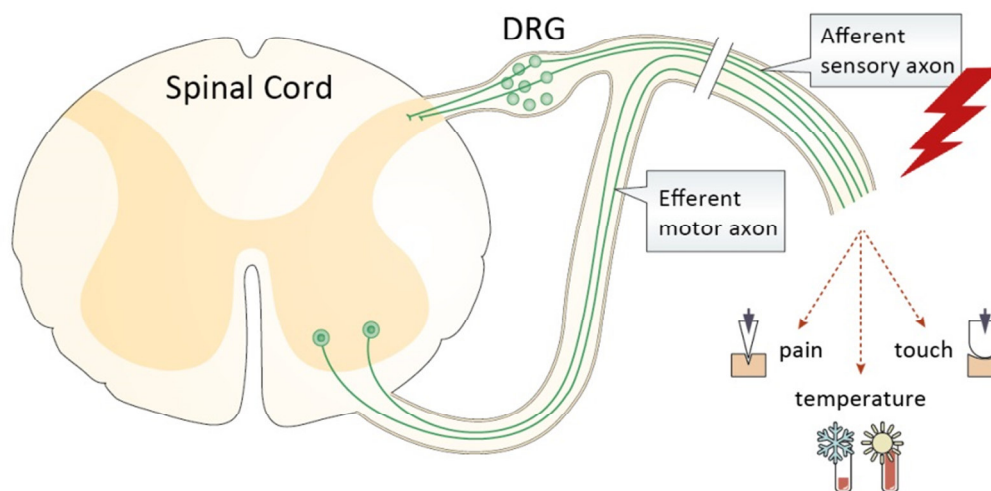


Figure 1: Afferent sensory fiber dysfunction in hereditary sensory and autonomic neuropathies

The peripheral nervous system (PNS) is composed of efferent and afferent axons that are characterized by exceedingly long fiber tracts. Efferent motor neuron somata reside in the ventral horn of the spinal cord, whereas afferent sensory neuron somata are clustered in ganglia. Here, a dorsal root ganglion (DRG) is illustrated. Hereditary sensory and autonomic neuropathies (HSANs) are characterized by the predominant impairment of afferent sensory neurons leading to progressive loss of sensation to pain, temperature and touch. Figure was modified from Conforti et al. (2014).

HMNs, HMSNs and HSANs can be further summarized as ‘length-dependent axonopathies’ since neurons of particular long axon fiber tracts of the peripheral nervous system are affected. In Figure 1 the exceedingly long projections of afferent and efferent neurons are illustrated. The marked predominant degeneration of afferent sensory neurons with their cell bodies located in dorsal root ganglia (DRGs) is typical for HSANs.

HSANs comprise five clinically heterogeneous subtypes and are characterized by the mode of inheritance, genetic background, age at onset and varying degrees of sensory and autonomic involvement. This historical classification that is based on Dyck (Dyck et al. 1993) is still valid but has been modified and additional subtypes have been suggested (Auer-Grumbach 2013).

The most common symptoms of HSANs include the progressive loss of sensation of pain and temperature frequently accompanied by painless injuries as well as chronic ulcerations at hands and feet which can lead to severe complications up to amputations. However, the detailed clinical presentation is highly variable ranging from mild sensory disturbances to a complete loss of sensation and variable motoric or autonomic dysfunction both within and beyond the different HSAN subtypes. This heterogeneity in symptoms and severity further complicates differential diagnosis from HSAN-related diseases such as ‘congenital inability to experience pain’ (Auer-Grumbach 2013).

Novel genetic approaches such as next-generation-sequencing helped to identify a number of HSAN-disease causative genes. However, in more than two-thirds of human patients the genetic cause remains unresolved (Rotthier et al. 2012).

Known causative mutations of the autosomal dominant HSAN subtype I affect genes associated with various cellular processes such as vesicular axonal transport, tubulation of the endoplasmic reticulum (ER) or DNA methylation. In the group of recessive HSANs that are subclassified in type II, III, IV and V causative genes are found to be involved in correct axon guidance during development, nociceptive pathway regulation, cytoskeletal organization or axonal transport. Some HSAN-associated genes are identified but still remain to be functionally characterized (Rotthier et al. 2012). Further, the identification of additional disease causing genes in each of the HSAN subtypes will shed more light into fundamental disease mechanisms and provide a better understanding of cellular pathways affected in HSANs.

3.2 FAM134B

3.2.1 Clinical relevance of FAM134B

In 2009, a new subgroup of HSAN2 was defined by the identification of the disease-associated gene *FAM134B*, the '*family with sequence similarity 134, member B*', which is further known as *JK-1* (Kurth et al. 2009). The identified homozygous loss-of-function mutation (S309X) was associated with a severe clinical presentation and involved early-onset impaired nociception. Mutilating ulcerations of hands and feet and chronic osteomyelitis (see Figure 2) were diagnosed in three affected siblings of unaffected consanguineous parents, who were heterozygous carriers of the S309X mutation (Kurth et al. 2009).



Figure 2: Clinical features of *FAM134B*-mediated HSAN2B

The severity of *FAM134B*-associated peripheral sensory neuropathy is shown by the example of a human patient that clinically presented with progressive mutilating ulcerations of hands and feet accompanied by osteolysis involving the distal phalanges of the fingers and toes. The figure was published in Kurth et al. (2009).

Additional mutations in the *FAM134B* gene have been identified, such as the Q145X mutation, resulting in severe protein truncation (Kurth et al. 2009, Murphy et al. 2012). Generally, the disease characteristics appear during the first decade of life and acroosteomyelitis necessitating amputations, is a common complication in the disease course. A weak motor involvement is described for a few of the reported cases or may even lead to a spastic gait (Davidson et al. 2012, Aydinlar et al. 2014). In addition, autonomic dysfunction may present as impaired pupillary light reflex, feeding problems, incontinence, apnea or hyperhidrosis (Kurth et al. 2009, Hübner and Kurth 2014).

Apart from those few familial cases with hereditary *FAM134B*-mediated HSAN2B, oncogenic properties are associated with somatic mutations of *FAM134B* that is commonly termed as *JK-1* in this context. *JK-1* was reported to be upregulated in human cases of esophageal squamous cell carcinoma (Tang et al. 2007) and colorectal tumours (Kasem et al. 2014), so a role in developing invasive phenotypes crucial for disease progression is considered.

Moreover, *FAM134B* was identified as a candidate gene for the susceptibility of vascular dementia (Kong et al. 2011).

3.2.2 *FAM134B* protein topology and function

FAM134B is predicted as membrane integral protein with structural similarities to reticulon proteins (Hübner and Kurth 2014). The characteristic feature that unites all of the reticulon-like proteins is the special length of the hydrophobic domains, which is about 28-36 amino acids, each (Yan et al. 2006). This distance is too long to span the lipid bilayer once and not sufficient to fully span it twice. It is assumed that reticulon-like proteins integrate in a horse shoe-like orientation into intracellular membranes, thus, occupying more area in the outer leaflet and thereby bend the membrane (Voeltz et al. 2006). The putative membrane-bound topology of *FAM134B* is illustrated in Figure 3. Further, *FAM134B* is characterized by a C-terminal coiled-coil-domain.

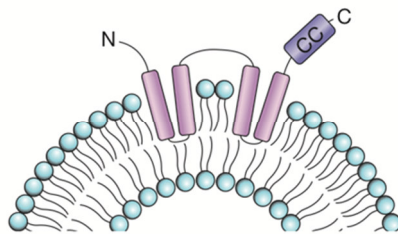


Figure 3: Predicted *FAM134B* protein topology

The *FAM134B* protein contains two hydrophobic segments predictive for membrane localization. The hydrophobic regions are interrupted by a short hydrophilic region most probably forming a hairpin-like topology. Moreover, *FAM134B* is characterized by a C-terminal coiled-coil domain. The figure was published by Hübner and Kurth (2014).

Initial studies to elucidate *Fam134b* protein function revealed structural alterations of the Golgi-compartment in murine neuroblastoma Neuro-2a cells, upon knockdown of *Fam134b*. Further it was demonstrated that primary sensory cultures showed selective neuronal death of small and medium sized cells if *Fam134b* was silenced (Kurth et al. 2009). However, downstream events leading to the progressive sensory neuropathy observed in humans remained speculative.

3.3 Endoplasmic reticulum and Golgi apparatus

The endoplasmic reticulum (ER) and Golgi apparatus are an important part of the endomembrane system in eukaryotic cells and are functionally involved in the early secretory and endocytic pathway. A complex equilibrium exists between both compartments that are connected via intense bidirectional trafficking for the purpose of coordinating various cellular functions (Hsu et al. 2009). First of all, these functions include the synthesis, modification, quality control and sorting of proteins and lipids. In the end, cargo molecules are packed into transport vesicles and sent to their specific destination by budding from the ER and Golgi apparatus (Griffiths and Simons 1986, Baumann and Walz 2001, Appenzeller-Herzog and Hauri 2006).

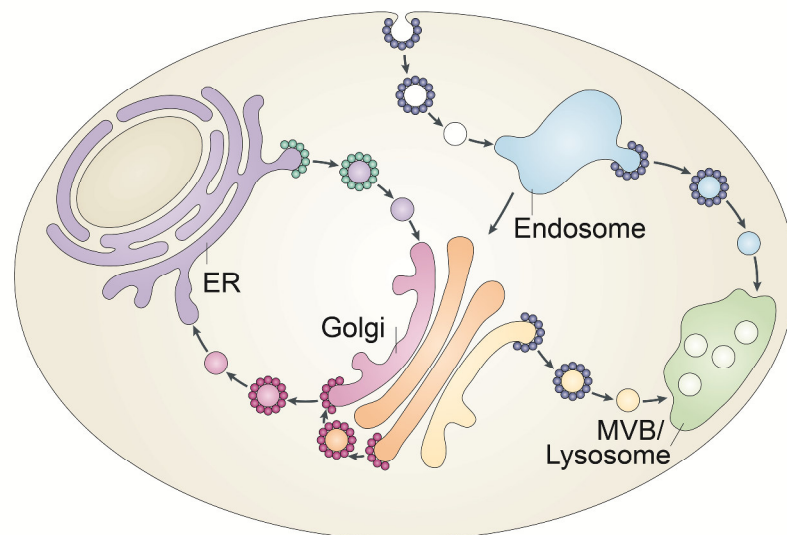


Figure 4: Vesicular trafficking between the endomembrane compartments

The endomembrane system of eukaryotic cells consists of the endoplasmic reticulum (ER), the Golgi apparatus (Golgi), the endosomal and lysosomal compartment. The flow of material inbetween these dynamically changing organelles is mediated by certain vesicle coat proteins. Coat protein II (COPII) illustrated as green sphere forms vesicles of the ER to Golgi transport (termed as anterograde); whereby COPI (red sphere) forms vesicles for both retrograde transport from Golgi apparatus to the ER and for intra-Golgi transport. Endocytosed vesicles which bud off from the plasma membrane are Clathrin (blue sphere) coated. Moreover, Clathrin forms vesicles that traffick from the trans-Golgi network (TGN) to multivesicular bodies (MVBs) and lysosomes. The figure was modified from Hsu et. al. (2009).

A second set of functions comprises clathrin-mediated endocytosis that may target endo- or lysosomal compartments, but also the Golgi apparatus if recycling and sorting of endocytosed material is required (Maxfield and McGraw 2004). Overall, the complex membrane trafficking machinery depicted in Figure 4 is fundamental to maintain cellular homeostasis and requires dynamic organellar changes, particularly of the ER and Golgi compartment, and continuous membrane remodeling processes.

3.3.1 Architecture of the ER and Golgi apparatus

ER and Golgi compartments constitute multifunctional membrane organelles of extraordinary structural diversity and plasticity during cell growth, division and even under basal conditions (Puhka et al. 2012, Shibata et al. 2009, Lippincott-Schwartz et al. 2000). ER structural subcompartments comprise the nuclear envelope, peripheral sheet-like structures associated with ribosomes and a network of interconnected smooth tubules devoid of ribosomes. Recent evidence suggests that the tubules and sheet abundance are in accordance to the expression level of specific sheet- or tubule-forming proteins that possess differential membrane shaping capacities (Shibata et al. 2009, Lynes and Simmen 2011). Functionally, the rough ER is the major site of co-translational membrane insertion of proteins, whereas the smooth ER mediates calcium homeostasis and lipid biosynthesis (Lippincott-Schwartz et al. 2000). Additionally, in the last decades distinct subdomains such as ER exit sites (ERES), plasma membrane-associated ER, the mitochondria-associated membrane and the ER quality control compartment (ERQC) have been associated with specific functions (Lynes and Simmen 2011).

While the ER is an interconnected network of sheet and tubules, the Golgi apparatus consists of cisternae, which are stacks of perforated flattened sheets, hallmarked by a strong structural and functional polarity (Farquhar and Palade 1981). The disc-shaped cisternae form three functionally distinct subcompartments: cis-, medial- and trans-Golgi apparatus. Translated proteins are modified in the ER and delivered to the Golgi apparatus via anterograde transport in COPII-positive vesicles. The vesicles received from the ER enter the Golgi apparatus at the cis-face and the cargo moves through the stack into trans-direction where it undergoes posttranslational modifications. Cargo-packed vesicles with another distinct coat composition are formed at the trans-Golgi apparatus where products are sorted and sent to their destination within the cells (Day et al. 2013).

The ER-Golgi interface termed as '**ER-Golgi intermediate compartment**' (ERGIC) is precisely defined by the presence of the 53-kDa-membrane-protein (ERGIC-53) (Hauri et al. 2000). The ERGIC compartment is described as a complex stationary sorting membrane system of vesicular-tubular clusters for anterograde and retrograde trafficking between the ER and Golgi apparatus (Appenzeller-Herzog and Hauri 2006). In different phases of the cell cycle ER and Golgi structures undergo dynamic changes: The peripheral ER is largely tubulated (Puhka et al. 2007) and the nuclear membrane as well as the Golgi apparatus almost completely disassembled during mitosis but reestablish afterwards (Robbins and Gonatas 1964).

3.3.2 Membrane shaping processes

The ER and Golgi membrane system is highly dynamic and its functional domains are in constant flux. The complex morphological changes of both endomembrane compartments are attributable to various microtubule-associated interconnecting proteins, membrane fusion and fission events as well as membrane shaping proteins (Pendin et al. 2011).

The predominant ER membrane arrangement as low curvature sheets or high curvature tubules is an energetically unfavorable state of the phospholipid bilayer and requires active membrane shaping. Several studies highlighted the outstanding role of the reticulon and DP1/REEP/Yop1 proteins for triggering ER tubule formation (Voeltz et al. 2006). They are featured by a special hairpin topology based on two transmembrane hydrophobic segments. Their length of 28-36 residues is a fundamental property (Yan et al. 2006) and enables insertion in the outer leaflet of the membrane bilayer, thereby forming a 'wedge' that increases the surface area of the outer leaflet relative to the inner leaflet. In addition, these proteins were shown to function as oligomers and contribute to scaffolding (Shibata et al. 2008).

Some uncertainty still exists about the principle of ER sheet morphology. It is suggested that membrane-bound Climp63 that is restricted to the reticular part of rough ER, mediates ER sheet formation. By its extensive ER luminal segment that potentially folds as coiled-coil, it might form multimeric protein oligomers and function as ER luminal spacer (Klopfenstein et al. 2001). Alternatively, reticulon-domain containing proteins that promote ER tubule formation similarly might be involved in promoting high membrane curvature at the sheet edges. Consistently these proteins localize to both tubules and sheet edges, though, if overexpressed sheets are converted into tubules (Shibata et al. 2010).

Moreover, in higher eukaryotes, the shape of organelles is facilitated by membrane tethering mechanisms. The attachment of membranes either to components of the cytoskeleton, as described for Climp63, or tethering of two membranes to each other leading to regular intercisternal spacing in Golgi stacks for instance, represent mechanisms for shaping subcompartments (Voeltz and Prinz 2007).

In addition, coordinated membrane remodeling requires fusion and fission of vesicles e.g. at ER exit sites (ERES) and at lateral edges of Golgi cisterna that subsequently fuse to the next cisterna. Here, SNARE (soluble N-ethylmaleimide-sensitive factor attachment protein receptor) proteins were identified to drive membrane fusion to merge two membranes into one (Jahn and Scheller 2006). Further, atlastin proteins belonging to the dynamin superfamily of

GTPases, are found to be involved in membrane remodeling events by its oligomerization-stimulated GTPase activity (Orso et al. 2009, Hu et al. 2009). Strikingly, dynamin proteins mediate membrane fission events for vesicle budding (Praefcke and McMahon 2004).

3.3.3 ER stress responses

ER homeostasis is of crucial importance as most of the secreted or integral membrane proteins are assembled, modified and sorted at this compartment. Proper protein folding is strictly controlled at various levels and accumulation of unfolded proteins is immediately counteracted by the unfolded protein response (UPR), a highly conserved ER-to-nucleus signaling pathway (Ron 2002). UPR target genes are upregulated and include chaperones, transport proteins, mediators of ER-associated protein degradation (ERAD) and phospholipids in order to fold, process, and secrete proteins faster. At least three mechanistically distinct pathways are described to cooperate in sensing unfolded proteins in the ER, each activating distinct transcription factors (Bernales et al. 2006a).

In detail, unfolded proteins competitively bind the chaperone-glucose regulated protein of 78 kDa (Grp78 or BiP) in the ER lumen. If unfolded proteins accumulate Grp78 is released from its inhibitory interactions with IRE1 α (inositol-requiring protein 1 α), PERK (protein kinase RNA-like ER kinase) and ATF6 (activating transcription factor 6) (Wang et al. 2009). Each of these three branches triggers UPR target gene expression. Thus, the UPR constitutes a set of powerful stress response pathways that lead to the activation of both pro-survival and pro-apoptotic mechanisms. If stress is more severe than UPR can compensate for, apoptosis is triggered. However, chronic but mild ER stress keeps pro-survival stimuli active and diminishes pro-apoptotic stimuli, a phenomenon which is termed 'ER hormesis' (Rutkowski et al. 2006).

A frequent cellular response as part of the UPR is the proliferation of the ER (Maiuolo et al. 2011). The increased ER compartment dilutes the concentration of unfolded proteins and thereby prevents their aggregation. In contrast, little attention has been paid to pathways of potential Golgi apparatus-specific stress responses comparable to the ER-related UPR.

The remarkable importance of the ER and Golgi apparatus morphology is provided by the existence of many human disorders associated with alterations of Golgi or ER structure and such disease were found frequently implicated in neurological dysfunction (Renvoise and Blackstone 2010).

3.4 Autophagy

Autophagy ('self-eating') is a catabolic process involving degradation of cytosolic components or cytoplasmic organelles within lysosomes in eukaryotic cells. Autophagic pathways are tightly regulated and play a pivotal role in balancing synthesis, degradation and turnover of cellular components, thus, contributing to metabolic and nutrient homeostasis (Kaur and Debnath 2015). Two major degradative systems exist: while the ubiquitin-proteasome-system is restricted primarily to short-lived and soluble proteins, autophagy has the capacity to degrade a wider spectrum of substrates such as long-lived bulky proteins, intracellular organelles or extracellular material delivered by the endocytic pathway (Korolchuk et al. 2010). Autophagic pathways are categorized into three types: microautophagy, chaperone-mediated autophagy and macroautophagy (Mizushima and Komatsu 2011). In microautophagy small components of the cytoplasm are directly engulfed by membrane invagination of the lysosomal or late endosomal compartment (Sahu et al. 2011). Chaperone-mediated autophagy does not involve membrane reorganization but chaperone-mediated translocation of substrate proteins into the lysosomal lumen across the lysosomal membrane (Cuervo and Wong 2014). In the process called macroautophagy a *de novo* synthesized compartment named 'autophagosome' is formed. Autophagosomes are double-membrane vesicular structures derived from an initial phagophore (also termed as pre-autophagosomal structure (PAS) or isolation membrane) which engulfs cytoplasmic cargo. The fusion of autophagosomes with lysosomes generates the so-called 'autolysosome' where the inner autophagosomal membrane and the trapped material is degraded by lysosomal proteases as shown in Figure 5 (Stolz et al. 2014). This thesis focuses on the latter macroautophagic pathway which is hereafter termed 'autophagy' for simplicity.

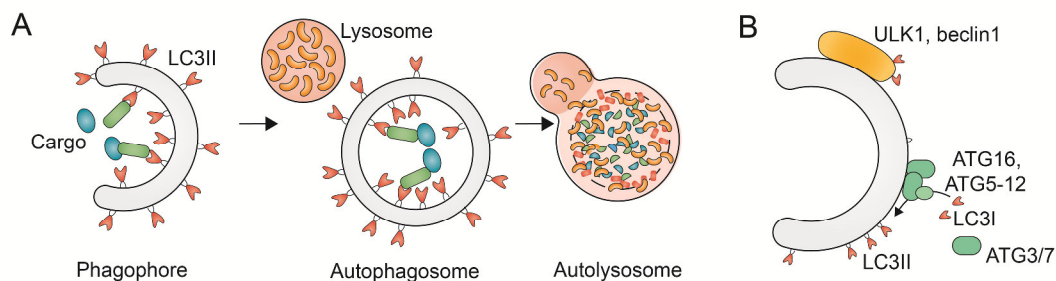


Figure 5: Autophagosome formation and initiation in macroautophagic pathways

(A) The phagophore (also called isolation membrane) is decorated with LC3-II and engulfs specific cargo. In the next step, the double membrane autophagosome fuses with a lysosome generating an autophagolysosome where proteases degrade the inner autophagosomal membrane and the trapped cytosolic material. (B) Phagophore nucleation is initiated by complexes involving autophagy adaptors such as ULK1 and beclin1. For elongation of the phagophore membrane certain Atg proteins are required. The figure was modified from Stolz et al. (2014).

3.4.1 Formation of autophagosomes

The core molecular machinery of autophagosome formation was intensively studied in yeast which allowed the identification of more than 30 essential *autophagy-related* (*ATG*) genes. Klionsky et al. (2003) summarized the nomenclature of *ATGs* which are conserved from yeast to mammals throughout evolution (Weidberg et al. 2011). The key proteins required for autophagosome formation are illustrated in Figure 5B. In detail, phagophore initiation involves both the Atg1/Unc-51-like kinase (ULK) complex that is considered as the central autophagy regulator. The Atg6/Beclin1 core complex promotes production of phosphatidylinositol-3-phosphate, which is recognized by early autophagic effector proteins triggering the autophagy cascade. The sources of membranes implicated in the isolation membrane formation are various and include the endoplasmic reticulum (Hayashi-Nishino et al. 2009), mitochondria (Hailey et al. 2010), the plasma membrane (Ravikumar et al. 2010) and the Golgi apparatus (Yen et al. 2010, van der Vaart et al. 2010, Ohashi and Munro 2010). Once nucleated, the phagophore requires the ubiquitin-like proteins Atg8 and Atg12 in their activated (mediated by Atg7) and processed (conjugated by Atg3 and Atg10, respectively) forms. Following the conjugation of Atg12 with Atg5 the association of Atg16 occurs and acts at the phagophore membrane site for the recruitment and conjugation of Atg8. A mammalian homologue to Atg8 is LC3 (microtubule-associated protein 1-light chain 3), for this reason mammalian Atg8s are often referred to as 'LC3-like modifiers'. The cytosolic form termed as LC3-I conjugates with phosphatidylethanolamine generating pre-autophagosomal membrane-associated LC3-II mediating membrane elongation and autophagosome maturation (Ichimura et al. 2000, Nakatogawa et al. 2009).

3.4.2 Regulation of autophagic activity

Following autophagosome formation, Atg proteins are removed from the autophagosomal membranes with the exception of Atg8/LC3II. These proteins remain attached to the autophagosomal membrane, which allows the assessment of autophagosome abundance in cells or tissue by analyzing the LC3-II protein expression level.

Studies over the past decades have elucidated that autophagy is strongly induced by nutrient starvation. The underlying molecular mechanisms involve mTOR-mediated Ulk-phosphorylation. Under nutrient-rich conditions mTOR inhibits Ulk-activity and thereby prevents excessive autophagosome formation. In contrast, nutrient deprivation is known to

inhibit mTOR activity that abolishes the inhibition of Ulk and stimulates autophagic degradation (Hosokawa et al. 2009).

The starvation-induced upregulation of autophagic activity is a fundamental and highly conserved process that enables the survival of cells by counteracting nutrient deprivation attributable to the mobilization of cellular nutrient and energy stores (Kaur and Debnath 2015). However, a low and basal level of autophagy is evident even under nutrient-rich conditions and may regulate continuous protein turnover or eliminate proteins and organelles with aberrant structure to keep the cellular homeostasis (Mizushima and Komatsu 2011). Consequently, the importance of autophagy as starvation-induced non-selective bulk degradative pathway was extended by its additional function for the selective elimination of distinct cargo as crucial quality control pathway (Yang and Klionsky 2010).

3.4.3 Pathways and mechanisms of selective autophagy

Various pathways of selective autophagy have been discovered and were reviewed by Johansen and Lamark (2011). Generally, cargo destined for degradation is specifically bound by an ‘autophagy receptor’ protein interacting with LC3-like modifiers present at the phagophore membrane (see Figure 6). Then, the selected cargo is targeted into autophagosomal compartments and gets degraded.

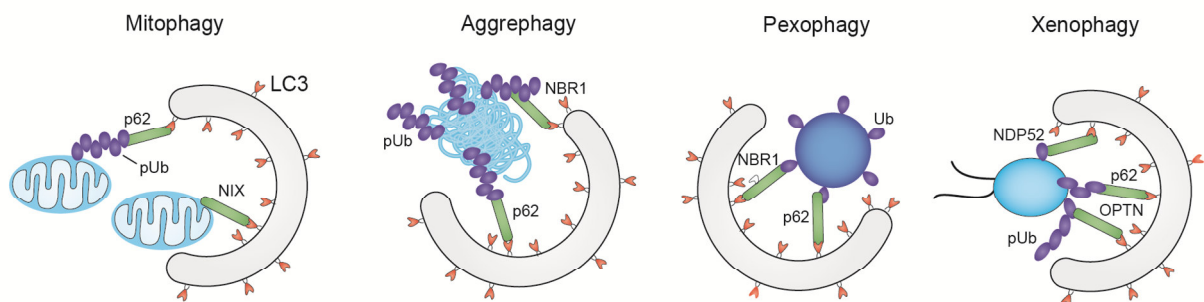


Figure 6: Selective types of autophagy involve autophagy receptor protein function

Examples for selective types of autophagy: Mitophagy requires distinct autophagy receptor protein function such as p62-binding to poly-ubiquitylated (pUb) mitochondria or direct NIX-binding. Aggrephagy may be mediated by p62 or NBR1 binding to pUb protein aggregates leading to their selective sequestration. The removal of mono-ubiquitylated peroxisomes can be similarly mediated by p62 or NBR1 recruitment. At last, for xenophagy NDP52, p62 or OPTN targets ubiquitylated bacteria to the LC3II-decorated phagophore. The figure was modified from Stolz et al. (2014).

The first autophagy receptor protein discovered was the multifunctional scaffold protein p62 (also named sequestosome 1) (Bjørkøy et al. 2005) that is implicated in many processes, including cell signaling, receptor internalization and protein turnover (Moscat et al. 2007).

The C-terminal located ubiquitin-binding domain UBA of p62 recognizes various ubiquitinated substrates including mitochondria, protein aggregates, peroxisomes and intracellular pathogens. Likewise, ubiquitination as degradation signal for selective autophagy is utilized by NBR1 (neighbour of BRCA1 gene 1), NDP52 (nuclear dot protein 52 kDa) and OPTN (optineurin) which all belong to the group of sequestosome-1-like autophagy receptors (Birgisdottir et al. 2013, Stolz et al. 2014). An ubiquitin-independent selective autophagy process is mediated by NIX (also known as BNIP3L) promoting mitochondrial clearance after mitochondrial damage and during erythrocyte differentiation (Novak et al. 2010). Further, FUNDC1 was recently identified as mitochondria-selective autophagy receptor (Liu et al. 2012).

Within the past years the list of identified autophagy receptors was largely expanded and the most common feature is the LC3-interacting region (LIR) motif (Birgisdottir et al. 2013). This characteristic amino acid sequence constitutes the molecular basis for their specific interaction with LC3-like modifiers. The core consensus sequence is featured by the formula: [W/F/Y]xx[L/I/V] with 'x' for any amino acid. The motif commonly starts with any of the aromatic amino acids Tryptophan (W), Phenylalanine (F) or Tyrosine (Y) whose side chain deeply binds into a hydrophobic pocket of Atg8 proteins. One of the hydrophobic amino acids Leucine (L), Isoleucine (I) or Valine (V) constitutes another key feature of the LIR motif by interacting with a second hydrophobic pocket of Atg8 proteins. In addition to these highly conserved core amino acids acidic or phosphorylated groups upstream of the LIR have been shown to strengthen the interaction (Rogov et al. 2014). Furthermore, non-canonical LIR motifs exist such as described for the autophagy receptor NDP52 which lacks aromatic amino acids but possesses crucial function for innate immunity in the context of xenophagy (von Muhlinen et al. 2012).

3.4.4 ER stress-induced autophagy

Autophagy is a stress-responsive pathway allowing cells to adapt their metabolism to stressful conditions counteracting general nutrient depletion or exposure to more specific stressors which in turn triggers highly selective responses. In this regard, cells exposed to ER stress excessively generate autophagosomes (Cebollero et al. 2012). Additionally, autophagosome-independent ways equivalent to microautophagy are described to remove damaged ER from cells (Schuck et al. 2014). These different responses seem to constitute an additional cellular mechanism to cope with ER stress in addition to the UPR and ERAD that have been

introduced in chapter 3.3.3. The UPR entails significant expansion of the ER volume and, notably, formed autophagosomes contain densely packed ER fragments suggesting an ER-specific autophagic process (Bernales et al. 2006b). Moreover, the generation of ER-containing autophagosomes is protective against cell death (Ogata et al. 2006, Bernales et al. 2006b) and thus requires an efficient interplay of autophagic pathways with apoptotic signaling for efficient stress responses as reviewed by Kroemer et al. (2010).

Overall, there is growing evidence highlighting the vital importance of selective autophagic degradation as part of the complex ER-stress response mechanisms. However, a systematic understanding of the key players that contribute to stress-induced ER-phagy and how they are regulated in the complex network of cooperating cellular pathways is still lacking.

3.4.5 Involvement of autophagy in pathologies

Recent developments in the field of autophagy have led to an increased interest in its implication in human pathologies. A critical role of autophagy is recognized in a broad spectrum of immune-related, neoplastic, cardiovascular and neurodegenerative diseases (Kroemer 2015).

Knockout studies of autophagy genes in rodents aimed to understand their pathogenetic functions, but clearly indicated the indispensability of autophagic pathways for postnatal survival. For instance mice with a constitutive knockout of *Atg5* (Kuma et al. 2004), *Atg7* (Komatsu et al. 2005) or *Atg3* (encodes a crucial enzyme for Atg8-lipidation process) (Sou et al. 2008) die immediately after birth at the neonatal stage. However, conditional knockout models of *Atg5* and *Atg7* in neurons mediated by nestin-cre recombinase importantly linked impaired autophagy with the accumulation of protein aggregates in neurons – a hallmark of neurodegenerative diseases (Komatsu et al. 2006, Taichi et al. 2006). Human neurodegenerative disorders such as Alzheimer's disease, Parkinson's disease, Huntington's disease and amyotrophic lateral sclerosis (ALS) are featured by aggregated ubiquitinated and p62-positive structures within neurons (Yamamoto and Simonsen 2011, Weidberg et al. 2011, Tan et al. 2014). Moreover, in familial cases of ALS loss-of-function mutations in the autophagy receptor proteins p62 and optineurin have been identified (Hirano et al. 2013, Teyssou et al. 2013, Maruyama and Kawakami 2013). This genetic link demonstrates the association of selective autophagy-deficiency and neurodegenerative human disease mechanisms. The respective signaling pathways remain to be discovered and may allow the development of autophagy modulators for future therapeutic intervention (Frake et al. 2015).

3.5 Aims

Because mutations in *FAM134B* can cause HSAN2, its respective gene product FAM134B should be characterized with the help of a combination of biochemical, cellular and *in vivo* approaches. In particular:

- The specificity of available antibodies directed against FAM134B should be characterized.
- The subcellular localization of the protein had to be resolved.
- The topology of the protein should be addressed to get a better idea about its possible function.
- The relevance of putative interaction partners, which had been identified previously by a yeast two-hybrid screening, should be assessed.
- Based on the preliminary results suitable cellular assays had to be selected to further address the cellular function of FAM134B.
- Finally, a knockout mouse model already available in the lab should be characterized to study the relevance of the *in vitro* findings for the disease phenotype.

4 Materials and Methods

4.1 Materials

4.1.1 Transgenic knockout mouse model

Transgenic *Fam134b* knockout mice were used for the performed animal studies. The *Fam134b* knockout mouse model was generated by the deletion of exons six to eight (Figure 7), encoding large parts of the C-terminal reticulon domain of Fam134b. 129SvJ-derived embryonic stem (ES) cells were injected into C57BL/6 blastocysts and chimeric mice were backcrossed with C57BL/6 mice. Animal studies were performed in a mixed background after four to five generations.

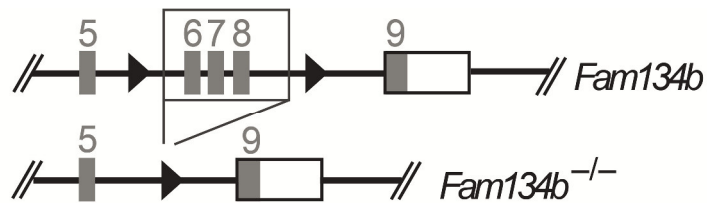


Figure 7: Knockout strategy for *Fam134b* transgenic mouse generation

The genomic structure of the targeted *Fam134b* locus (top) and *Fam134b* knockout allele (bottom) is shown. The correctly targeted *Fam134b* allele comprised two loxP sites (illustrated as black triangles) flanking exons 6 to 8. Targeted ES cells were selected for the generation of chimeric mice. Breeding of chimaeras with Cre-deleter mice resulted in Cre-lox mediated deletion of exons 6 to 8.

4.1.2 Cell lines

Table 1: Cultivated eukaryotic cell lines

Cell line	Description
HEK293T	human embryonic kidney 293 cells expressing SV40 large T-antigen
COS-7	african green monkey kidney cells
MEFs ^{+/+} ; MEFs ^{-/-}	mouse embryonic fibroblasts, isolated from <i>Fam134b</i> wild-type (+/+) and knockout (-/-) mice; immortalized by the SV40 large T-antigen

4.1.3 Bacteria

For amplification of DNA plasmids the bacterial strain *Escherichia coli* XL-1-Blue was used.

4.1.4 DNA plasmids**Table 2: List of DNA plasmids**

<i>Protein expressed by vector DNA</i>	<i>Vector construct</i>	<i>Source</i>
GFP-FAM134B	peGFP_C2	Lab-intern
FAM134B-GFP	peGFP_N2	Lab-intern
FAM134B-myc	pcineo_CT_myc	Lab-intern
FAM134B-S309X-myc	pcineo_CT_myc	Lab-intern
CD3-RFP	pRFP_N1	Lab-intern
RFP-KDEL	pcDNA3.1_Hygro	C.Kaether lab, FLI Jena
HA-FAM134B	pcDNA3.1	I.Dikic lab; Goethe University Frankfurt
HA-FAM134BmutLIR	pcDNA3.1	I.Dikic lab; Goethe University Frankfurt

4.1.5 Antibodies**Table 3: List of commercial primary antibodies**

<i>Antibody</i>	<i>Host, clonality: polyclonal (pc); monoclonal (mc)</i>	<i>Company</i>	<i>ID number</i>	<i>Working dilution for Western Blot (WB); Immunofluorescence (IF)</i>
anti- β -Actin	mouse (mc)	Abcam	ab6276	1:5000 (WB)
anti-Climp63	rabbit (pc)	Proteintech	16686-1AP	1:2000 (WB), 1:500 (IF)
anti- γ -Adaptin	mouse (mc)	BD	610386	1:2000 (WB)
anti-GFP	rabbit (pc)	Abcam	ab6556	1:1000 (IF)
anti-Giantin	mouse (mc)	Enzo	ALX-804-600-C100	1:2000 (IF)
anti-GM130	mouse (mc)	BD	610823	1:500 (WB), 1:250 (IF)
anti-Grp78	mouse (mc)	BD	610979	1:2000 (WB)
anti-HA	rat (mc)	Roche	11867423001	1:1000 (IF)
anti-LC3B	rabbit (pc)	Novus B.	NB100-2220	1:500 (WB)
anti-LC3	rabbit (mc)	Cell Sign.	3868	1:2000 (WB)
anti-myc Tag	rabbit (pc)	Millipore	06-549	1:1000 (WB)
anti-PDI	mouse (mc)	Enzo	ADI-SPA-891	1:2000 (WB)
anti-p62	mouse (pc)	Enzo	BML-PW9860	1:1000 (WB), 1:500 (IF)
anti-Rtn4	rabbit (pc)	Abcam	ab47085	1:2000 (WB), 1:500 (IF)

The FAM134B-specific antibody was custom-made (Pineda). Rabbits were immunized against the peptide (C)GYTPQTDTSDDLDRP (amino acids 307–321 of FAM134B). Resulting antisera were purified on an affinity matrix conjugated with the peptide.

Secondary horseradish peroxidase (HRP)-labeled antibodies anti-rabbit (NA9340) and anti-mouse (NA9310) were obtained from ‘GE Healthcare Life Sciences’ and diluted 1:4000.

Alexa Fluor® conjugated goat secondary antibodies (A10525; A11035; A11008; A11030; A11029) were purchased from ‘Life Technologies’ and applied as 1:2000 dilutions.

4.1.6 Kits

Clarity™ Western ECL Substrate (Bio-RAD; Cat. No. 170-5061)

NucleoBond® Xtra Midi (Macherey-Nagel; Cat. No. 740410)

Pierce™ BCA Protein Assay Kit (Thermo Scientific; Cat. No. 23228)

4.1.7 Chemicals and reagents

Acrylamide/bisacrylamide mixture, Rotiphorese® Gel 40 (Roth; Cat. No. A515.1)

Anti-c-Myc Agarose (Thermo Scientific; Cat. No. 20168)

β-nerve growth factor (β-NGF) (Preprotec; Cat. No. 450-01)

Bovine serum albumin (BSA), pH 7.0 (PAA; Cat. No. K41-001)

B-27® Supplement (50X) (Gibco Cat. No. 17504-44)

Chloroquine (Sigma; Cat. No. C6628)

Collagenase II (Worthington; Cat. No. 4176)

Dimethyl sulfoxide (DMSO) (Sigma Aldrich; Cat. No. D2650)

DMEM + GlutaMAX-I (Gibco; Cat. No. 31966-021)

Dnase I (Applichem; Cat. No. A3778)

Fetale bovine serum (FBS) (biowest; Cat. No. S1810-500)

Fluoromount-G (Southern Biotech; Cat. No. 0100-01)

GFP-Trap®_A (Chromotek, Cat. No. gta-20)

Glutaraldehyde (GA) (25% solution in water; Serva; 23114.01)

Hank’s buffered salt solution (HBSS) (Gibco; Cat. No. 14175-053)

Hoechst 33258 (Invitrogen; Cat. No. H3569)

Horse serum (Sigma; Cat. No. H-0146)

L-Glutamine (Gibco; Cat. No. 25030)

Lipofectamine®2000 (Invitrogen; Cat. No. 11668-019)

Minimum Essential Medium (MEM) (Gibco; Cat. No. 31095-029)
Neurobasal-A Medium (Gibco; Cat. No. 10888-022)
OptiMEM (Gibco; Cat. No. 51985-034)
OptiPrep™ Density Gradient Medium/ Iodixanol solution (Sigma; Cat. No. D1556)
PageRuler Plus Prestained Protein Ladder (Thermo Scientific; Cat. No. 26620)
PCR-buffer (10x) (Invitrogen, Cat. No. Y02028)
Penicillin-Streptomycin (P/S), (5,000 U/mL; Gibco; Cat. No. 15070-063)
Poly-L-lysine hydrobromide (PLL), (Sigma; Cat. No. P2636)
Protease Inhibitor Cocktail Tablets, (Roche; Cat. No. 04693116001)
Taq DNA Polymerase (5U/μl), (Invitrogen; Cat. No. 10342-020)
Trypsin-EDTA (0.05%; Gibco; Cat. No. 25300-54)

4.2 Methods

4.2.1 Molecular biology

4.2.1.1 Plasmid DNA amplification and purification

For the transformation of *E.coli* XL-1 Blue bacteria 1 μg of plasmid DNA was mixed with 50 μl of competent bacteria cells and incubated on ice for 5 min. For the heat shock, the tubes were placed in a water bath of 42°C for 60 seconds and chilled on ice for 2 min. Afterwards 250 μl of SOC medium (0.5% yeast extract, 2% tryptone, 10 mM NaCl, 2.5 mM KCl, 10 mM MgCl₂, 10 mM MgSO₄, 20 mM Glucose, pH 7.0) were added and incubated at 37°C for 1 h while shaking at 600 rpm. Then, 50 μl of this mixture were plated on LB agar (1% NaCl, 1% tryptone, 0.5% yeast extract, 1.5% agar, pH 7.0) containing antibiotics according to the resistance marker encoded by the plasmid DNA to be amplified. LB agar plates were incubated at 37°C overnight. The next day, a single colony was inoculated in 100 ml LB medium (1% NaCl, 1% tryptone, 0.5% yeast extract, pH 7.0) supplemented with antibiotics for the selection of resistant bacteria cells expressing the desired DNA plasmid. Bacteria were grown at 37°C while shaking overnight.

For the purification of plasmid DNA the kit ‘NucleoBond® Xtra Midi’ was used according to the instructions of the manufacturer. Following alkaline lysis of bacteria the plasmid DNA was purified on an anion-exchange column. Eluted plasmid DNA was precipitated with isopropanol, washed with 70% ethanol, dried and resolved in an appropriate volume of TE-

buffer (10 mM Tris-HCl pH 7.5, 1 mM EDTA). DNA concentration and purity were determined by absorbance measurements at 260 nm and 280 nm.

4.2.1.2 Mouse genotyping

DNA was extracted from tail biopsies by the HotSHOT method (Truett et al. 2000). Briefly, a 0.2 mm-tail biopsy was incubated with 75 μ l of alkaline lysis buffer (25 mM NaOH, 0.2 mM EDTA) for 30 min at 95°C while shaking. Samples were neutralized with 75 μ l of neutralization buffer (40 mM Tris-HCl). For PCR genotyping, 1.5 μ l DNA were used in a single PCR mix containing Taq-DNA polymerase, dNTPs, MgCl₂, PCR buffer and three allele-specific primers with the following sequence written 5' to 3': accccatagttcactactaggc, cgtaacagaggttggtgagg and catggcaatgacattctcc. The amplification was carried out in a PCR thermal cycler using the following program: 5 min at 95°C, 35 cycles of 30 s at 95°C, 30 s at 55°C and 45 s at 72°C followed by a final 10 sec extension step at 72°C. The amplified DNA fragments were mixed with an appropriate volume of 5x DNA loading buffer (30% glycerine, 0.25% bromophenol blue, 0.25% xylencyanol) and separated in a 2% agarose gel containing ethidium bromide and documented under UV light. A product size of 280 bp was obtained for the wild-type allele and a 420-bp-amplicon for the *Fam134b* knockout allele.

4.2.2 Primary cultures and continuous cell lines

4.2.2.1 Maintenance of cell lines

Eukaryotic cell lines (listed in chapter 4.1.2, Table 1) were cultured at 37°C under an atmosphere of 5% CO₂ in cell culture medium (Dulbecco's Modified Eagle Medium (DMEM) supplemented with 10% fetal bovine serum (FBS) and penicillin-streptomycin (P/S)).

The adherent cells were split every 2 to 3 days at a confluency of 80 to 90% in order to avoid overgrowth. To split the cells, cell culture medium was removed and the cell layer was gently rinsed with phosphate-buffered saline (PBS) to remove traces of serum. Trypsin/EDTA-solution was pipetted onto the cell layer and incubated at 37°C for 3 min. By adding prewarmed cell culture medium trypsinization was stopped and cells were dispersed. Appropriate aliquots of cell suspension were transferred into flasks according to the required split ratio.

For storage, cells were suspended in freezing medium (40% DMEM, 50% FBS and 10% DMSO) and aliquoted into freezing vials at a density of about $2 \cdot 10^6$ cells/ml. For a slow cooling process, freezing vials were placed in an isopropanol-freezing container and placed

to -80°C for 24 h. At the next day, vials were transferred into a nitrogen tank for long-term storage. Thawing of cells was performed rapidly by incubation in a water bath at 37°C. Afterwards cells were washed immediately and resuspended in fresh prewarmed cell culture medium.

4.2.2.2 Transient protein expression in mammalian cells

For transient protein overexpression, cells were transfected with plasmid DNA (see Table 2) using Lipofectamine®2000 transfection reagent. Cells were seeded and allowed to reach about 80% confluency while maintained in cell culture medium. Then, cells were transfected with 1 µg of plasmid DNA per well of a 24-well plate or with 10 µg DNA per 10-cm-culture dish. For each microgram of transfected DNA, 1.5 µl of Lipofectamine®2000 transfection reagent were used. The lipofectamine dilution was prepared in Opti-MEM® (Minimum Essential Medium) and was added to the same volume of DNA dilution in Opti-MEM®. The mixture was incubated at room temperature (RT) for 20 min allowing formation of liposomes that entrap the DNA. Cell culture medium of cells was replaced by fresh cell culture medium. The transfection mixture was added drop-wise to the cells and incubated for further 24 h to 48 h under normal cell culture conditions.

4.2.2.3 Preparation of mouse embryonic fibroblasts (MEFs)

MEFs were prepared from *Fam134b* wild-type and knockout embryos at embryonic day 13.5 (E13.5). Brain, eyes and organs of the embryos were removed and the residual tissue was washed in PBS and placed into a Petri dish each. Then, the tissue was minced using a sterile razor blade. 2 ml of DMEM supplemented with P/S were added to each dish. The tissue suspension was homogenized by careful pipetting and triturating with a syringe equipped with needles of the following decreasing diameters: 0.90, 0.80, 0.7, 0.6, 0.55 and 0.4 mm. Afterwards, 5 ml of 0.05% trypsin/EDTA containing DNaseI (80 µg/ml) were added to each sample and incubated at 37°C for 10 min. The supernatant containing dissociated cells was transferred carefully into a new tube. The remaining suspension was incubated with fresh trypsin solution containing DNaseI and incubated for further 10 min at 37°C. Incubations were repeated until a total volume of 40 ml per sample was collected. Cells were pelleted by centrifugation for 10 min at 240g and resuspended in 2 ml of MEF plating medium (DMEM supplemented with 20% FBS, 1.2% MEM, P/S). Cells were counted and $5 \cdot 10^6$ cells were seeded in 20-cm-dishes.

4.2.2.4 Isolation and culture of primary DRG neurons

Adult mice were sacrificed via cervical dislocation. Dorsal root ganglia (DRGs) were manually isolated from the spinal cord and rinsed three times with Hank's buffered salt solution (HBSS) followed by an incubation in collagenase solution (3 mg/ml dissolved in HBSS) for 1 h at 37°C. Activated trypsin was added to a final concentration of 0.1% and DRGs were incubated for further 10 min at 37°C. DRGs were washed three times with HBSS and dissociated by pipetting with BSA-blocked glass Pasteur pipettes of decreasing diameters. In detail, with a glass pipette of normal diameter (1.2 mm) DRGs were pipetted about 10 times up and down till the solution appeared homogenous. The smaller diameter (fire-polished) pipette was used 8x and finally the very small diameter (fire-polished) pipette for 3x. The single cell suspension was centrifuged for 5 min at 160g and the supernatant was removed from the cell pellet. DMEM containing 10% horse serum was added to the cell pellet and again centrifuged for 5 min at 160g. The supernatant was carefully removed and cells were resuspended in primary cell culture medium (Neurobasal-A medium supplemented with 2 mM L-Glutamine and 2% B-27®). Cells were plated on poly-L-lysine coated cover slips or in T25 cell culture flasks and placed at 37°C under a 5% CO₂ atmosphere. 30 min after plating, medium was discarded and replaced by fresh medium containing β-NGF (50 ng/ml).

4.2.3 Protein biochemistry

4.2.3.1 Protein extraction from tissues and cultured cells

Confluent cells from 10-cm-dishes were harvested in 500 μl of ice-cold cell lysis buffer (50 mM Tris/HCl pH 8.0, 120 mM NaCl, 0.5% (v/v) Nonidet P-40, complete protease inhibitor cocktail, 1 mM PMSF) and scraped into 1.5-ml-tubes placed on ice. Lysates were mixed well, incubated on ice for 15 min and centrifuged at 16,000g and 4°C for 30 min. The supernatants were transferred into new tubes and stored at -80°C.

For protein extraction from murine tissue, mice were sacrificed and dissected to isolate brain or dorsal root ganglia. DRGs were rapidly frozen in liquid nitrogen and grinded in 100 μl tissue lysis buffer (50 mM Tris, 150 mM NaCl, 1 mM EDTA, 1% Triton X-100, 1 mM Na₃VO₄, 1 mM NaF, 2.5 mM Na₂HPO₄, 2.5 mM NaH₂O₄, complete protease inhibitor cocktail, 1 mM PMSF). Brain tissue was minced and homogenized by 12 strokes with a glass Teflon homogenizer in 2 ml of ice-cold tissue lysis buffer. Then, tissue homogenates were sonicated on ice for 30 min and centrifuged at 3,100g for 10 min to remove cell debris.

Supernatants were collected and the protein concentration of each sample was determined with the Pierce BCA Protein Assay Kit.

4.2.3.2 Subcellular fractionation

Whole mouse brains were dissected, weighed and rinsed with PBS. Brain tissue was minced and homogenized by 12 strokes with a glass Teflon homogenizer in 2 ml of ice-cold homogenisation buffer (130mM KCl, 25 mM Tris/HCl pH 7.4, 1 mM EGTA, complete protease inhibitor cocktail). Postnuclear fractions were prepared by centrifugation at 1,000g for 10 min at 4°C. The remaining supernatants were centrifuged at 10,000g for 15 min at 4°C. Supernatants were loaded on discontinuous iodixanol gradients (from bottom to top: 30%, 25%, 20%, 15%, 12.5%, 10%, 7.5%, 5%, 2%) and centrifuged at 130,000g for 40 min at 4°C using a ultracentrifuge (Optima™ L-100 XP BioSafe; Beckman Coulter) equipped with a SW-32.1Ti rotor. After centrifugation, 1500- μ l fractions were carefully decanted from the top of the tube and each sample was diluted with homogenisation buffer to a final volume of 16 ml followed by ultracentrifugation at 130,000g for 40 min at 4°C. Protein pellets were boiled in 50 μ l of 1x SDS-PAGE sample buffer for 5 min and resolved by 10% SDS-PAGE. The samples were probed for subcellular marker proteins and for Fam134b by Western blotting.

4.2.3.3 Co-immunoprecipitation

For co-immunoprecipitation (co-IP) studies HEK293T cells were seeded and transfected by the lipofectamine method as described in chapter 4.2.2.2. After one day, cells were treated with 50 μ M Chloroquine overnight or left untreated. At day two after transfection, cells were lysed according to the protocol described in chapter 4.2.3.1. The supernatants were transferred in new tubes and 25- μ l-aliquots were taken. Aliquots were immediately supplemented with the appropriate amount of 6x SDS-PAGE sample buffer (6% SDS, 33% β -mercaptoethanol, 40% (v/v) glycerol, bromphenol blue), incubated at 95°C for 5 min and stored at -20°C as input samples. The remaining protein samples were incubated with antibody-coupled beads with specificity according to the tags of transiently expressed proteins favored for immunoprecipitation (IP). For this purpose, beads were washed three times with 1 ml of cell lysis buffer. After each wash, beads were pelleted for 1 min at 1000g and 4°C and the supernatants were discarded. Finally, fresh lysis buffer was added to the beads and the bead-buffer-suspension was pipetted to the cell lysates. The IP-samples were incubated on a rotating wheel at 4°C overnight. Next day, beads were washed three times with 1 ml of cell

lysis buffer on ice. The supernatants were carefully removed and pelleted beads were mixed with 25 μ l of 6x SDS-PAGE sample buffer. By subsequent incubation at 95°C for 5 min precipitated proteins were eluted from the beads and the supernatants were subjected to SDS-PAGE and Western blotting.

4.2.3.4 SDS-PAGE and Western blotting

Protein lysates were mixed with an appropriate volume of 6x SDS-PAGE sample buffer (6% SDS, 33% β -mercaptoethanol, 40% (v/v) glycerol and bromophenole blue) and boiled at 95°C for 5 min. The proteins were separated by SDS-polyacrylamide gel electrophoresis (SDS-PAGE) according to their size together with a molecular size marker (PageRuler, Thermo Scientific). SDS-gels consisting of stacking and separating gel were run with electrode buffer (25 mM Tris, 250 mM Glycine, 0.1 % SDS) at 15 mA for 15 min followed by running at 100 V constantly per gel with a Mini-PROTEAN®3 System (Biorad). After electrophoresis, the separated proteins were transferred to a PVDF membrane (Amersham Hybond™ (0.45 μ m), Cat.No. 106000023) by a wet-blot system in transfer buffer (25 mM Tris base, 192 mM glycine, 20% methanol). The Western blot sandwich was assembled and contained three pieces of Whatman filter paper overlaid by a methanol-activated PVDF membrane, the SDS-gel and another three pieces of Whatman filter paper. The transfer was performed at 280 mA for 90 min. Afterwards, unoccupied membrane sites were blocked by incubation in blocking solution containing 1% BSA in Tris-buffered saline supplemented with 0.1% Tween 20 (TBS-T) at RT for 1 h. Then, the membrane was incubated in primary antibody solution (1% BSA, primary antibody (diluted as listed in table 4), 0.05 % NaN₃ in TBS-T) under gentle agitation at 4°C overnight. The next day, the membrane was washed three times with TBS-T for 10 min followed by an incubation in secondary antibody solution (TBS-T containing 1% BSA and secondary antibody diluted 1:4,000) at RT with agitation for 60 min. After three more washing steps in TBS-T at RT for 10 min, immunodetection was performed by enhanced chemiluminescence (ECL). The membrane was incubated with ECL substrate for 1 min. Horseradish peroxidase that is linked to the secondary antibody cleaves the chemiluminescent agent producing luminescence. The luminescence was detected by the LAS 4000 imaging device (GE Healthcare). For reprobing, the membranes were washed three times with TBS-T for 10 min followed by incubation in another primary antibody solution.

4.2.3.5 Immunocytochemistry

Cultured cells on cover slips were fixed with fixative solution (4% paraformaldehyde (PFA) in PBS, pH 7.4) at RT for 15 min. Fixed cells were rinsed three times with PBS for 5 min followed by permeabilization with PBS containing 0.25% Triton-X incubated at RT for 15 min. Then, cells were incubated with blocking solution (PBS containing 0.25% Triton-X and 5% normal goat serum) at RT for 1 h and incubated with primary antibody diluted in blocking solution (antibody-specific dilutions see Table 3 of chapter 4.1.5) at 4°C overnight. For co-stainings, a mixture of primary antibodies was applied. The next day, cells were washed three times with PBS for 10 min each. Afterwards, goat secondary antibodies conjugated either with Cy5, Alexa Fluor-488, Alexa Fluor-555 or Alexa Fluor-546 directed against the species of the respective primary antibody were applied as 1:1,000 dilutions in blocking solution. The secondary antibodies were incubated at RT for 1 h followed by a washing step with PBS. Nuclei were stained with Hoechst-33258 (1:10,000 in PBS) and the cells were washed three times with PBS. Finally, cover slips with stained cells were mounted with Fluoromount-G (SouthernBiotech) on microscope slides and analyzed with a Leica TCS SP5 confocal scanning fluorescence microscope equipped with a 63x objective.

4.2.4 Fam134b topology assay by fluorescence live cell imaging

Fluorescence protein protection assay was carried out with COS-7 cells seeded on cover slips. Cells were transiently transfected with FAM134B-GFP (C-terminal GFP-tag), GFP-FAM134B (N-terminal GFP-tag), CD3-RFP or RFP-KDEL expressing plasmids. The lipofectamine-transfection was performed as described in chapter 4.2.2.2. 24 h after transfection, cell cultures on cover slips were transferred into a heated perfusion chamber (37°C) fitting into the desk of an inverted microscope (Axio Observer Z.1; AxioCam MRm, Zeiss) equipped with a 20x objective. Cells were kept in live-cell buffer (50 mM HEPES, 23 mM NaCl, 3 mM MgCl₂, 100 nM CaCl₂, 1 mM EGTA, 107 mM Glutamate, 1 mM ATP, 2 mM DTT) and the live cell recording was started by collecting images every 20 s. Cells were treated with digitonin (18 µM in live cell buffer) for 80 sec in order to permeabilize the plasma membrane followed by an incubation in live-cell buffer without additives for 80 sec. Then, trypsin (1 µM in live cell buffer) was added to the cells, which digests fluorescent protein tags of membrane proteins facing the cytosolic compartment, whereas the fluorescence of intraorganellar located protein-tags is unaffected. After live cell imaging for 10 min in total, the recordings were stopped. ImageJ Software was used for fluorescence

quantification measurements. Mean fluorescence values of single cells were subtracted from background fluorescence and normalized to fluorescence at the starting time point.

4.2.5 Liposome-shaping assay

The liposome-shaping assay was performed by Dr. N. Koch at the Institute of Biochemistry, Jena University Hospital. For freeze-fracture experiments, 1 mg of liposomes was incubated with 5 μ M protein in liposome buffer containing 0.3 M sucrose for 15 min at 37°C. Small aliquots (1 to 2 μ l) of vesicle suspension were freeze-fractured. The samples were examined using an EM 902 A electron microscope (Zeiss). Images were acquired using a 1k FastScan CCD camera (TVIPS). Diameters of approximately 1600 to 2600 liposome structures per incubation condition were determined using the ImageJ software.

4.2.6 Mouse studies

Studies were performed in a mixed 129SvJ/C57BL/6 background in the F4 and F5 generation of C57BL/6-backcrossing. All animal experiments were approved by the local administrative institution (Thüringer Landesamt für Verbraucherschutz, Bad Langensalza, Germany) and the experimental procedures were performed in accordance with the guidelines established by the animal welfare committee of the State of Thuringia.

4.2.6.1 Behavioural tests for nociception

Thermal stimulation at 45°C was applied to the tail of adult male mice after their habituation to the test environment using the water immersion method (Le Bars et al. 2001). The time from onset of stimulation to rapid movement of the tail was recorded. Two trials with two separate measurements of tail-flick latency per mouse were averaged. Statistical comparisons of two groups of data were made using the Mann-Whitney-U-test. The experimenter was blinded to the genotype of the mice.

4.2.6.2 Nerve conduction studies

Nerve conduction studies were carried out by Dr. Lutz Liebmann to examine sensory function *in vivo*. Mice were anesthetized and the body temperature was maintained with a warming pad. Tail sensory nerve conduction velocities (TSNCVs) were recorded 30 mm proximal to the stimulation electrode. Sensory action potentials were evoked with increasing intensities (0-10 V, increment 1 V, 50 μ s duration). Electrodes with a tip diameter of 1-2 μ m and an impedance of 0.1 M Ω were used (WE30030.1H10, Science Products). Signals were processed

with an extracellular amplifier (EXT 02F, NPI; high-pass filter: 3 Hz, low-pass filter: 2 kHz). The sample frequency was 20 kHz. For analysis the software Signal 3 (CED) was used. TSNCVs were calculated by dividing the distance by the take-off latency of 5 averaged sensory potentials. Amplitudes were determined from peak to peak.

4.2.6.3 Histological sample preparation

Murine tissue was fixed by *in vivo* perfusion with fixative solution containing 4% PFA in PBS. The spinal cord and the 4th lumbal DRGs were isolated and post-fixed overnight at 4°C in fixative. After washing with PBS and dehydration in 30% sucrose in PBS at 4°C ON, the ganglia and spinal cord samples were cryosectioned with a thickness of 10 µm (Leica CM 1850 cryostat). The tissue sections were placed on adhesion slides (Histobond Marienfeld; Cat. No. 0810401) and stored at -20°C. For semithin sectioning the fixative solution contained 4% PFA and 1% glutaraldehyde (GA) in PBS. The fixed tissue was delivered in cacodylate buffer (0.2 M cacodylate buffer, pH 7.4) to the electron microscopy facility of the Jena University Hospital for further processing. Richardons's staining (10x Richardson's stock solution: 1% methylene blue, 1% azure II in 1% borax) was applied for the semithin-sections.

4.2.6.4 Cresyl violet staining

Rehydrated spinal cord paraffin sections with a thickness of 10 µm were stained according to the cresyl violet staining protocol. For this purpose, cresyl violet staining solution (0.03% cresyl violet w/v, 0.2 M v/v glacial acetic acid, 0.1 M sodium acetate) was filtered and prewarmed up to 60°C. The sections were incubated with staining solution for 10 min in cuvettes and dehydrated in an ascending alcohol series of 70%, 96%, and 100% ethanol for two times for 3 min at each step. Finally, sections were incubated two times for 5 min in xylene and mounted with permanent mounting medium. Images were taken with an inverted microscope (Axio Observer Z.1; AxioCam MRm, Zeiss) and purple-blue Nissl-stained motoneuron cell bodies in the ventral horn were quantified.

4.2.6.5 Immunohistochemistry

Tissue cryosections on adherent microscope slides were placed in PBS and transferred into Shandon coverplates (Thermo Scientific; Cat. No. 72110017). The staining protocol for tissue sections was identically equal to the protocol for fixed cells on cover slips as described in chapter 4.2.3.5. After staining according to the protocol for immunocytochemistry,

microscope slides were removed from Shandon coverplates by submersion in PBS. Slides were mounted with Fluoromount-G (SouthernBiotech) and cover slips and analyzed with a Leica TCS SP5 confocal laser scanning microscope equipped with a 40x objective. The number of p62-positive immunofluorescent puncta was analyzed using the ImageJ software. The threshold was set to exclude the cytosolic background fluorescence allowing selective analysis of immune-positive puncta representing autophagosomes. Sensory neuron somata were analyzed if the cell nucleus was in plane of the section and outlined manually. The numbers of p62-puncta and the cell area of sectioned DRG somata were measured.

4.2.6.6 Ultrastructural analysis of primary sensory neurons and tissue

Electron microscopy of DRG and spinal cord tissue samples were performed at the RWTH Aachen University Hospital at the Institute of Neuropathology by Dr. I. Katona and Prof. Dr. J. Weis. DRG and spinal cord tissue was fixed in 4% glutaraldehyde (GA) and post-fixed with osmium tetroxyde. Ultrathin sections were treated with uranyl acetate and lead citrate and viewed with a Philips CM10 transmission electron microscope.

Ultrastructural analysis of primary sensory neurons was performed at the University Medical Center Utrecht by Dr. M. Mair and Prof. F. Reggiori. A monolayer culture DRG neurons was fixed in 0.1 M cacodylate buffer containing 2.5% GA and 2% PFA at RT for 2 h. Fixed samples were sent to Utrecht and embedded in Epon resin in cell culture flasks following the flat embedding procedure. After Epon resin polymerization at high temperature, the embedded material was stripped off the plastic flask using needle-nose pliers and forceps. Small specimens (appr. 0.5 cm in diameter) of Epon-embedded material were cut using a drill bit (mounted with a rotating cutting tool) and glued onto ultra-microtome supports. Ultrathin serial sections of 50 nm were cut parallel to the neuron monolayer using an ultra-microtome (Leica Microsystems) and transferred onto Formvar carbon-coated copper grids for staining using the EM AC-20 contrasting instrument (Leica Microsystems).

4.2.7 Statistical analysis

Data are presented as mean \pm SEM in the figures. The statistical test applied for *p*-value calculation is noted in the legends of the respective figures. One- or Two-way ANOVA or parametric two-tailed Student's *t*-test were applied after confirming a parametric distribution by Normal Q-Q-Plots. For non-parametric distributed data, the Mann-Whitney-U-test was applied. Levels of significance were set as following: *** $p < 0.001$; ** $p < 0.01$, * $p < 0.05$.

5 Results

The results section is divided into three parts. In the first part, the results of the detailed phenotypic characterization of transgenic *Fam134b* knockout mice are described. The second and third part contains data of the *Fam134b* biochemical and functional approaches.

5.1 Phenotypic characterization of *Fam134b* knockout mice

5.1.1 Phenotype assessment and knockout verification

The *Fam134b* homozygous knockout (KO) mice were viable, fertile and did not show an increased mortality compared to their wild-type (WT) littermates. The knockout of *Fam134b* was verified by immunodetection of the *Fam134b* protein, which has an electrophoretic mobility close to the molecular weight marker of 70 kilodaltons (kDa). The *Fam134b*-specific protein band was observed exclusively in tissue lysates prepared from *Fam134b* wild-type but not *Fam134b* knockout mice (Figure 8). *Fam134b* knockout mice were born at the expected Mendelian ratio from heterozygous breedings, indistinguishable from *Fam134b* wild-type mice and did not show apparent abnormalities or deficits until 24 months of age.

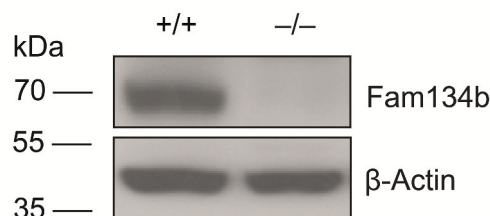


Figure 8: Protein expression of *Fam134b* in mouse embryonic fibroblasts

Endogenous *Fam134b* expression was analyzed in lysates of mouse embryonic fibroblasts (MEFs) derived from *Fam134b* wild-type (+/+) and *Fam134b* knockout (-/-) mice at embryonic day 13.5. Primary MEFs were lysed after passage 3, subjected to SDS-PAGE and processed for immunoblot analysis. *Fam134b* was observed as a sharp band that migrates at approximately 70 kDa. The specificity of *Fam134b* detection was confirmed by the absence of the observed protein band in MEFs of *Fam134b* knockout mice. Immunodetection of β -Actin served as loading control.

5.1.2 Analyses of peripheral sensory function *in vivo*

Two different experimental approaches were followed to investigate whether *Fam134b* knockout mice show impaired sensation. Based on previous findings that human patients with mutations in the *Fam134b* gene suffer from a sensory neuropathy (Kurth et al. 2009), a behavioural test for nociception was conducted. For this purpose, the latency from onset of thermal stimulation at 45°C of the mouse tail until rapid movement of the tail was recorded.

In comparison to other approaches, the tail-flick assay is a simple test with an end-point-detection. The tail-flick test has a high reproducibility because the readout is a simple reflex instead of a complex behavioural response. Briefly, the noxious heat stimulus was applied by water-immersion in contrast to the more common radial application of heat by an intense light beam. This experimental set up has the advantage that it is independent of the tail pigmentation pattern which can affect tail flick latencies triggered by radiant light (Wen et al. 2009).

Additionally, nerve conduction studies were carried out by Dr. Lutz Liebmann to examine the sensory function *in vivo*. For this purpose, electrical stimuli were delivered to the nerves of the distal tail of anaesthetized animals, predominantly activating the large-caliber nerve fibers. The responses were recorded at the tail base and the respective results are summarized in Figure 9.

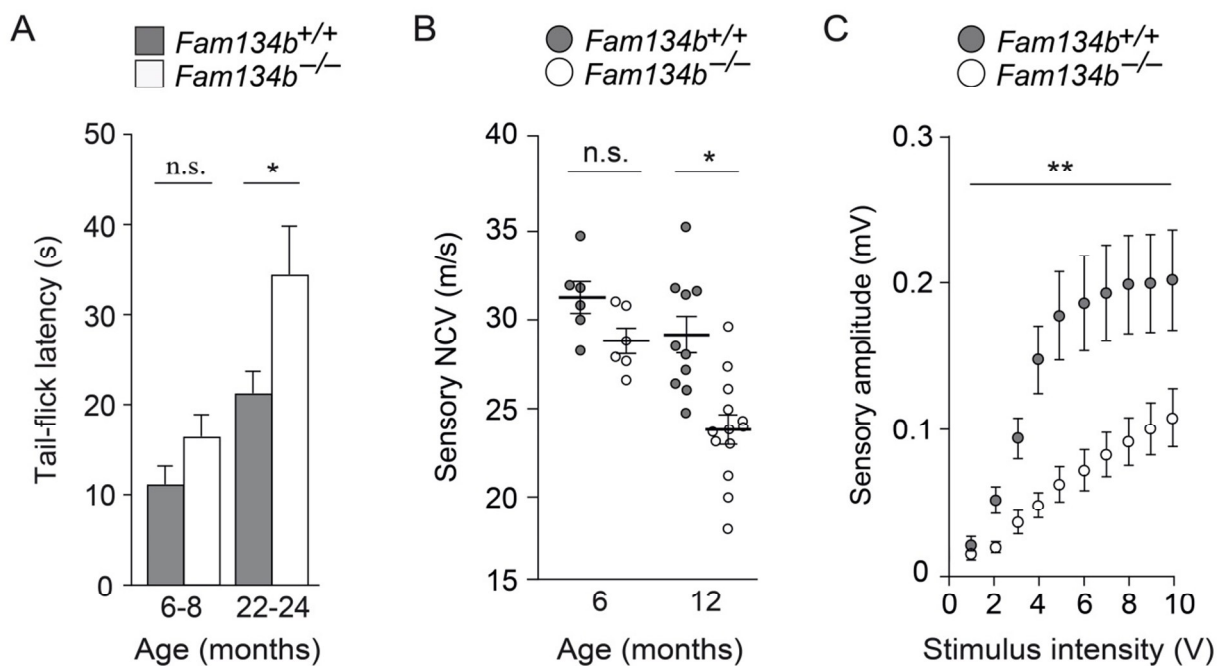


Figure 9: Sensory function in *Fam134b*-deficient mice

(A) *Fam134b* wild-type (+/+) and knockout (-/-) mice were subjected to the tail-flick test. The latency time from thermal stimulation of the caudal part of the tail in a water bath heated at 45°C to flicking of the tail was measured. Two trials with two measurements each were averaged for each mouse. (n=13 for +/+, n=11 for -/-) Parametric distribution was not confirmed by Normal Q-Q-Plots, so the Mann-Whitney-U-Test was applied. (B) Sensory nerve conduction velocities (NCVs) were recorded from the tail by stimulating distally and recording proximally. (n=6 for +/+ and -/- at 6-8 months; n=10 for +/+ and n=13 for -/- at 12 months). Statistical test: one-way ANOVA (C) Input-output curves of sensory nerve amplitudes at 12 months of age (n=10 for +/+ and n=13 for -/-). Statistical test: two-way ANOVA. n=number of animals. Results are expressed as mean ± SEM.

The tail-withdrawal latencies of *Fam134b* knockout mice were comparable with that of wild-type mice at an age of six to eight months, whereas a 62.5% increase of the latency time was detected in 2-year-old *Fam134b*-deficient animals compared to wild-type littermates (Figure 9A). These results are consistent with the nerve conduction studies of sensory nerves of the tail showing a decline in sensory function in *Fam134b* knockout mice at an age of 12 months. In detail, sensory nerve conductance velocities (NCVs) illustrated in Figure 9B correspond to the speed at which an action potential is propagated along an axon. NCVs were significantly decreased by 22.5% at 12, but not 6 months of age in knockout mice. The sensory NCV is predominantly dependent on axon diameter and myelination, whereas the sensory amplitude which is the height of the peak of a recorded action potential mainly depends on the axon number. Sensory amplitudes were measured for each evoked fast response of large diameter axons with increasing stimulus intensities and were found severely reduced in 12-month-old *Fam134b* knockout mice (Figure 9C). Thus, a progressive loss of large diameter axons in *Fam134b* knockout mice was assumed. Furthermore, the decreased NCVs indicated a degeneration of the myelin sheath. In contrast, the tail-flick reflex as a measure of nociception evaluates rather small-caliber A δ - and C-fibers, which are sensitive to the stimulation by noxious heating at 45°C (Cain et al. 2001). Taken together, both nociceptive behaviour and nerve conduction studies addressing peripheral nerve function of afferent fibers *in vivo*, present strong evidence for a progressive sensory dysfunction of *Fam134b* knockout mice.

5.1.3 Histological analysis of afferent sensory fibers

Based on the results from the phenotypic characterization described in the previous section, it was assumed that the number of afferent sensory fibers might be reduced in aged *Fam134b* knockout animals. In order to address this issue, several approaches to quantify afferent fibers in mouse tissue were considered. With regards to technical obstacles and the requirement of high reproducibility for analyzing sensory fibers in animals at different ages, cross-sectioning of the distal processes of dorsal root ganglia (DRG) turned out to be the appropriate method to determine even slight quantitative changes. As illustrated in Figure 10A, nerve fibers of peripheral nociceptors projecting to spinal cord neurons are bundled before entering the ganglia where the cell somata of sensory neurons are located. Embedding of dissected 4th lumbar DRGs from mice followed by cross-sectioning of preganglionic sensory fibers (see exemplary sections in Figure 10B) enabled us to precisely count axons. The resulting data is illustrated in Figure 10C and indeed revealed a significantly reduced sensory axon number in

2-year-old knockout mice, whereas 6-8-month-old knockout mice showed afferent axon numbers comparable to their *Fam134b* wild-type littermates. However, the determined axon count in 2-year-old knockout mice was declined by 7% only. It is assumed that the effect of sensory fiber loss might be more pronounced at distal regions, but there a precise quantification is technically difficult.

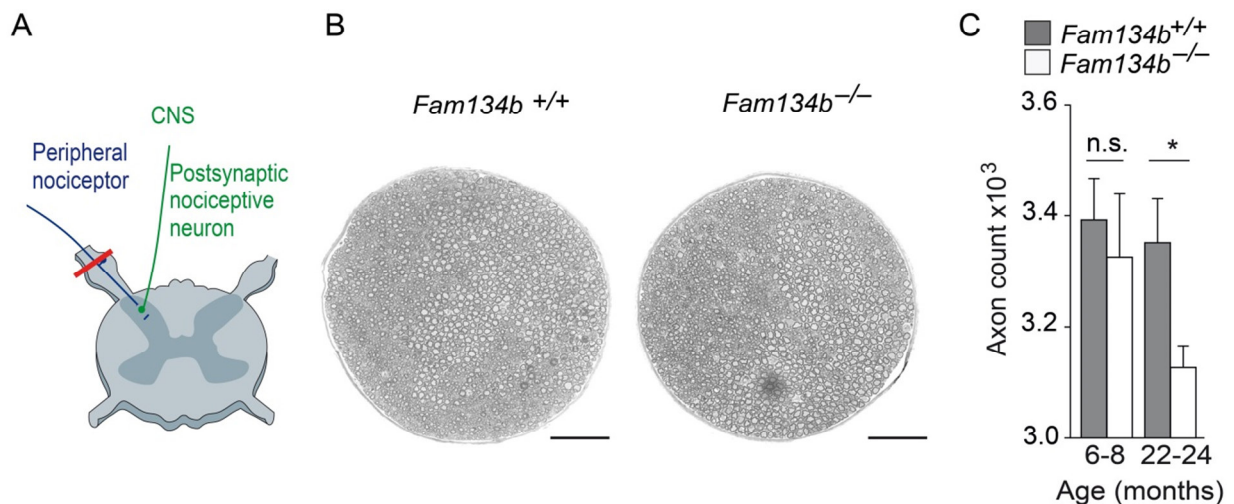


Figure 10: Quantification of afferent sensory axon number

(A) Schematic illustration of the specific site for cross-sectioning (red bar) preganglionic afferent axon fiber bundles distal to the 4th lumbar (L4) dorsal root ganglion (DRG). (B) Representative bright field microscopy images of semithin-sections stained with Richardson's Blue following *in vivo* mouse perfusion with fixative and L4 DRG isolation from *Fam134b* wild-type (+/+) and *Fam134b* knockout (-/-) mice (Scale bars: 200 μ m). (C) Sensory axon numbers analyzed from semithin cross-sections that are shown in (B). Afferent sensory axons were counted using the ImageJ software. (n=3 for +/+ and -/- at 6-8 months; n=4 for +/+ and -/- at 22-24 months). Results are expressed as mean \pm SEM. Statistical test: Student's *t*-test. n=number of animals.

5.1.4 Ultrastructural analysis of sensory neurons

Since *Fam134b*-deficient mice showed progressive sensory dysfunction and afferent fiber loss, we asked whether any cellular pathologies can be observed even prior to the late sensory phenotypic disease onset. To address this question, electron microscopy (EM) was used to search for morphological alterations that may hint for the underlying pathophysiological mechanisms causing sensory neuron dysfunction in *Fam134b* knockout mice. First, the ultrastructure of DRG tissue sections from 11-month-old mice was analyzed in collaboration with Dr. I. Katona and Prof. Dr. J. Weis (Aachen). The architecture of cellular organelles in the somata of sensory neurons was studied by EM. Strikingly, aberrant expansions of the endoplasmic reticulum (ER) and remarkable dilations of Golgi cisternae were present in a subset of cells of knockout mouse tissue. The transmission electron microscopy (TEM)

images of those findings are summarized in Figure 11. Images of Figure 11A and B show the ER compartment with prominently enlarged ER tubules that were exclusively observed in tissues from *Fam134b* knockout mice. Similarly, Figure 11C and D illustrate the Golgi apparatus with enlarged and distended cisternae in some of the DRG somata from knockout mouse tissue, but normal tightly stacked cisternae with narrow intraluminal spaces arranged in stacked arrays in tissues from wild-type mice. No obvious abnormalities were observed in other subcellular compartments.

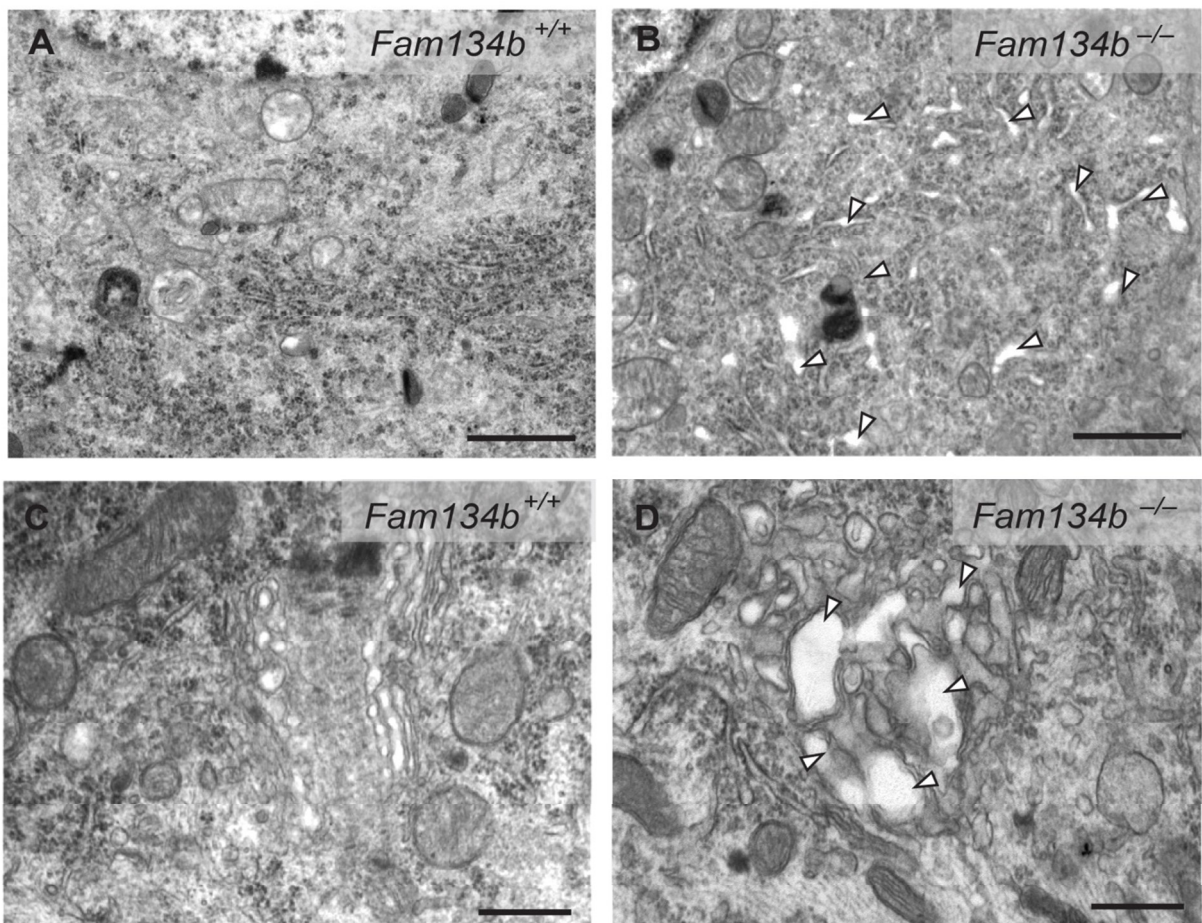


Figure 11: Ultrastructural analysis of DRG somata from mouse tissue sections

Transmission electron microscopy (TEM) images of DRG tissue ultrathin-sections from 45-week-old wild-type (*Fam134b*^{+/+}) and knockout (*Fam134b*^{-/-}) mice. **(A,B)** TEM images of endoplasmic reticulum (Scale bars: 1 μ m) and **(C,D)** Golgi apparatus (Scale bars: 0.5 μ m). Images are representative for three individual mice for each genotype. Enlarged organelles observed in DRG somata of knockout mice are indicated by white arrowheads. Images were taken using a Philips CM10 transmission electron microscope.

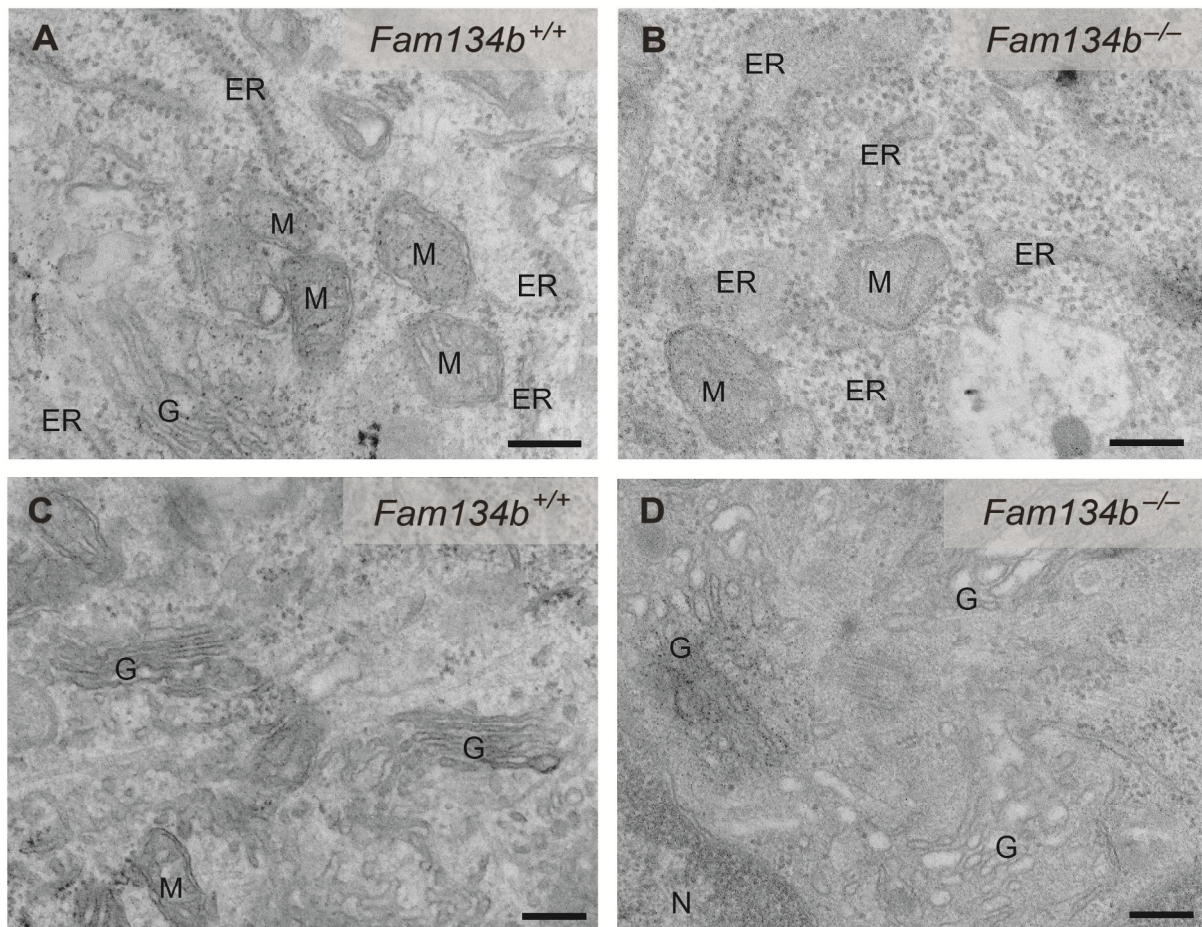


Figure 12: Ultrastructural analysis of DRG somata from primary neuronal cultures

Transmission electron microscopy images of primary sensory DRG neurons from 3-month-old wild-type (*Fam134b*^{+/+}) and knockout (*Fam134b*^{-/-}) littermates subjected to flat embedding after fixation at the second day *in vitro* (DIV=2). (A,B) TEM images of the endoplasmic reticulum adjacent to the nucleus of DRG neurons and (C,D) the Golgi compartment (Scale bars: 200 nm). 25 cells per genotype were analyzed. Cell sections were examined using an 80 kV transmission electron microscope (Jeol 1200-EX). ER, endoplasmic reticulum; G, Golgi apparatus; M, mitochondrium.

Next, a detailed investigation of the neurite ultrastructure was performed to elucidate if similar organellar alterations may exist in afferent axonal processes. By flat embedding of primary sensory neurons grown as monolayer culture, the neuronal architecture was successfully obtained. Embedding of fixed cells, sample processing and TEM imaging was conducted in the EM laboratory led by Dr. F. Reggiori (Utrecht). Both longitudinal and lateral neurite cross-sectioning was facilitated for proper analyses of intra-axonal organelles. Neurites of primary sensory DRG neurons isolated from 3-month-old *Fam134b* wild-type and knockout mice were indistinguishable. However, even though the axonal ultrastructure did not show obvious changes in primary sensory neurons, the ER of the cell somata was swollen in

nearly half of the neurons in *Fam134b* knockout compared to their wild-type littermates. Moreover, Golgi stacks appeared severely distorted in somata of DRGs isolated from knockout mice, but were highly ordered with closely stacked leaflets in primary wild-type DRG neurons. Representative data of those findings are summarized in Figure 12 and closely resemble the ultrastructural changes present in DRG tissue from 11-month-old knockout mice.

5.1.5 Analysis of motoneuron histology and efferent motor function

Because of the sensory dysfunction in 12-month-old *Fam134b* knockout mice, we asked whether motor neurons are affected as well, though *Fam134b* knockout mice did not exhibit an apparent motor phenotype. Firstly, efferent fiber function was assessed by motor NCVs through analyzing the tail compound muscle action potentials (CMAPs). CMAP, which is the summation of individual motor unit action potentials, may indicate efferent axonal impairments (Walsh et al. 2014). Tail distant motor latencies recorded in anesthetized mice *in vivo* are shown in Figure 13 and did not differ between genotypes.

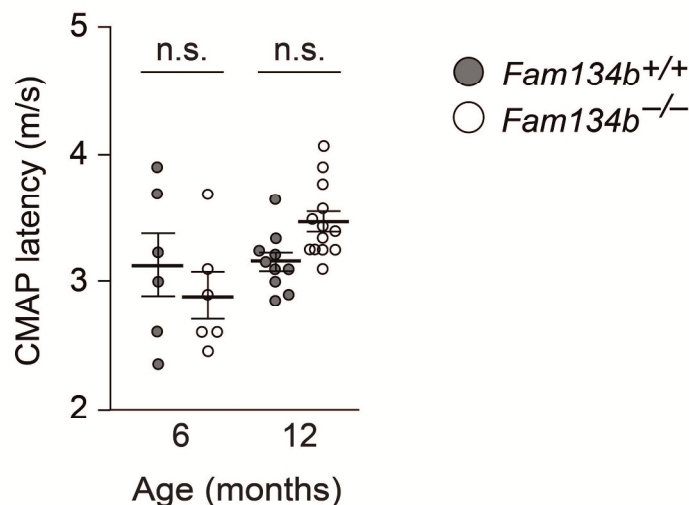


Figure 13: Efferent motor fiber function assessed by CMAP latency

Compound muscle action potential (CMAP) latencies recorded from tail nerves of wild-type (*Fam134b*^{+/+}) and knockout (*Fam134b*^{-/-}) mice at the ages indicated (n=6 for +/+ and -/- at 6 months; n=10 for +/+ and n=13 for -/- at 12 months). Statistical test: one-way ANOVA. n=number of animals. Results are expressed as mean ± SEM.

Motoneuron histology was examined on Nissl-stained spinal cord cross-sections that are illustrated in Figure 14. Neither changes in the appearance of stained motoneuron cell bodies, nor in motoneuron numbers were observed in *Fam134b* knockout mice at an age of 12 and 20

months compared to wild-type littermates. Additionally, the subcellular Golgi and ER compartment in motoneurons exhibited a normal architecture as evidenced by ultrastructural studies (see TEM images shown in Figure 15).

Taken together, loss of *Fam134b* did not affect the peripheral motor system and thus efferent axon function. The observed severe and selective disruption of ER and Golgi apparatus morphology *in vivo* that is characterized by distension of both compartments (described in chapter 5.1.4) seems to be specific for the peripheral sensory system.

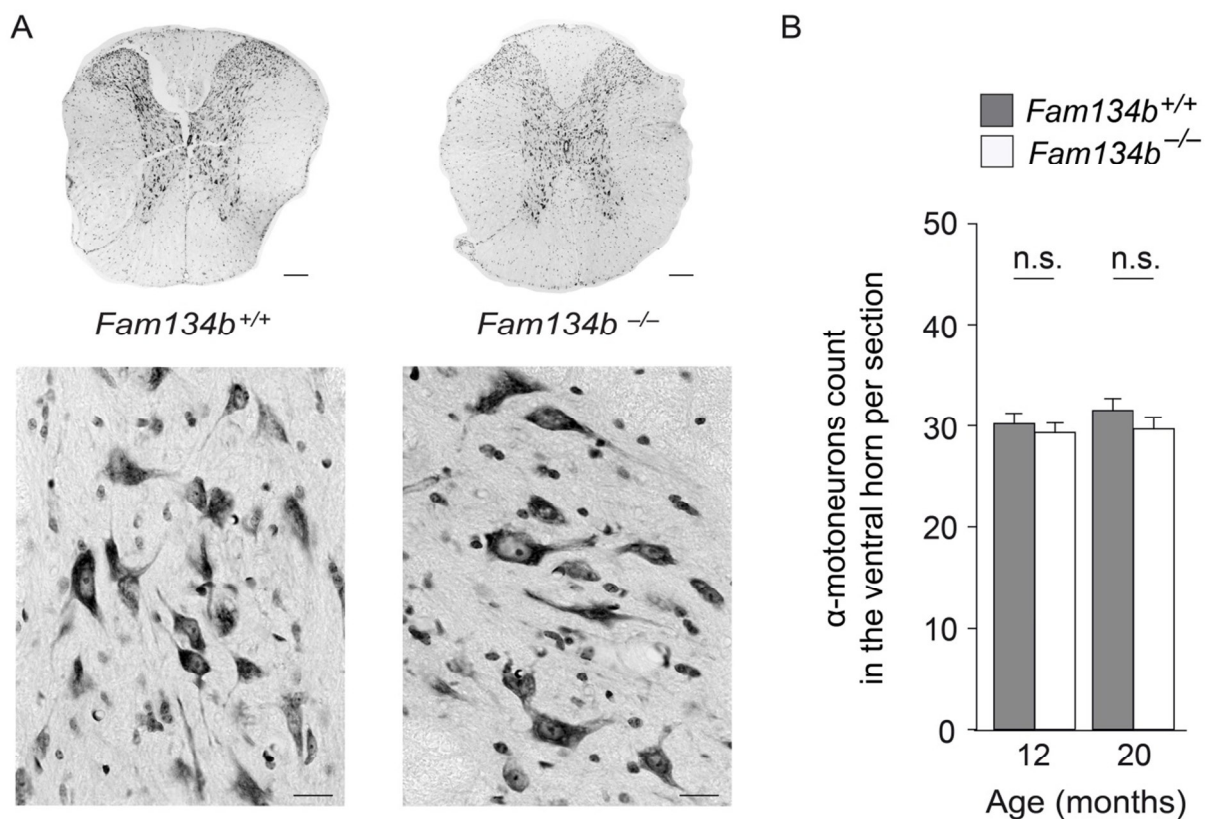


Figure 14: Ventral horn motor neuron histology and quantification

(A) Bright field images of Nissl-stained spinal cord sections of 12-month-old wild-type (*Fam134b*^{+/+}) and knockout (*Fam134b*^{-/-}) mice. Upper panel: Spinal cord cross-sections (10- μ m thick) from thoracic segments (Scale bars: 150 μ m). Bottom panel: The ventral horn region in spinal cord cross-sections showing Nissl-positive α -motoneuron cell bodies (Scale bars: 20 μ m). (B) Quantification of α -motoneurons in sections shown in (A) using ImageJ software. (n=3 for +/+ and -/- at 6-8 months; n=4 for +/+ and -/- at 22-24 months). Statistical test: Student's *t*-test. n=number of animals. Results are expressed as mean \pm SEM.

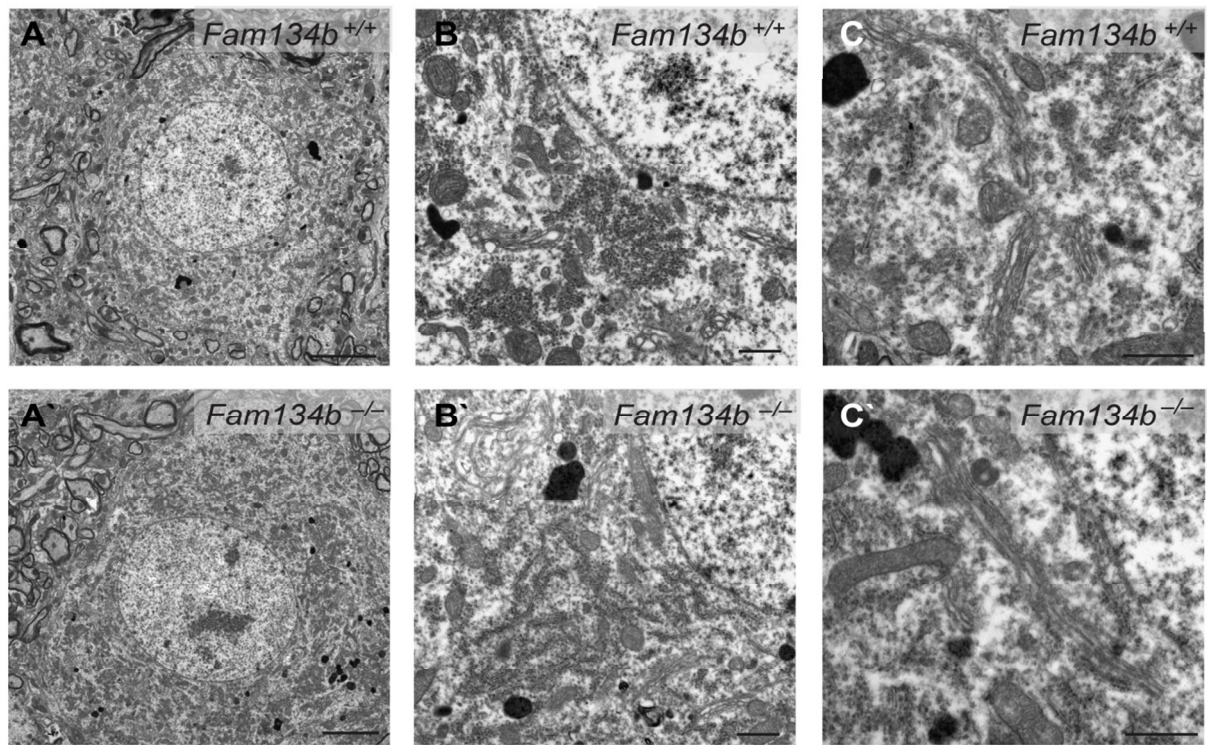


Figure 15: Ultrastructural analysis of motoneurons in spinal cord sections

TEM images of motoneuron cell bodies in ultrathin-sections from 12-month-old mice. (A, A') Images of cell somata are shown (Scale bars: 5 μ m). Higher magnification of (B, B') ER and (C, C') Golgi compartments (Scale bars: 1 μ m). Images were performed using a Philips CM10 transmission electron microscope.

5.2 Cellular localization and protein-interaction partners of Fam134b

5.2.1 Subcellular localization studies

To functionally address the role of Fam134b, its subcellular localization in murine cells and tissue was analyzed. Firstly, the Fam134b protein localization was studied by confocal laser scanning microscopy (CLSM) of mouse embryonic fibroblast cells (MEFs) transiently expressing HA-tagged FAM134B. The cells were co-stained for HA immunoreactivity and different subcellular compartment markers. As illustrated in Figure 16, the HA-signal showed a high density at perinuclear structures and was distributed throughout the cytoplasm in a network-like pattern. In addition, HA-FAM134B co-localized with the Golgi compartment-specific markers GM130 (Nakamura et al. 1995) and Giantin (Linstedt et al. 1995) at the perinuclear region. This is consistent with previous findings from our laboratory identifying Fam134b as a Golgi protein (Kurth et al. 2009). Moreover, double-staining for HA-FAM134B and defined sub-compartment markers revealed a partial co-localization with the ER. In detail, HA-FAM134B overlaps to a high degree with protein disulfide isomerase (PDI), an ER luminal enzyme (Freedman 1989). Similarly, HA-FAM134B overlaps with Reticulon-4 (Rtn4), an ER membrane marker associated with smooth ER tubules (van de Velde et al. 1994). Another established ER-resident marker protein, Climp63, localizes to the rough ER membrane and contributes to the formation of ER sheet-structures (Klopfenstein et al. 2001). The Climp63-positive compartment co-stained with HA-FAM134B as well. Taken together, these data indicate that HA-FAM134B localizes to the ER and Golgi compartment. The relatively broad subcellular fluorescence pattern of FAM134B partially overlaps with the applied markers specific for various ER sub-compartments. However, limitations of this experimental strategy to elucidate the precise localization of FAM134B include the limited resolution of fluorescence microscopy e.g. by confocal blurring or overexpression artifacts due to a transiently high protein level that may lead to ectopic protein expression or even affect the structure of the respective compartments. Additionally, cell-type specific differences in the localization pattern should be considered in highly specialized cells as neurons. For this reasons, another experimental approach was chosen to address the subcellular localization of Fam134b.

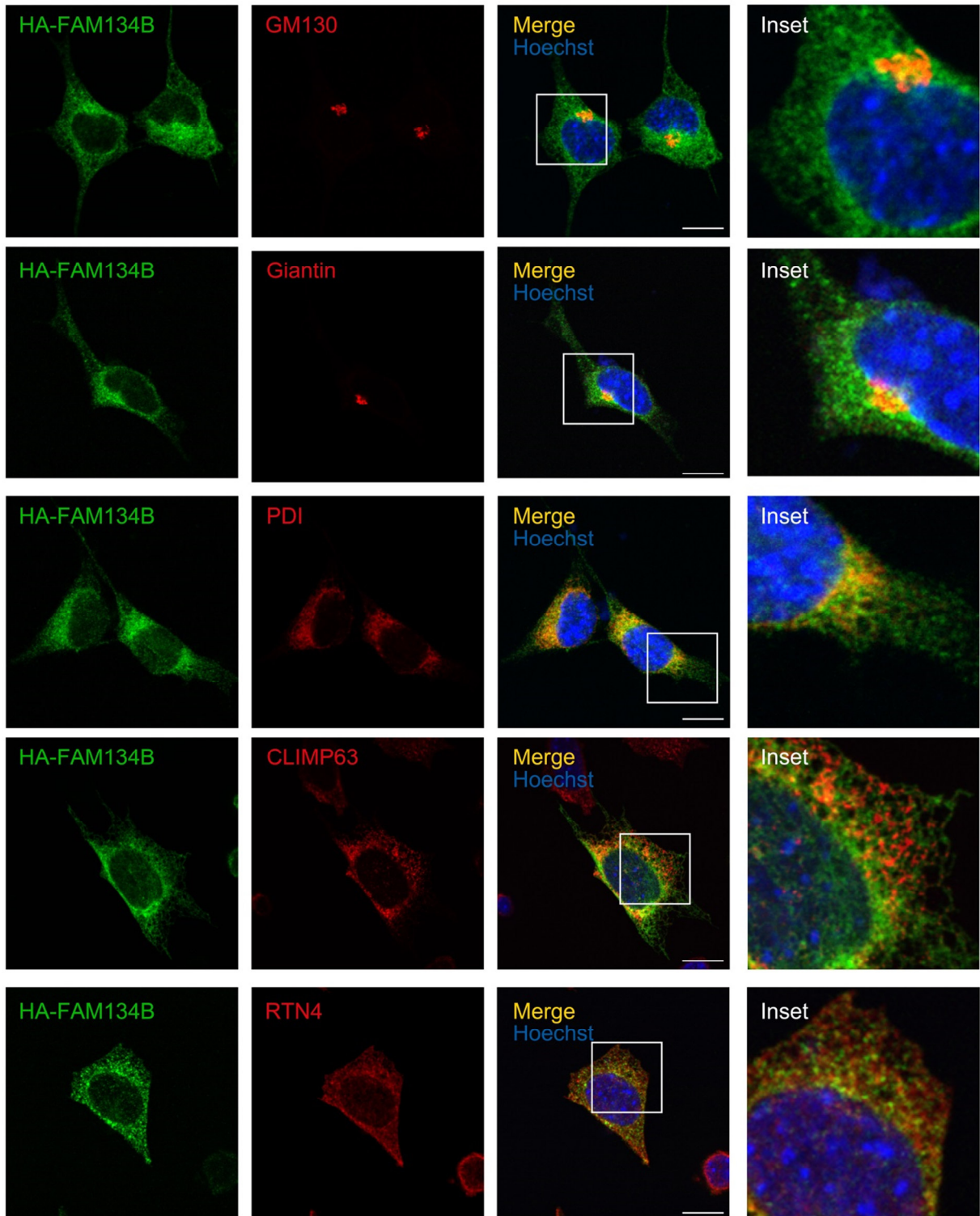


Figure 16: Subcellular distribution of immunofluorescent HA-tagged FAM134B

Confocal images of MEF cells transiently expressing HA-FAM134B. 48 h post-transfection, cells were fixed and co-stained for HA and established subcellular compartment marker proteins (red channel). Images were taken with a confocal laser scanning microscope (Leica TCS SP5) equipped with a 63x objective. The left column shows HA-FAM134B by anti-HA immunostaining. In the second column the distribution of the following marker proteins are illustrated: Giantin and GM130, specific for the cis-Golgi apparatus, PDI as ER luminal marker, Climp63 as ER sheet marker and Rtn4 as marker for tubular ER structures. In the third column the merged images are shown (Scale bars: 10 μ m). Nuclei were stained with Hoechst 33258. Co-staining is illustrated by the yellow color in overlay images. The white box indicates the enlarged area displayed in the last column.

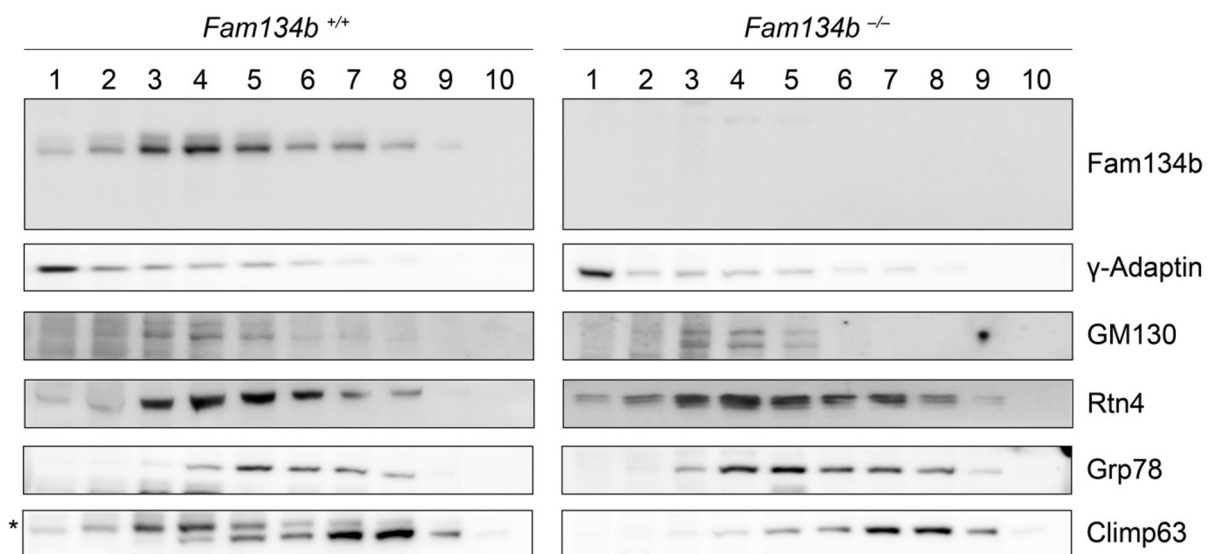


Figure 17: Subcellular fractionation studies of the ER and Golgi compartment

The localization of Fam134b was analyzed in mouse neuronal tissue by density gradient ultracentrifugation. The ER and Golgi compartments were fractionated on a discontinuous iodixanol gradient (2.5 to 30%). Proteins of the collected fractions were separated by SDS-PAGE, transferred onto a PVDF membrane and incubated with antibodies specific for proteins that are markers of distinct ER and Golgi sub-compartments. In parallel, the same experiment was performed using tissue from knockout (*Fam134b*^{-/-}) mice to verify the specificity of the Fam134b-related signal detected in wild-type (*Fam134b*^{+/+}) samples. The asterisk (*) labels the Fam134b-specific protein band derived from previous detection prior to Climp63 antibody incubation.

In order to support the initial findings from the overexpression studies in mouse fibroblast cells, a second method analyzing ER and Golgi apparatus-positive subcellular fractions was used. For this purpose, a subcellular fractionation study to isolate ER and Golgi apparatus gradient fractions prepared from mouse neuronal tissue was performed and followed by immunoblot analyses for endogenous Fam134b (see Figure 17). Each fraction of the entire density gradient was analyzed for subcellular marker proteins for the organelles of interest. The gradient fraction of the lowest density was observed to be strongly positive for γ-Adaptin that labels clathrin-coated vesicles of the late-Golgi apparatus, trans-Golgi network (TGN) and the endosome secretory pathway (Robinson 1990, Gu et al. 2001). The ‘Golgi matrix protein of 130 kDa’ termed as GM130 was predominantly detected in fractions three, four and five. However, the ER-resident proteins were spread across several fractions probably due to the larger variation in the density of ER-derived structures. Thus, Reticulon-4 (Rtn4) as tubular ER structural protein also localized to the Golgi apparatus-positive fractions but extended to higher densities. Next, Grp78 (the ‘78 kDa glucose-regulated protein’ also known as BiP/‘Binding immunoglobulin protein’), an ER chaperone protein (Munro and Pelham

1986), was observed to be slightly density-shifted with the most intense immunoreactivity in fraction number five. At last, Climp63-positive fractions were observed in the bottom layers of the gradient consistent with previous reports (Puhka et al. 2012, Zhang et al. 2014) and, thus, were largely separated from the Golgi apparatus enriched membranes. The applied iodixanol gradient successfully separated the compartments of interest. Immunodetection of endogenous Fam134b protein revealed its presence in both Golgi- and ER-positive fractions and distributed among the gradient in a pattern very similar to Rtn4. The specificity of the detected Fam134b protein band was verified by its absence in fractions prepared from knockout mice (for immunoblots with *Fam134b* wild-type and knockout samples run on one gel see Appendix Figure 29). The distribution of the applied subcellular marker proteins among the gradient was, with the exception of Grp78, not altered in neuronal tissues from *Fam134b* knockout mice compared to wild-type mice. Grp78 levels seemed to be increased in samples from knockout mice which might indicate activation of ER stress signaling (Lee 2005). In conclusion, from microscopy studies with overexpressed HA-tagged FAM134B and the subcellular fractionation by density gradient centrifugation supported Fam134b's localization to ER and Golgi structures. Notably, immunoblotting of fractionation samples detected the endogenous Fam134b and was performed with mouse brain tissue lysates.

5.2.2 Investigation of protein-protein interactions

Based on the assumption that protein-protein interactions might play a key role in predicting the respective protein function, tests for potential interaction partners of Fam134b were performed. In a previous data set from our lab, FAM134B was used as bait for a yeast two-hybrid (Y2H) screening with a human testis library. From this study, members of the LC3-like modifier proteins were identified as potential interaction partners. Hence, co-immunoprecipitation (co-IP) experiments were performed to examine whether FAM134B interacts with endogenous 'Microtubule-associated protein light chain 3' (LC3) *in vivo*. Addressing this issue, cells were transfected with different versions of tagged FAM134B and immunoprecipitated from HEK293T cell lysates followed by immunodetection of endogenous LC3. As depicted in Figure 18, whole cell lysate input samples showed protein bands corresponding to the cytosolic LC3-I and a faster running processed and lipidated LC3-II that is present at autophagosomal membranes (Barth et al. 2010). Half of the cells were treated with Chloroquine that increases the number of autophagosomes and prevents their proper degradation (Boya et al. 2005). Accordingly, treated cells compared to untreated cells showed

a strong induction of LC3II in the respective input samples. Interestingly, the presence of the LC3-specific band of ~14 kDa in IP samples confirmed the co-purification of endogenous LC3 with FAM134B-myc (see Figure 18). The most striking observation from this data is the specificity for the membrane-bound version, LC3-II, but not for LC3-I. Importantly, the truncated FAM134B version ‘S309X’, previously identified in human patients as disease-causing did not interact with LC3II. FAM134B-S309X-myc lacks large parts of the C-terminal end of the wild-type protein, hence, is detected as faster migrating band in input and IP samples after Western blotting. As a negative control, untransfected cells were used to rule out false-positive results due to an unspecific association of proteins with the antibody-conjugated beads used.

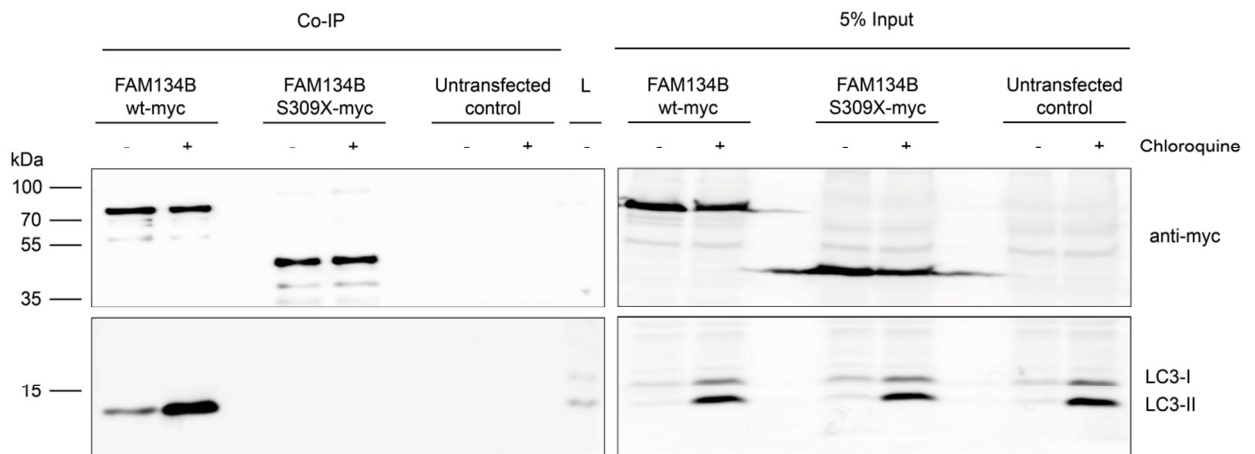


Figure 18: FAM134B-LC3 protein interaction studies by co-immunoprecipitation

Co-immunoprecipitation (Co-IP) of FAM134B-myc in lysates of HEK293T cells transiently transfected with the FAM134B wild-type construct (denoted as FAM134B wt-myc) or the truncated mutant version ‘S309X’ (denoted as FAM134B S309X-myc). 36 h after transfection, cells were treated with 50 μ M Chloroquine (O/N) to induce lipidated LC3 bound to autophagosomal membranes. LC3-II is detected by a higher electrophoretic mobility compared to cytosolic LC3-I in SDS-PAGE. Prior to incubation of cell lysates with myc-antibody-coupled beads, an input sample was taken and stored at -20°C . As a negative control, lysates of untransfected cells underwent immunoprecipitation in parallel. One sample of cell lysate (denoted as L) was run together on the gel with co-IP samples to detect both LC3-I and LC3-II at this membrane. Probing of the membranes with the myc-specific antibody detected full-length wild-type FAM134B-myc and truncated FAM134B S309X-myc mutant protein in the respective cell lysates both in input and IP samples.

Because of the revealed interaction of FAM134B with LC3-II, we tested whether FAM134B harbours a ‘LC3-interaction-region’ (LIR) motif (see chapter 3.4.3). Briefly, a LIR motif is characterized by the core consensus amino acid sequence [W/F/Y]xx[L/IV] and has been reported to mediate the interaction with LC3-like modifiers in various proteins (Birgisdottir et al. 2013). In fact, the protein sequence alignment depicted in Figure 19 identified such a putative sequence, which was highly conserved in different species. The identified motif

[D/E]DFELL is present close to the C-terminal end in all FAM134 family members. The functional relevance of this putative LIR for FAM134B's protein interactions was strengthened by the co-immunoprecipitation data presented in Figure 18. It was demonstrated that the truncated FAM134B protein 'S309X' lacking the proteins C-terminus which harbours the hypothesized LIR motif, was unable to co-immunoprecipitate LC3-II.

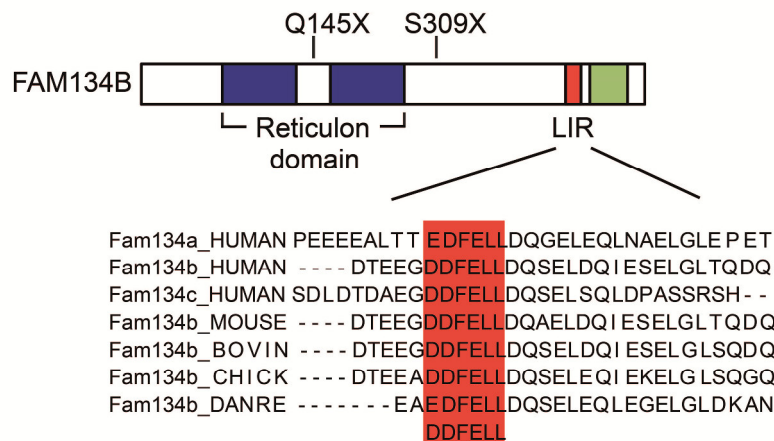


Figure 19: Multisequence alignment of the LIR motif present in Fam134 proteins

The upper scheme shows the predicted domain architecture of Fam134b containing two large hydrophobic segments interrupted by a short hydrophilic loop known as reticulon domain (highlighted in blue), a putative LIR motif (red) was identified next to a C-terminal coiled-coil domain (marked in green). Sites of the truncating disease-causing mutants reported in human patients are depicted on top of the scheme. Below, the alignment of amino acid sequences shows that the putative LIR sequence DDFELL is highly conserved during evolution (shown for human, mouse, bovine, chicken and zebrafish (*Danio rerio*) and among the members of the Fam134 protein family.

In order to verify the functional role of the LIR motif for the identified protein-protein interaction, cells transiently expressing HA-tagged FAM134B and GFP-LC3 were examined. HA-tagged FAM134B expression construct encoding a mutant version with the amino acids DDFELL (= LIR motif) substituted by alanines was transfected. MEF cells were incubated with EBSS for 6 hours to trigger the starvation-induced formation of autophagosomes, which was visualized by GFP-LC3 immunofluorescence. The wild-type HA-FAM134B was targeted to vesicle-like structures that perfectly merged with GFP-LC3, whereas the mutant LIR-version did not show such a punctate fluorescence pattern. This data provides strong evidence for the interaction of FAM134B with lipidated LC3 present at autophagosomal membranes. Since starvation-induced targeting of overexpressed HA-FAM134B into LC3-positive compartments was fully abolished by alanine-substitution of the six core amino acids identified as putative LC3-interacting region, its functional importance mediating FAM134B-

LC3-II interaction was proven. Taken together, both co-immunostaining and -precipitation confirmed the interaction of LC3 with Fam134B that was suggested by Y2H-screening. This interaction is mediated by the conserved DDFEEL amino acid sequence. However, interaction with other members of LC3-like modifier proteins was not further addressed within this thesis.

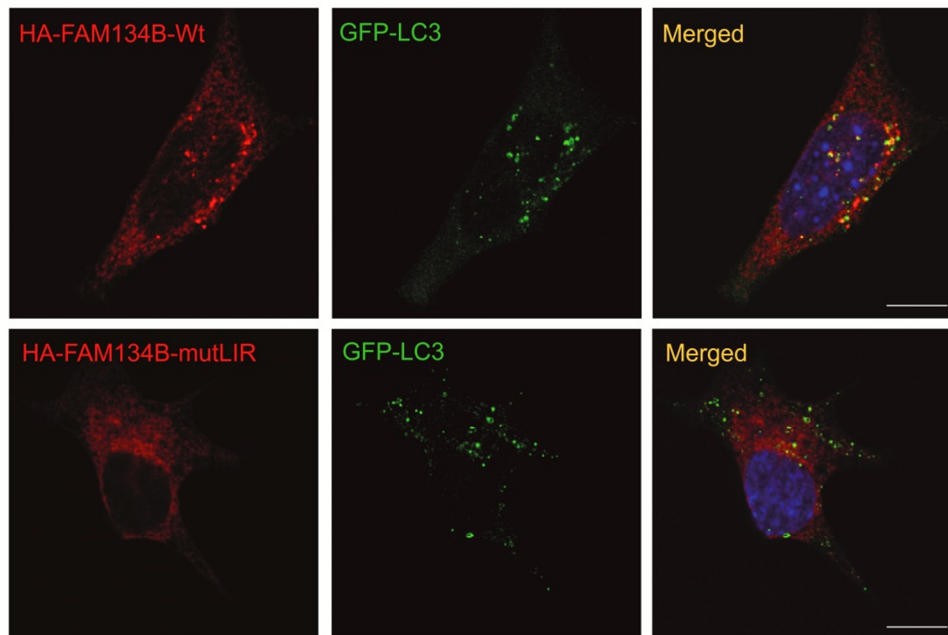


Figure 20: Co-localization studies of FAM134B and autophagosomes

Confocal images of MEF cells transiently co-transfected with plasmids encoding GFP-LC3 and either HA-FAM134B or a HA-FAM134BmutLIR variant are shown. 24 h post-transfection, cells were EBSS-starved for 6 h, fixed with 4% PFA and stained with anti-HA and anti-GFP antibodies. Images were taken with a confocal laser scanning microscope (Leica TCS SP5) equipped with a 63x objective. The left column shows the pattern of overexpressed HA-Fam134b-wild-type or -mutLIR as indicated. In the middle column GFP-LC3 fluorescence pattern is shown. In the third column merged images are displayed (Scale bars: 10 μ m). Nuclei were stained with Hoechst 33258. Costaining is illustrated by the yellow color in overlay images.

5.2.3 Analysis of the Fam134b membrane topology

The ER and Golgi compartment localization of Fam134b (see chapter 5.2.1) and the predicted Fam134b functional domains (Figure 19) together with the newly identified and experimentally verified LIR motif led to the question whether the C-terminal end of Fam134b localizes to the cytoplasm. To determine the Fam134b membrane topology, a fluorescence protein protection (FPP) assay was performed by live-cell imaging. In principle, the initial treatment with digitonin permeabilizes the plasma membrane of cells selectively, but leaves intracellular membranes intact due to differential cholesterol concentrations. The subsequent incubation with trypsin degrades the fluorescent protein tags of membrane proteins facing the cytosolic

compartment, whereas tags facing the lumen of intracellular compartments are protected and thus remain fluorescent (Lorenz et al. 2006). The results of these experiments are summarized in Figure 21.

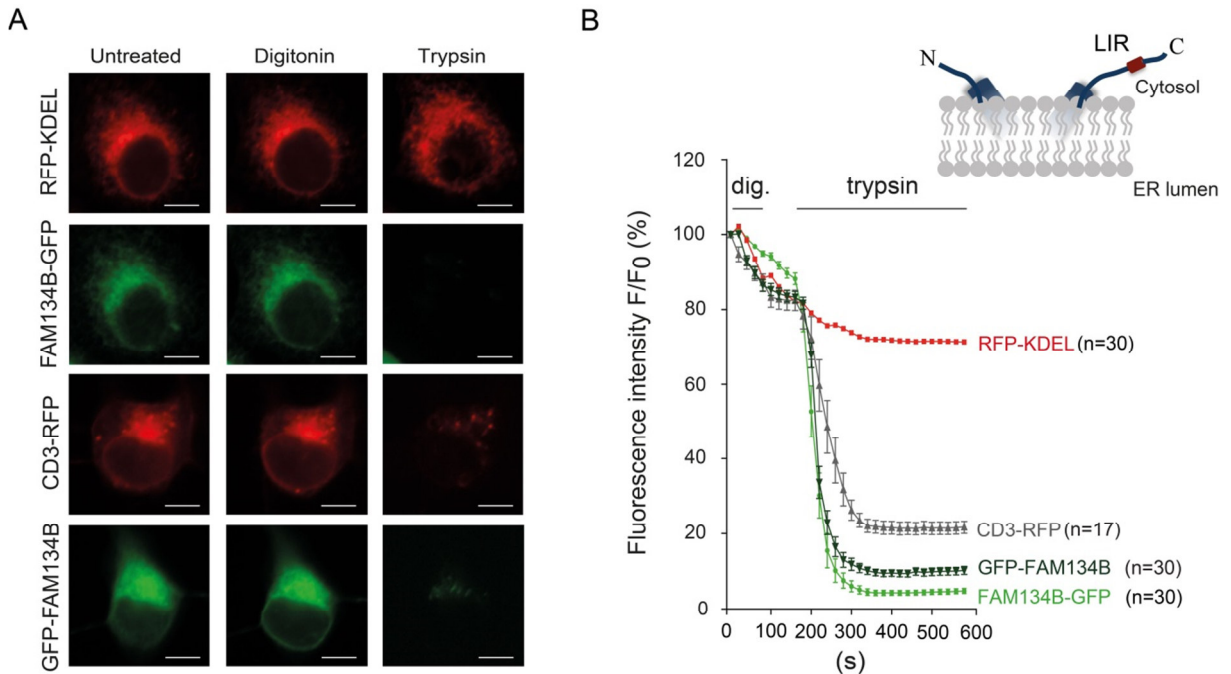


Figure 21: FAM134B topology studies by assaying fluorescence protein protection

(A) Fluorescence microscopy images of COS-7 cells transiently transfected with the constructs indicated. C- and N-terminally tagged FAM134B, CD3-RFP and RFP-KDEL were subjected to fluorescence protein protection (FPP) assay. Images shown were taken before treatment (left column), after incubation with 18 μ M digitonin for 80 seconds (middle column) and after subsequent incubation with trypsin (last column) using an inverted Axio Observer Z.1 microscope (Zeiss) equipped with AxioCam MRm and a 20x objective (Scale bars: 10 μ m). (B) Images were recorded every 20 s for 10 min and quantification of mean fluorescence intensities of single cells were calculated by ImageJ software. Fluorescence values were subtracted from the background fluorescence and normalized to the mean fluorescence value of each cell (F) at the starting time point of the experiment (F_0). A strong decrease in relative fluorescence (F/F_0) was observed for CD3-RFP, GFP-FAM134B and FAM134B-GFP after digitonin and subsequent trypsin treatment, but not for RFP-KDEL (n =number of analyzed cells). The inset shows the confirmed topology with both the N- and C-terminal end facing the cytoplasm.

The illustrated microscopy images and the quantification of the relative fluorescence intensities summarized in Figure 21B clearly show that the fluorescence of the luminal ER peptide RFP-KDEL remains largely unaffected from trypsin treatment. In contrast, the C-terminally RFP-tagged CD3 (CD3-RFP) served as positive control due to its known topology with the RFP-tag exposed to the cytoplasmic site and accordingly RFP-fluorescence was not protected. Similarly, both a C- and N-terminal tagged FAM134B protein underwent the FPP assay. The applied trypsin accessed the respective GFP-tags as concluded from the strong decrease in relative fluorescence values. In conclusion, both the C- and N-terminal end of FAM134B face towards the cytoplasm and thus are accessible to various cytosolic proteins.

Particularly, the revealed interaction of FAM134B with LC3 via the functional LIR motif (see chapter 5.2.2) is feasible.

5.2.4 Membrane shaping function of FAM134B

FAM134B contains a characteristic protein domain highly similar to reticulon proteins that mediate membrane bending as introduced in section 3.2.2. To test for an *in vitro* membrane shaping function of FAM134B, a liposome shaping assay was performed by Dr. N. Koch of the Biochemistry department of Jena University Hospital. For this purpose, recombinant GST-FAM134B fusion protein was incubated with liposomes and resulted in a reduced liposome size as illustrated by TEM images of freeze-fractured liposomes (see Figure 22). Similarly, the S309X mutant version of FAM134B, lacking the C-terminal hydrophilic region, leads to a pronounced increase in the relative numbers of smaller structures in comparison to control liposomes pre-incubated with GST. In contrast, the more severely truncated Q145X mutant version, additionally lacking parts of the reticulon-domain, did not affect liposome size. In conclusion, FAM134B showed *in vitro* membrane shaping that is abolished in case of FAM134B-Q145X where the truncating mutation involves parts of the reticulon domain.

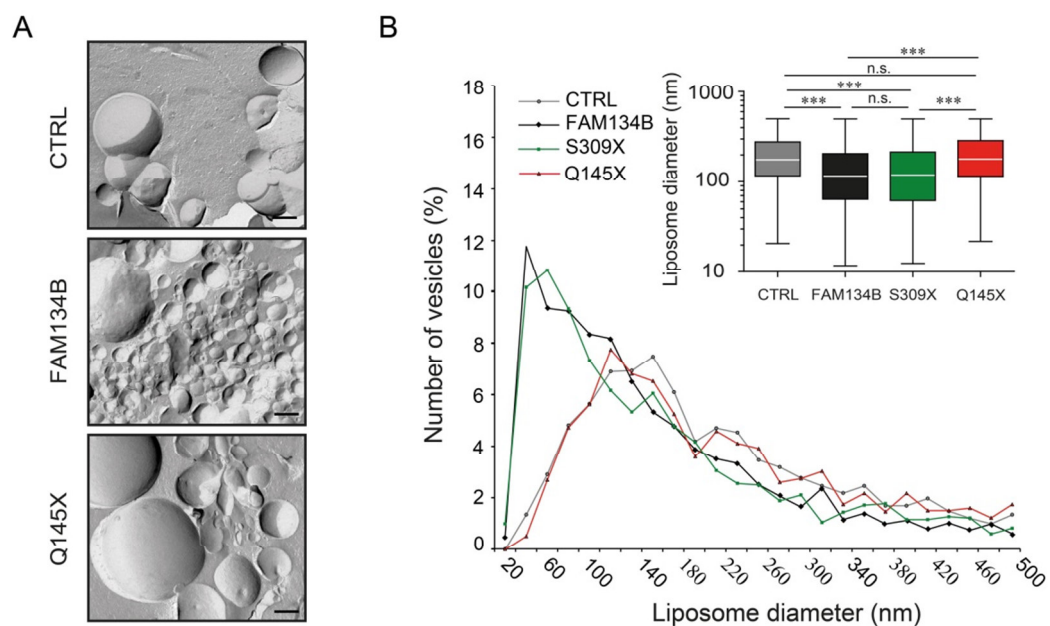


Figure 22: *In vitro* liposome shaping assay

(A) Transmission electron microscopy (TEM) images of freeze-fractured incubations of liposomes with recombinant GST-fusion proteins (GST-FAM134B, GST-FAM134B-Q145X, CTRL=GST) are depicted in the left column (Scale bars: 200 nm). (B) The diagram shows the distribution of liposome diameters observed by TEM of freeze-fractured liposomes. Inset: Box plots of presented data. Y-axis is logarithmic (n=2682 for CTRL, n=2683 for FAM134B, n=1685 for Q145X, n=1612 for S309X). Boxes contain 50% of the values; minimal, maximal and median values are marked by vertical lines. Statistical test: one-way ANOVA (n=number of liposomes). Results are expressed as mean \pm SEM.

5.3 Functional studies of autophagy in *Fam134b* knockout tissue and cells

At last, the functional importance of the *Fam134b*-LC3-interaction for the *Fam134b* knockout mouse model was assessed in respect to potential mechanisms underlying the organellar changes evident from ultrastructural studies of sensory neurons. To explore autophagy in *Fam134b* wild-type and knockout mice, protein expression analysis of autophagy-relevant marker proteins (see chapter 3.4) on DRG whole tissue extracts were performed. Beclin-1 is a well-known key-component for the initiation of autophagosomal structures and decreased levels of Beclin-1 have been already reported to be associated with neurological disorders based on neuronal autophagic dysfunction (Pickford et al. 2008). In addition, autophagy-mediated degradation of p62 is an established tool for autophagic studies simply by assaying p62 protein levels that, if accumulated, may indicate defects in autophagosomal clearance (Bjørkøy et al. 2009). As summarized in Figure 23, the protein levels of Beclin-1 and p62 were comparable between *Fam134b* wild-type and knockout mice at the respective ages in DRG sensory neuron lysates. However, considering protein expression changes during life, both autophagosomal marker proteins were apparently upregulated in 10-month-old mice compared to 2.5-month-old mice, but this age-related effect was observed in the same extent in *Fam134b* wild-type and knockout mice.

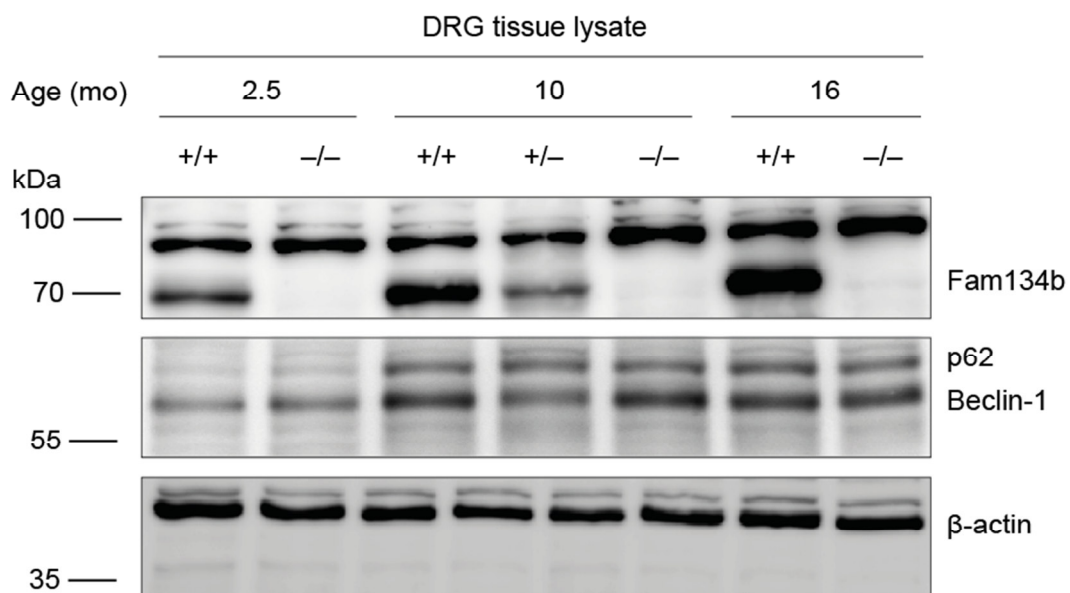


Figure 23: Protein expression studies in mouse neuronal tissue

Protein expression levels were examined in lysates of DRGs isolated from *Fam134b* wild-type (+/+), heterozygous (+/-) and knockout (-/-) mice at the ages indicated. Whole tissue extracts were subjected to SDS-PAGE (15% gel) and processed for immunoblot analysis with antibodies specific for *Fam134b*, p62 and Beclin-1. Immunodetection of β -Actin served as loading control.

Moreover, a comprehensive study of autophagy protein levels includes immunohistochemical analysis assuming that proteins isolated from whole tissue homogenates might seem normal regardless of effects on small subsets of DRG neuron populations. For this purpose, available antibodies were pre-tested for specificity and sufficient sensitivity on cryosections of sensory neuronal tissue. P62-stained tissue sections are illustrated in Figure 24. The clearly detectable fluorescent p62-puncta indicated the presence of autophagosomes. DRG-tissue distribution of detected p62-puncta was restricted to the cytosolic surface of sectioned neurons and further indicating high specificity of the staining. Quantification of p62-positive vesicular structures revealed no significant difference in p62-protein expression pattern at single cell level.

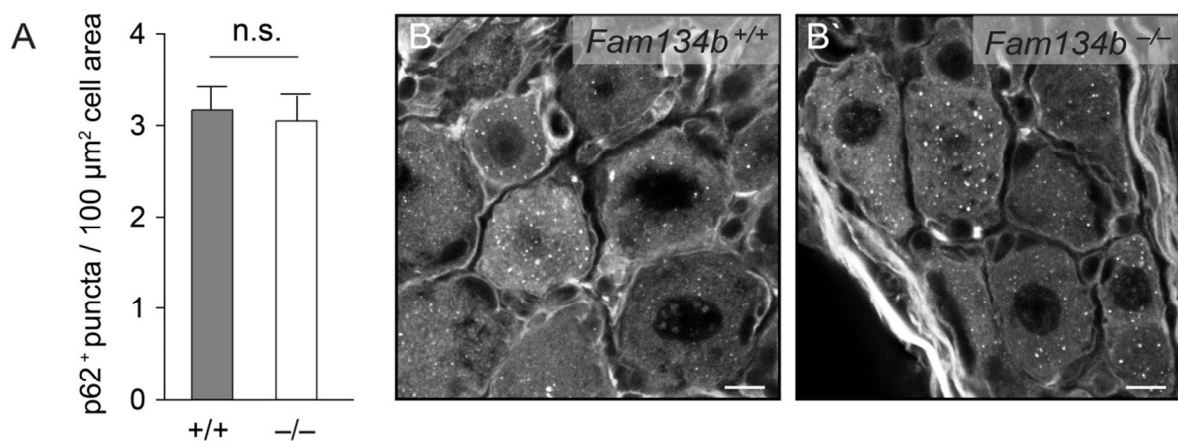


Figure 24: p62-protein expression monitored in DRG cryosections

(A) Quantification of p62-positive puncta in somata of large sensory DRG neurons prepared from 11-month-old wild-type (*Fam134b*^{+/+}) and knockout (*Fam134b*^{-/-}) mice (n=40 cells from 2 animals per genotype). 10-μm DRG L4-cryosections were stained with the p62-antibody. Representative images are shown in (B) and (B') and were acquired using a confocal laser scanning microscope (Leica) equipped with a 40x objective. For quantification of p62-positive puncta the ImageJ software was used. P62-positive regions of interest were set and quantified per cell. The numbers of p62-positive puncta were normalized to the size of the analyzed cells (Scale bars: 10 μm). Statistical test: Student's *t*-test.

To additionally test for differences in the autophagic flux with another frequently applied autophagy marker, LC3 protein levels were studied. Autophagosome formation is correlated with the conversion of cytosolic LC3-I into autophagosomal membrane-bound LC3-II, which is detected by a slightly higher electrophoretic mobility in SDS-PAGE followed by Western blotting (Barth et al. 2010). Based on the findings from *Fam134b*-protein interaction studies in chapter 5.2.2 identifying LC3-II as interaction partner, it seemed even more relevant to test for LC3-I and LC3-II protein levels in *Fam134b* knockout mouse neuronal tissue.

Figure 25 shows that levels of LC3-II from DRG tissue protein lysates were hardly detectable at any age of the analyzed mice. Additionally, brain tissue lysates from 10-week-old mice were analyzed and exhibited very low, but slightly higher LC3-II levels compared to DRG sensory neuron tissue. In contrast, LC3-I protein was highly expressed both in brain and DRG tissue lysates but did not show differences among genotypes.

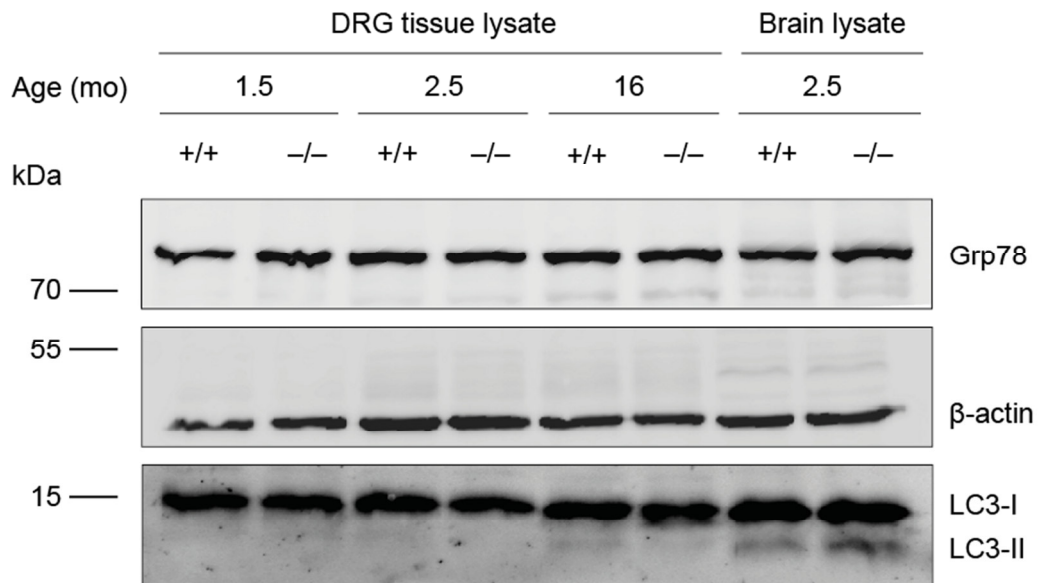


Figure 25: Protein expression of LC3 and Grp78 in mouse neuronal tissue

Protein expression levels of LC3 and Grp78 in lysates of DRG and brain tissue from *Fam134b* wild-type (+/+) and knockout (-/-) mice at ages in months (mo) indicated. Protein samples were subjected to SDS-PAGE (15% gel) and processed for immunoblot analysis with antibodies specific for Grp78 and LC3B. Immunodetection of β -Actin served as loading control.

In avoidance of misinterpretation, an additional gel was run with lysates obtained from HEK293T and starved MEF cells as positive control for LC3-II protein detection. The detection of LC3 by Western Blotting is illustrated in Appendix Figure 30 and confirmed the absence of LC3-II expression in DRG tissue lysates in contrast to lysates obtained from HEK293T and starved MEF cells. Thus, the possibility of technical difficulties to detect LC3-II in murine cell lysates was ruled out. In conclusion, the number of autophagosomes seems particular low in mouse neuronal tissue. These findings are consistent with reports comparing LC3-I-to-II conversion in multiple tissues, with almost no LC3-II band detectable in the mouse brain (Mizushima et al. 2004). However, it is assumed that the underlying reason may be a highly efficient autophagosomal clearance rather than less autophagic activity in neurons (Boland et al. 2008).

Furthermore, data obtained from the immunodetection of Grp78 is shown in Figure 25. An elevated Grp78 level might be indicative for ER stress responses and was observed to be differentially expressed in mouse brain subcellular fractionations (see Figure 17). For this reason, Grp78 protein expression was examined in neuronal tissue, but protein levels in *Fam134b* knockout mice were not different. However, limitations of tissue lysate analyses by Western blotting might mask differences present in small subpopulations of neurons only. Nonetheless, the p62-protein expression pattern investigated in single sensory neurons from DRG tissue sections was found unchanged between *Fam134b* wild-type and knockout mice at 11 months of age. In conclusion, no general alterations in bulk autophagy pathways were evident.

A more profound study of the time-course of autophagic activity required the specific stimulation of cells and distinct time-series experiments that were not feasible by analysis of mouse tissue. Hence, immortalized fibroblasts were prepared from embryonic *Fam134b* wild-type and knockout mice and studied to monitor autophagy pathway dynamics.

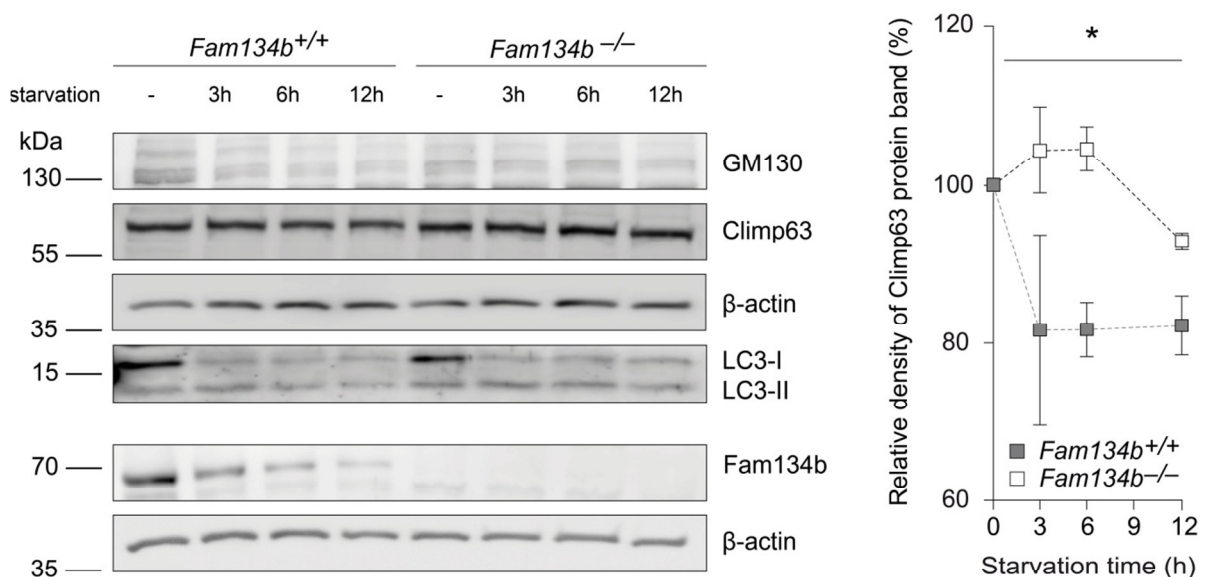


Figure 26: Protein expression of Fam134b, GM130, Climp63 and LC3 in MEFs

(A) Endogenous Fam134b, Climp63 and LC3 expression levels were analyzed in lysates of mouse embryonic fibroblasts (MEFs) derived from wild-type (*Fam134b*^{+/+}) and knockout (*Fam134b*^{-/-}) mice. Immortalized MEFs were either EBSS-starved for the time as indicated (in hours) or left untreated (-). Then, cells were lysed and subjected to SDS-PAGE (15% gel) and processed for immunoblot analysis with Fam134b, GM130, Climp63 and LC3B antibody. Immunodetection of β -Actin served as loading control. (B) Quantitative analysis of Climp63 protein bands by densitometry by the use of ImageJ software. Statistical test: two-way ANOVA.

MEFs of both genotypes underwent EBSS-starvation for different time duration or were left untreated as indicated in Figure 26. Then, protein expression levels were analyzed in the respective protein cell lysates. The autophagic flux was determined by investigation of LC3-I and LC3-II protein bands which were observed to be identical in *Fam134b* wild-type compared to *Fam134b* knockout cells. Thus, it can be concluded that Fam134b does not appear crucial for non-selective bulk autophagy function.

Impressively, starvation strongly triggered Fam134b protein degradation. Even after 3 h of EBSS-starvation, only 46% of Fam134b was detected compared to untreated cells. The decrease of Fam134b protein correlated with the time of starvation and after 12 h of starvation Fam134b was barely detectable. To elucidate whether the extent of Fam134b protein degradation might be due to a general breakdown of the compartments, where Fam134b resides, the rough ER structural protein marker Climp63 and the Golgi matrix protein of 130 kDa (GM130) were analyzed. GM130 protein was hardly detectable and was found less abundant in MEF cell lysates for a conclusive interpretation. In contrast, the Climp63 protein level was applicable for detailed quantitative densitometric analysis and showed a significant reduction upon starvation (Figure 26B). Interestingly, this mild starvation-induced Climp63 breakdown was abolished in MEFs deficient for *Fam134b*.

Based on the observation that the starvation-mediated reduction of an ER compartment marker is dependent on Fam134b, the ER structure was analyzed in single cell immunofluorescence studies. MEF cells were transiently co-transfected with plasmids encoding for GFP-LC3, HA-FAM134B wild-type and a FAM134B-mutant LIR protein. Starvation-induced autophagosomes were present and co-labeled with HA-FAM134B wild-type but not FAM134BmutLIR consistent to initial findings illustrated in Figure 20. The tubular ER-marker Reticulon 4 (Rtn4) was found as punctated pattern at endogenous level in transfected cells and might be indicative for small ER fragments. Those fragments were found positive for both HA-FAM134B and GFP-LC3. In contrast, cells expressing the mutLIR version of HA-FAM134B did not show such Rtn4-positive fragments. Hence, it was hypothesized that FAM134B-mediated sequestration of ER fragments into autophagosomes might be dependent on its functional LIR domain.

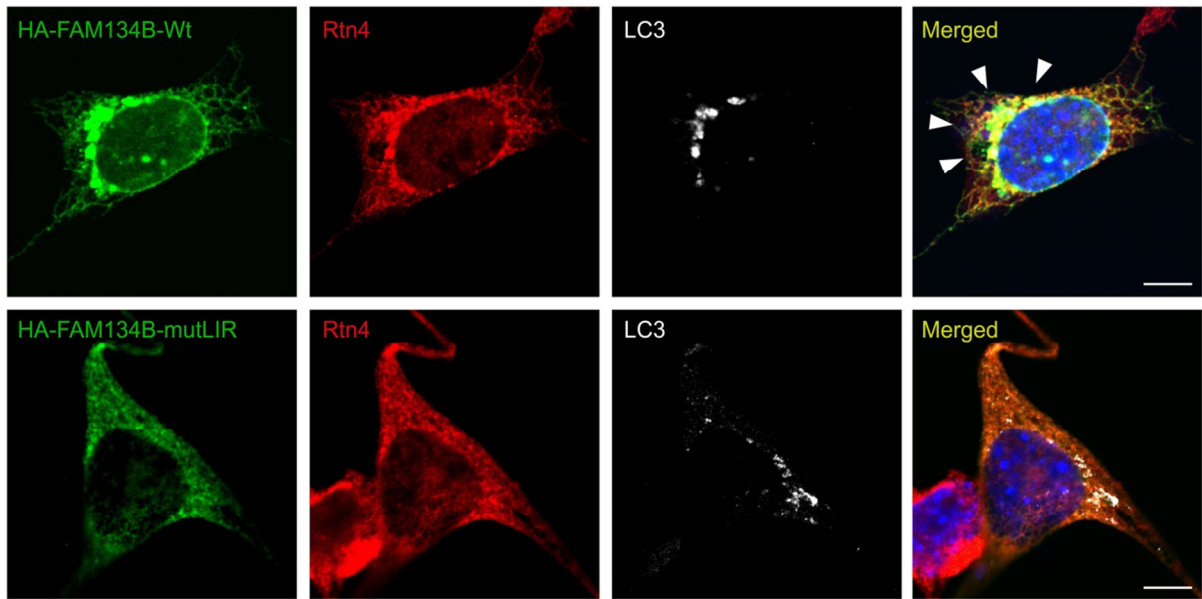


Figure 27: Protein co-localization studies of FAM134B, Rtn4 and autophagosomes

Confocal images of MEFs transiently co-transfected with plasmids encoding GFP-LC3 and either the HA-FAM134B or a HA-FAM134BmutLIR variant are shown. 24 h post-transfection, cells were EBSS-starved for 6 h, fixed with 4% PFA and stained with anti-HA, anti-Rtn4 and anti-GFP antibodies. Secondary antibodies conjugated to Cy5 (for HA-FAM134B detection), Alexa-488 (for GFP-LC3-detection) and Alexa-546 (for Rtn4 detection) were applied. Single-color stained controls were used to ensure that each dye was only detected in one single channel. Images were performed using a confocal laser scanning microscope (Leica TCS SP5) equipped with a 63x objective. The left column illustrates the pattern of overexpressed HA-FAM134B-wild-type or -mutLIR as indicated. In the second column endogenous expression pattern of the tubular ER compartment marker Rtn4 is shown. The third column shows fluorescence pattern of GFP-LC3 visualized in greyscale. In the last column merged images are presented. Puncta positive for all fluorescence channels are indicated by arrowheads. Nuclei were stained with Hoechst 33258 (Scale bars: 7.5 μm).

6 Discussion

This thesis attempted to uncover the function of FAM134B to elucidate the pathophysiology of HSAN2B, an inherited progressive sensory neuropathy. Disruption of *Fam134b* in mice mimicked key characteristics of the human disease. The molecular mechanisms underlying *Fam134b*-mediated neuropathy were addressed by a combinatorial approach including mouse phenotyping, protein biochemistry and cell biology.

6.1 *Fam134b* knockout mice develop a progressive sensory neuropathy

The initial assessment of *Fam134b* knockout mice did not show any obvious abnormalities in respect to Mendelian birth ratio, behaviour, lesions or a shortened life-span. Because of the clinical relevance of *Fam134b* for the development of HSAN2 (see chapter 3.2.1), a detailed analyses of the peripheral nervous system (PNS) was performed. First of all, behavioural tests for nociception were conducted to validate whether our knockout mouse model phenocopies human disease characteristics. Initially, several different methods of rodent analgesiometry (Mulder and Pritchett 2004) were pre-tested. Most tests for nociception were limited by a low sensitivity and a high degree of inter-individual variation. Only the water-immersion tail-flick assay proved to be suitable. This test measures a spinally mediated response to an acute thermal pain stimulus with an intensity set by the water temperature. The tail-flick latencies in response to thermal nociceptive stimuli were found to be increased in two-year-old mice deficient for *Fam134b* compared to wild-type littermates and thus provided first evidence for impaired sensitivity to thermal pain. In six to eight months old mice such an effect was not observed. These initial findings proposed a progressive sensory dysfunction of small-caliber nociceptive fibers in *Fam134b* knockout mice. The late-onset sensory neuropathy in *Fam134b* knockout mice was confirmed by nerve conduction studies. For this approach, supramaximal stimuli were delivered to the nerves of the tail predominantly activating large-caliber nerve fiber responses that were recorded at the tail base. We observed decreased sensory nerve conductance velocities (NCVs) and amplitudes in 12-, but not 6-month-old mice. In addition to the direct assessment of afferent fiber function, the degeneration of sensory nerve fibers was shown by histological analysis. The 7% reduction in afferent fiber number was observed in aged, but not young adult mice, which is consistent with findings from functional sensory nerve studies and thus proves the progressive nature of the sensory neuropathy in *Fam134b* knockout mice. The histological study of sensory nerve fiber quantification was technically

achieved by analyzing the cross-sectioned pre-ganglionic fiber bundles. A precise quantification of sensory fibers in more distal regions with the same high sensitivity was not feasible, but might have revealed a more pronounced axonal loss at peripheral sites. Similarly, in human HSAN2B patients initial distal axon degeneration spreads in a progressive manner to proximal parts of the neuron (Rotthier et al. 2012).

Compound muscle action potentials were unchanged in animals of the same age indicating that peripheral motor nerve function was unaffected in *Fam134b* knockout mice. Consistent with this finding, the morphology and number of alpha-motor neurons in spinal cord sections prepared from 2-year-old knockout animals was normal. In conclusion, the neurodegenerative phenotype seems restricted to peripheral sensory nerves in the mouse model analyzed. However, approaches to address autonomic dysfunction have not been applied. Clinical features of human patients suffering from HSAN2B occasionally involve mild motor neuron impairments or minor autonomic dysfunctions but effects on peripheral sensory neurons predominate (as introduced in chapter 3.2.1).

So the question remained how *Fam134b* loss selectively affects afferent neuron function. *Fam134b* protein expression is largely restricted to neuronal tissue and testis (Kurth et al. 2009), although it was found to be present at lower levels in embryonic fibroblast cells as well. So the *Fam134b*-related neurodegeneration appeared to be restricted to sensory axons despite *Fam134b*'s expression is not restricted to this specific subpopulation of neurons. In this regard, it might be important to ask whether the complementary expression of protein family members that probably possess redundant functions could account for this observation. The *Fam134* family is composed of three members, with *Fam134a* and *Fam134c* showing a broader gene expression pattern compared to *Fam134b* (Kurth et al. 2009). So far both of them are not linked to neurodegenerative disease but still similar functions may facilitate compensatory mechanisms. Further research should be undertaken to investigate the redundancy in gene function of other *Fam134* family members like e.g. the analysis of double and triple transgenic knockout mice. Overall, the mechanism underlying selective sensory neuron death in *Fam134b* knockout mice is not yet resolved.

Moreover, the impaired axon function may be specific for a particular subtype of sensory neurons. Previous *Fam134b*-knockdown studies in mouse primary DRG cultures supported the selective reduction of small soma diameter sensory neurons (Kurth et al. 2009). In contrast to this finding, human case reports of *Fam134b*-mediated HSAN2B demonstrated that both large and small myelinated fibers as well as unmyelinated fibers can be affected (Murphy et

al. 2012). Within the current study, the phenotypic characterization of *Fam134b* knockout mice revealed dysfunction of small unmyelinated C-fibers or myelinated small-caliber A δ -fibers by measuring tail flick latencies in response to a heat stimulus. Additionally, NCV studies showed that large myelinated nerve fibers were affected upon loss of *Fam134b*, which is in line with human case reports of HSAN2B.

However, in contrast to the human disease course, is the late onset of peripheral sensory dysfunction in our mouse model in relation to life span. Furthermore, the signs and symptoms present in *Fam134b* knockout mice are milder compared to affected humans. In HSAN2B patients, loss of sensory perception starts around the first decade of life and is strongly associated with severe injuries that have not been observed in the mouse model. The human HSAN2B clinically manifests as ‘dying back’ neuropathy (Hübner and Kurth 2014) which means that axonal degeneration starts at distal regions of the nerve fibers and progresses towards the nerve's cell bodies. Generally, in human longer sensory projections have to be maintained. This might explain why *Fam134b*-related axon length-dependent impairments have a milder manifestation in mice.

6.2 Changes in the architecture of the ER and Golgi apparatus

The *Fam134b* knockout mice model important features of a progressive sensory neuropathy as pointed out in the previous chapter. For this reason, these mice are well suited to study disease-causing mechanisms underlying HSAN2B.

Detailed histological analysis aimed to identify intracellular alterations that may account for sensory neuron dysfunction. Initially, sensory nerve tissue was analyzed by conventional light and fluorescence microscopy which did not reveal obvious alterations. However, the ultrastructure of DRG sensory neurons showed changes of the Golgi apparatus and the endoplasmic reticulum in tissues of 11-month-old *Fam134b* knockout mice and in primary sensory neuron cultures obtained from 3-month-old mice.

The Golgi cisternae and ER tubules appeared to be severely dilated which presented as less electron-dense regions. In contrast, the accumulation of debris would be featured by high electron-dense structures but have not been observed. The organellar changes did not seem to be restricted to particular subcompartments of the Golgi or ER. The Golgi stacks were partially preserved and not shortened or dispersed as reported for a variety of human degenerative diseases marked by cytoplasmic aggregates of mutant proteins (Gonatas et al. 2006). Ultrastructural Golgi apparatus changes similar to that observed in our mice have been

reported in cortical neurons of a transgenic mouse model for a neurodevelopmental disorder, the Angelman syndrome. In this study, it was shown that Golgi stacks appeared swollen which was associated with a marked reduction of the Golgi lumen acidification (Condon et al. 2013). Swollen Golgi cisternae accompanied by rough ER (RER) dilations were further reported for mice lacking SPCA1, the secretory pathway Ca^{2+} ATPase 1, implicated in a human skin disease. Though drastic changes in Golgi apparatus and RER membranes were detected, substantial organellar functions were found preserved and the alterations observed are discussed as a possible pro-survival secondary response (Okunade et al. 2007).

In this respect, it is interesting to note that ultrastructural changes were already revealed at a pre-symptomatic state in primary neurons isolated from 3-month-old *Fam134b* knockout mice. This may suggest that the alterations of the ER and Golgi apparatus are an early event in the neurodegenerative disease course. Nevertheless it is important to keep in mind that a potential bias may arise from cell cultures. Primary isolated cells undergo considerable stress potentially triggering multiple changes in gene expression or metabolic activity and may promote early alterations of the ER and Golgi apparatus.

The organellar changes were only present in some of the sensory neurons and not in motor neurons or sensory neurites. It was not feasible to define the affected sensory neuron subtype since the ER and Golgi apparatus alterations were only detected by ultrastructural analyses. Advanced imaging approaches such as correlative light and electron microscopy would provide the possibility of identifying affected subtypes of sensory neurons in mouse neuronal tissue by fluorescent labeling and high resolution electron microscopy at the same time.

Overall, our findings allow two interpretations for the *Fam134b*-mediated progressive neurodegenerative phenotype observed in transgenic knockout mice: either the ER and Golgi apparatus organellar changes can be primary and directly contribute to functional impairments; or alternatively organellar changes are just secondary effects in stressed neurons. To address these options, *Fam134b* intracellular localization was studied.

Immunofluorescent staining of tagged FAM134B after transient overexpression and co-staining for several well described compartment marker proteins verified that *Fam134b* is present in the ER and Golgi compartment. Similarly, subcellular fractions of the ER and Golgi apparatus derived from neuronal tissue were analyzed and confirmed a rather homogenous distribution of the endogenous protein in both compartments. Taken together, it is suggested that *Fam134b* loss-of-function may rather disturb ER and Golgi compartment homeostasis directly and may lead to sensory impairments.

6.3 Functional domains of Fam134b

Several domains predicted from Fam134b protein's structure were indicative for its cellular functions (see chapter 3.2.2). The two characteristic hydrophobic reticulon-like domains may form a hairpin topology and thus mediate membrane shaping similar to reticulon and DP1/REEP/Yop1 proteins that induce ER tubule formation (see chapter 3.3.2). The predicted membrane shaping function was tested by an *in vitro* liposome shaping assay in collaboration with the Biochemistry department of Jena University Hospital. This assay revealed that liposome diameters decreased upon incubation with FAM134B. In contrast, this was not observed for mutant FAM134B-Q145X, where the reticulon domain is partially truncated. This observation implies that the full-length reticulon-like domain is required for membrane shaping. In conclusion, Fam134b possesses membrane shaping capacity in a reticulon-domain-like manner. Interestingly, a list of studies exists that link mutated membrane-shaping proteins with neurodegenerative diseases. Similar to FAM134B, ARL6IP1 (ADP-ribosylation factor-like 6 protein 1), Atlastins, REEP (receptor expression enhancing protein), SPAST and ZFYVE27/Protrudin have a predicted reticulon-like topology and are associated with axonopathies as reviewed in Hübner and Kurth (2014). Nevertheless, the molecular pathways inducing neuronal death in conditions of impaired membrane-shaping remain to be resolved. Apart from the reticulon domain, a C-terminal coiled-coil domain is predicted for Fam134b. Such structures often serve as homo-dimerization domains (Mason and Arndt 2004); however, its functional involvement was not further explored within this study.

Moreover, a conserved amino acid sequence was identified next to the C-terminal end of the FAM134B protein that is characteristic for a LC3-interacting region (LIR) consensus motif and provides a direct link to autophagy (introduced in chapter 3.4). The functionality of the LIR was confirmed by protein-interaction studies. Co-immunoprecipitation experiments verified the interaction of FAM134B with endogenously expressed LC3II, the lipid-conjugated form which is present at autophagosomal membrane structures. Importantly, this interaction was abolished by the disease-causing mutation S309X, which truncates a part of the C-terminal end of FAM134B including the LIR motif. Additional studies were performed at the Goethe University School of Medicine in Frankfurt (Prof. I. Dikic) to assess FAM134B protein interactions via GST-pulldown. A FAM134B-mutLIR protein was analyzed in which the core amino acids of the LIR (DDFELLD) were substituted by 7 alanine residues. No LC3-binding was detected in experiments testing FAM134B-mutLIR and verified the particular importance of these amino acids for the interaction with LC3 (Khaminets et al. 2015).

With respect to the functional LIR motif located next to the C-terminal end of FAM134B, the topology of FAM134B was examined. The topology is critical for the interaction of the LIR motif with cytoplasmic interaction partners, e.g. LC3-like modifiers. The performed fluorescent protein protection assay is based on the assumption that the fluorescent protein tags which face the lumen of intracellular organelles are protected from protease treatment after digitonin-mediated plasma membrane permeabilization. Fluorescent tags of integral membrane proteins that are exposed to the cytosol are digested. Similarly, the fluorescence of N- and C-terminally tagged FAM134B was not protected from protease treatment.

In summary, FAM134B localizes to the dynamically connected ER and Golgi endomembrane network. Due to its structural features, FAM134B probably inserts into the respective membranes as hairpin loop. Functional domains predicted from FAM134B's amino acid sequence gave evidence to assume membrane shaping function and LC3-binding, both of which were experimentally verified. Its C-terminally located LIR motif is exposed to the cytoplasmic site and thus allows interaction of FAM134B with LC3-like modifiers *in vivo*. In this context, the basis for the functional role of FAM134B in autophagic pathways is provided.

6.4 Fam134b is involved in selective autophagic pathways

As a final step it was asked if Fam134b has a crucial function in pathways of autophagy and if evidences of impaired autophagy are present in *Fam134b* knockout cells. Firstly, autophagic marker proteins were studied in murine tissues but did not differ between genotypes. Secondly, primary MEFs obtained from *Fam134b* transgenic mice were tested under basal conditions and upon starvation, but similarly revealed no differential expression levels of autophagosomal markers. These data led to the assumption that non-selective bulk-degradation is not affected by loss of *Fam134b*. There are reports from mice deficient for essential autophagy related genes (Atgs) exclusively in neural cells. In this context it had been shown that cytoplasmic inclusion bodies are present in neurons due to an impaired clearance from abnormal proteins leading to neurodegeneration. Interestingly, DRG sensory neurons were included in those studies (Taichi et al. 2006) and contained aggregates of ubiquitinated proteins. We have not observed similar aggregates in tissue sections of *Fam134b* knockout mice. Taken together, it was concluded that Fam134b does not play a pivotal role for basal and starvation-induced autophagy.

However, Fam134b itself was observed to be degraded massively under starvation and strongly co-localized with autophagosomes. Additionally, the protein expression level of the ER structural protein Climp63 was differentially regulated in wild-type *versus* knockout cells under starvation. In particular, Climp63 was found slightly degraded in wild-type, but not *Fam134b* knockout cells. In the collaborating laboratory of Prof. I. Dikic the ER compartment changes were intensively studied in a shRNA-mediated knockdown cell system. The resulting data revealed a proliferated ER compartment exclusively in cells treated with *FAM134B*-specific shRNA. The rescue of this effect was achieved by re-expressing *FAM134B* that reconstituted the detected ER proportion. In contrast, overexpression of disease-related truncated *FAM134B* mutant proteins S309X and Q145X (introduced in chapter 3.2.1) as well as the LIR-motif deficient mutant *FAM134B* variant were unable to re-establish the normal ER size (Khaminets et al. 2015). Thus, a functional importance of *FAM134B* in controlling the size of the ER was suggested. This hypothesis was enormously supported by ultrastructural changes detected in *Fam134b* knockout mouse sensory neurons showing ER and Golgi compartment alterations that were discussed in section 6.2. Remarkably, the findings of our study (Khaminets et al. 2015) are in agreement with previous reports linking a proper ER morphology with the long-term maintenance of highly polarized neurons. Especially proteins that contribute to the shaping of the neuronal ER are associated with a huge number of neurological diseases. For instance the group of hereditary spastic paraplegias (HSPs) affect particularly long-projecting upper motoneurons (Renvoise and Blackstone 2010).

Notably, within the present study we identified the capability of Fam134b to specifically bind to LC3-like modifier proteins by a conserved LIR motif. For the recovery of ER compartment size by re-expression of Fam134b in knockdown cells, the LIR motif was indispensable. Hence, the interaction with LC3-like modifiers is obligatory for the cellular mechanism underlying Fam134b-mediated ER regulation. More evidence for this assumption was obtained by immunocytochemic analysis of starved MEF cells which were transfected with a tagged wild-type *FAM134B* construct or a respective mutant LIR version (see Figure 27). Based on the observation that starvation-induced HA-*FAM134B* puncta co-localized both with the tubular ER marker Reticulon 4 (Rtn4) and GFP-LC3, a Fam134b-mediated degradation of ER fragments by the autophagosomal pathway was suggested. This was further supported by the observation that the LIR-mutant *FAM134B* did not co-localize with GFP-LC3 puncta and Rtn4. Hence, the LIR mutant *FAM134B* was unable to sequester ER

fragments into autophagosomes. However, it should be considered that overexpression may generate artifacts especially when studying autophagic pathways. For this reason, endogenous levels of the ER compartment marker Rtn4 were analyzed to increase the reliability of the observed effects on autophagosomal ER degradation. Further, a cellular model with stable and moderate expression of tagged LC3 may be recommended for future work.

In summary, the key features of an autophagy receptor that simultaneously binds to the designated cargo and LC3-like modifiers (Stolz et al. 2014) are provided in the case of Fam134b. Selective ER-targeting to autophagosomes has been proposed already (Hamasaki et al. 2004, Lipatova and Segev 2015), but Fam134b might be the first identified autophagy receptor for this process. In parallel, two autophagy receptor proteins facilitating selective ER-phagy processes in yeast were identified by Mochida et.al. (2015).

6.5 Molecular mechanisms involved in Fam134b-mediated HSAN

The results of this study provide important insights into pathogenetic pathways that may contribute to the human sensory neuropathy caused by *Fam134b* loss-of-function mutations. Fam134b specifically interacts with LC3-like modifiers via a conserved LIR motif and possesses membrane bending properties. Functional impairments of autophagy and membrane-shaping have been linked with neurodegenerative diseases by various studies which were published in the last years (Renvoise and Blackstone 2010, Hübner and Kurth 2014, Yamamoto and Simonsen 2011, Frake et al. 2015, Kroemer 2015, Beetz et al. 2013).

In respect to the HSAN2B pathogenesis, it remains to be elucidated if both the loss of LC3-interaction and membrane curvature function of Fam134b are relevant for the disease mechanism. In this context, membrane remodeling processes are considered as crucial for autophagic pathways; thus, membrane bending by the reticulon-like hairpin topology of Fam134b might be helpful in scission of ER fragments which are targeted in turn for autophagosomal degradation. Likewise, other proteins involved in autophagy accomplish dual functions, such as GATE-16. Initially GATE-16 was characterized as Golgi apparatus-resident protein that interacts with SNAREs to modulate intra-Golgi transport (Sagiv et al. 2000). Later GATE-16 was found to belong to the group of LC3-like modifiers mediating autophagosome maturation (Weidberg et al. 2010).

Both disease-related FAM134B mutants lack the conserved LIR motif, but only the Q145X version lacks parts of the reticulon domain. Accordingly, *in vitro* liposome shaping was impaired for the Q145X mutant, whereas the ability to shape membranes was preserved for

the S309X mutant (Khaminets et al. 2015). In conclusion, the pathomechanism of HSAN2B may be related to a loss of FAM134B-LC3 interactions via the LIR domain.

Mouse sensory neurons deficient for Fam134b showed ultrastructural changes of the reticular compartment even before phenotypic disease onset. Together with the findings discussed in the previous section this proposes a mechanism involving impaired ER-selective autophagy, in short 'ER-phagy'. In yeast, ER-phagic processes are described as adaptive responses counteracting UPR-related ER proliferation (Bernales et al. 2006b). In this context, pathways independent from the core autophagic machinery and autophagosome formation, but equivalent to microautophagy are reported (Schuck et al. 2014). Moreover, ER sequestration into autophagosomes requiring the function of macroautophagic core players and distinct selective autophagy receptors, was currently demonstrated in yeast (Mochida et al. 2015).

Various stressors are known to activate different modes of autophagic processes, so autophagy integrates into multiple stress responding adaptive pathways. This might explain why defects in autophagy reduce the cellular resistance to stress (Kroemer et al. 2010). The UPR as a major ER stress pathway activates PERK, IRE1 and ATF6 (as introduced in section 3.3.3). Notably, all of those pathways are involved in signaling cascades that could promote autophagy (Sica et al. 2015). Further, ER stress responses itself trigger both pro-survival and pro-apoptotic cascades. Either cell survival or death is favoured according to the severity and duration of stressors and is mediated by differential stability of signaling mRNA or proteins (Rutkowski et al. 2006). In parallel, autophagy is strongly crosslinked to apoptotic pathways and may prevent or contribute to programmed cell death (Maiuri et al. 2007). In respect to a disturbed ER-phagy due to Fam134b loss-of-function, DRG sensory neurons may be unable to cope with physiological stressors that accumulate during ageing.

Adaptive autophagy attempting to re-establish ER homeostasis may be activated by an increased abundance of cargo (Sica et al. 2015). Deficient ER-degradation caused by Fam134b dysfunction, promotes sustained ER stress and may finally lead to apoptosis (Walter and Ron 2011). Hereby, the different branches of UPR such as IRE1-mediated Caspase-12 activation or downregulation of pro-survival factors (Tabas and Ron 2011) might be involved. In summary, Fam134b-mediated ER-phagy seems particularly important to maintain highly polarized and long-living cells. Prolonged ER-stress signaling due to impaired adaptive ER-selective degradation may be causative of the observed sensory dysfunction and axonal loss. Generally, our findings suggest a role for defective ER-phagy implicated in neuro-

degenerative disease mechanisms. In this context, Fam134b complements the growing list of autophagy receptor proteins.

6.6 Conclusion and further perspectives

The present work proposes that impaired ER-selective autophagy (ER-phagy) underlies HSN2B pathology. Figure 28 illustrates how Fam134b may regulate the homeostasis of the ER by specific interaction with LC3-like modifiers. The conserved LC3-interacting region (LIR) ensures the proper targeting to autophagosome-anchored LC3. Conclusively, it is hypothesized that Fam134b protein acts as ER-specific autophagy receptor protein, thereby regulating ER turnover. Functional assays addressing ER turnover have provided strong evidence for selective autophagosome-mediated ER degradation which is termed ‘ER-phagy’. It might be speculated if such processes are likewise existent at Golgi membrane sites.

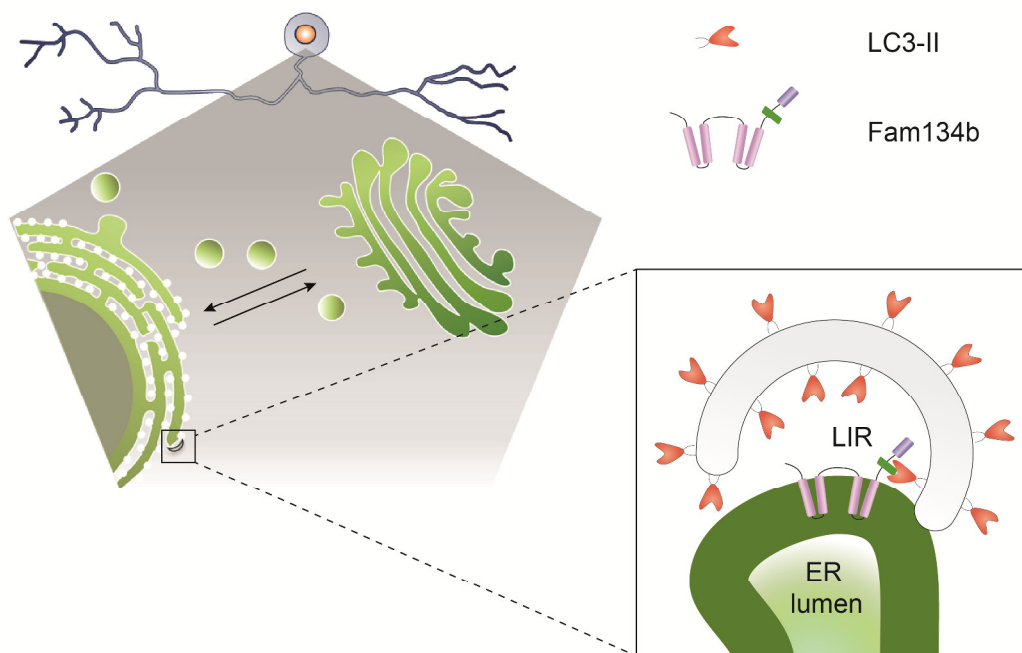


Figure 28: Fam134b protein might function as ER-specific autophagy receptor

Loss of Fam134b was shown to predominantly affect sensory neuron function in our knockout mouse model. In detail, the ultrastructure of endoplasmic reticulum (ER) and Golgi apparatus showed dilated tubules and stacks, respectively. The Fam134b protein localizes to both compartments and due to its reticulon-like topology might be enriched at high curvature membrane sites. The C-terminally LC3-interacting region (LIR) of Fam134b efficiently binds to LC3-like modifier proteins which are present at autophagosomal membrane structures. Thereby, Fam134b is hypothesized to selectively target ER membranes into autophagosomes for degradation.

Beyond the action of Fam134b which was examined by the work of this thesis, both Fam134a and Fam134c possess a conserved LIR motif. Accordingly, both of them might have similar capabilities to act as autophagy receptor and may be interesting to study.

Further questions that should be addressed by future work include: How is ER-phagy induced via Fam134b in detail? Which molecular players are involved in the recruitment of the phagophore and what regulates Fam134b-driven ER-phagy according to the variable cellular demands to keep the organellar homeostasis? Generally autophagy receptors are often regulated by multiple post-translational modifications (Stolz et al. 2014, Chen et al. 2014), so their detection by e.g. mass spectrometry may hint for mechanisms of Fam134b regulation.

How is Fam134b involved in adaptive signaling for the maintenance of cellular functions in response to certain stressors? In this context, it would be worth to resolve the time- and dose-dependency of stressors that trigger Fam134b-mediated adaptive responses. For this purpose, different ER stressors may be applied and cell viability could be determined.

Moreover, not much is known about autophagosome generation in DRG sensory neurons. Reports suggest an autophagosome generation preferentially at the distal ends of DRG axons. (Maday and Holzbaur 2014). This raises the question about distinct sites of Fam134b-related autophagosome generation in DRG sensory neurons.

Further it was shown recently that actin polymerization contributes to autophagosome formation and is a driving force for the assembly of mature autophagosomal vesicles (Holland and Simonsen 2015). So there is good reason to investigate if Fam134b interacts with the actin-network especially under conditions of starvation or ER-stress.

Additionally, the results of our study do not fully explain the occurrence of drastically swollen Golgi cisternae in DRG neurons of affected mice. To date, no pathways that suggest the selective degradation of the Golgi apparatus in autophagosomes have been revealed. However, the ER-Golgi-intermediate compartment (ERGIC) was identified as a source for pre-autophagosomal structures (Ge et al. 2013). For this reason, it could be planned to clarify if Fam134b promotes selective degradation of Golgi apparatus fragments similar as shown for the ER (Khaminets et al. 2015).

Taken together, it is of high relevance to entirely understand how adaptive networks interplay to keep the cellular homeostasis. Thus, the identification of Fam134b as molecular player for selective cargo targeting to autophagosomes and its impact in the neurodegeneration of sensory neurons, made a little contribution to this huge field of research.

References

- Appenzeller-Herzog C, Hauri H-PP. 2006. The ER-Golgi intermediate compartment (ERGIC): in search of its identity and function. *Journal of cell science*, 119 (Pt 11):2173-2183.
- Auer-Grumbach M. 2013. Hereditary sensory and autonomic neuropathies. *Handbook of clinical neurology*, 115:893-906.
- Aydinlar E, Rolfs A, Serteser M, Parman Y. 2014. Mutation in FAM134B causing hereditary sensory neuropathy with spasticity in a Turkish family. *Muscle & nerve*, 49 (5):774-775.
- Barth S, Glick D, Macleod KF. 2010. Autophagy: assays and artifacts. *The Journal of pathology*, 221 (2):117-124.
- Baumann O, Walz B. 2001. Endoplasmic reticulum of animal cells and its organization into structural and functional domains. *International review of cytology*, 205:149-214.
- Beetz C, Koch N, Khundadze M, Zimmer G, Nietzsche S, Hertel N, Huebner AK, Mumtaz R, Schweizer M, Dirren E, Karle KN, Irintchev A, Alvarez V, Redies C, Westermann M, Kurth I, Deufel T, Kessels MM, Qualmann B, Hubner CA. 2013. A spastic paraplegia mouse model reveals REEP1-dependent ER shaping. *J Clin Invest*, 123 (10):4273-4282.
- Bernales S, Papa FR, Walter P. 2006a. Intracellular signaling by the unfolded protein response. *Annual review of cell and developmental biology*, 22:487-508.
- Bernales S, McDonald K, Walter P. 2006b. Autophagy counterbalances endoplasmic reticulum expansion during the unfolded protein response. *PLoS biology*, 4 (12).
- Birgisdottir ÁBB, Lamark T, Johansen T. 2013. The LIR motif - crucial for selective autophagy. *Journal of cell science*, 126 (Pt 15):3237-3247.
- Bjørkøy G, Lamark T, Pankiv S, Øvervatn A, Brech A, Johansen T. 2009. Monitoring autophagic degradation of p62/SQSTM1. *Methods in enzymology*, 452:181-197.
- Bjørkøy G, Lamark T, Brech A, Outzen H, Perander M, Overvatn A, Stenmark H, Johansen T. 2005. p62/SQSTM1 forms protein aggregates degraded by autophagy and has a protective effect on huntingtin-induced cell death. *The Journal of cell biology*, 171 (4):603-614.
- Boland B, Kumar A, Lee S, Platt FM, Wegiel J, Yu WH, Nixon RA. 2008. Autophagy induction and autophagosome clearance in neurons: relationship to autophagic pathology in Alzheimer's disease. *The Journal of neuroscience : the official journal of the Society for Neuroscience*, 28 (27):6926-6937.
- Boya P, González-Polo R-AA, Casares N, Perfettini J-LL, Dessen P, Larochette N, Métivier D, Meley D, Souquere S, Yoshimori T, Pierron G, Codogno P, Kroemer G. 2005. Inhibition of macroautophagy triggers apoptosis. *Molecular and cellular biology*, 25 (3):1025-1040.
- Cain DM, Khasabov SG, Simone DA. 2001. Response properties of mechanoreceptors and nociceptors in mouse glabrous skin: an in vivo study. *Journal of neurophysiology*, 85 (4):1561-1574.
- Cebollero E, Reggiori F, Kraft C. 2012. Reticulophagy and ribophagy: regulated degradation of protein production factories. *International journal of cell biology*, vol. 2012, Article ID 182834.
- Chen G, Han Z, Feng D, Chen Y, Chen L, Wu H, Huang L, Zhou C, Cai X, Fu C, Duan L, Wang X, Liu L, Liu X, Shen Y, Zhu Y, Chen Q. 2014. A regulatory signaling loop

- comprising the PGAM5 phosphatase and CK2 controls receptor-mediated mitophagy. *Mol Cell*, 54 (3):362-377.
- Condon KH, Ho J, Robinson CG, Hanus C, Ehlers MD. 2013. The Angelman syndrome protein Ube3a/E6AP is required for Golgi acidification and surface protein sialylation. *The Journal of neuroscience : the official journal of the Society for Neuroscience*, 33 (9):3799-3814.
- Conforti L, Gilley J, Coleman MP. 2014. Wallerian degeneration: an emerging axon death pathway linking injury and disease. *Nature Reviews Neuroscience*, 15 (6):394-409.
- Cuervo AM, Wong E. 2014. Chaperone-mediated autophagy: roles in disease and aging. *Cell research*, 24 (1):92-104.
- Davidson GL, Murphy SM, Polke JM, Laura M, Salih MAM, Muntoni F, Blake J, Brandner S, Davies N, Horvath R, Price S, Donaghy M, Roberts M, Foulds N, Ramdharry G, Soler D, Lunn MP, Manji H, Davis MB, Houlden H, Reilly MM. 2012. Frequency of mutations in the genes associated with hereditary sensory and autonomic neuropathy in a UK cohort. *Journal of neurology*, 259 (8):1673-1685.
- Day KJ, Staehelin LA, Glick BS. 2013. A three-stage model of Golgi structure and function. *Histochemistry and cell biology*, 140 (3):239-249.
- Dyck PJ, Chance P, Lebo R, Carney J. 1993. Hereditary motor and sensory neuropathies. *Neurology*, 39:1302-1308.
- Farquhar MG, Palade GE. 1981. The Golgi apparatus (complex)-(1954-1981)-from artifact to center stage. *The Journal of cell biology*, 91 (3):77-103.
- Frake RA, Ricketts T, Menzies FM, Rubinsztein DC. 2015. Autophagy and neurodegeneration. *The Journal of clinical investigation*, 125 (1):65-74.
- Freedman RB. 1989. Protein disulfide isomerase: multiple roles in the modification of nascent secretory proteins. *Cell*, 57 (7):1069-1072.
- Ge L, Melville D, Zhang M, Schekman R. 2013. The ER-Golgi intermediate compartment is a key membrane source for the LC3 lipidation step of autophagosome biogenesis. *eLife*, 2.
- Gonatas NK, Stieber A, Gonatas JO. 2006. Fragmentation of the Golgi apparatus in neurodegenerative diseases and cell death. *Journal of the neurological sciences*, 246 (1-2):21-30.
- Griffiths G, Simons K. 1986. The trans Golgi network: sorting at the exit site of the Golgi complex. *Science*, 234 (4775):438-443.
- Gu F, Crump CM, Thomas G. 2001. Trans-Golgi network sorting. *Cellular and molecular life sciences: CMLS*, 58 (8):1067-1084.
- Hailey DW, Rambold AS, Satpute-Krishnan P, Mitra K, Sougrat R, Kim PK, Lippincott-Schwartz J. 2010. Mitochondria supply membranes for autophagosome biogenesis during starvation. *Cell*, 141 (4):656-667.
- Hamasaki M, Noda T, Baba M, Ohsumi Y. 2004. Starvation triggers the delivery of the endoplasmic reticulum to the vacuole via autophagy in yeast. *Traffic*, 6 (1):56-65.
- Hauri HP, Kappeler F, Andersson H, Appenzeller C. 2000. ERGIC-53 and traffic in the secretory pathway. *Journal of cell science*, 113 (Pt 4):587-596.
- Hayashi-Nishino M, Fujita N, Noda T, Yamaguchi A, Yoshimori T, Yamamoto A. 2009. A subdomain of the endoplasmic reticulum forms a cradle for autophagosome formation. *Nature cell biology*, 11 (12):1433-1437.
- Hirano M, Nakamura Y, Saigoh K, Sakamoto H, Ueno S, Isono C, Miyamoto K, Akamatsu M, Mitsui Y, Kusunoki S. 2013. Mutations in the gene encoding p62 in Japanese patients with amyotrophic lateral sclerosis. *Neurology*, 80 (5):458-463.

- Holland P, Simonsen A. 2015. Actin shapes the autophagosome. *Nature cell biology*, 17:1094-1096.
- Hosokawa N, Hara T, Kaizuka T, Kishi C, Takamura A, Miura Y, Iemura S-i, Natsume T, Takehana K, Yamada N, Guan J-LL, Oshiro N, Mizushima N. 2009. Nutrient-dependent mTORC1 association with the ULK1-Atg13-FIP200 complex required for autophagy. *Molecular biology of the cell*, 20 (7):1981-1991.
- Hsu VW, Lee SY, Yang JS. 2009. The evolving understanding of COPI vesicle formation. *Nat Rev Mol Cell Biol*, 10 (5):360-364.
- Hu J, Shibata Y, Zhu P-PP, Voss C, Rismanchi N, Prinz WA, Rapoport TA, Blackstone C. 2009. A class of dynamin-like GTPases involved in the generation of the tubular ER network. *Cell*, 138 (3):549-561.
- Hübner CA, Kurth I. 2014. Membrane-shaping disorders: a common pathway in axon degeneration. *Brain*, 137 (Pt 12):3109-3121.
- Hughes R. 2008. Peripheral nerve diseases: the bare essentials. *Practical neurology*, 8 (6):396-405.
- Ichimura Y, Kirisako T, Takao T, Satomi Y, Shimonishi Y, Ishihara N, Mizushima N, Tanida I, Kominami E, Ohsumi M, Noda T, Ohsumi Y. 2000. A ubiquitin-like system mediates protein lipidation. *Nature*, 408 (6811):488-492.
- Jahn R, Scheller RH. 2006. SNAREs--engines for membrane fusion. *Nature reviews Molecular cell biology*, 7 (9):631-643.
- Johansen T, Lamark T. 2011. Selective autophagy mediated by autophagic adapter proteins. *Autophagy*, 7 (3):279-296.
- Kasem K, Gopalan V, Salajegheh A, Lu C-TT, Smith RA, Lam AK. 2014. The roles of JK-1 (FAM134B) expressions in colorectal cancer. *Experimental cell research*, 326 (1):166-173.
- Kaur J, Debnath J. 2015. Autophagy at the crossroads of catabolism and anabolism. *Nature reviews Molecular cell biology*, 16 (8):461-472.
- Khaminets A, Heinrich T, Mari M, Grumati P, Huebner AK, Akutsu M, Liebmann L, Stolz A, Nietzsche S, Koch N, Mauthe M, Katona I, Qualmann B, Weis J, Reggiori F, Kurth I, Hübner CA, Dikic I. 2015. Regulation of endoplasmic reticulum turnover by selective autophagy. *Nature*, 522 (7556):354-358.
- Klionsky DJ, Cregg JM, Dunn WA, Emr SD, Sakai Y, Sandoval IV, Sibirny A, Subramani S, Thumm M, Veenhuis M, Ohsumi Y. 2003. A unified nomenclature for yeast autophagy-related genes. *Developmental cell*, 5 (4):539-545.
- Klopfenstein DR, Klumperman J, Lustig A, Kammerer RA, Oorschot V, Hauri HP. 2001. Subdomain-specific localization of CLIMP-63 (p63) in the endoplasmic reticulum is mediated by its luminal alpha-helical segment. *The Journal of cell biology*, 153 (6):1287-1300.
- Komatsu M, Waguri S, Chiba T, Murata S, Iwata J-i, Tanida I, Ueno T, Koike M, Uchiyama Y, Kominami E, Tanaka K. 2006. Loss of autophagy in the central nervous system causes neurodegeneration in mice. *Nature*, 441 (7095):880-884.
- Komatsu M, Waguri S, Ueno T, Iwata J, Murata S, Tanida I, Ezaki J, Mizushima N, Ohsumi Y, Uchiyama Y, Kominami E, Tanaka K, Chiba T. 2005. Impairment of starvation-induced and constitutive autophagy in Atg7-deficient mice. *The Journal of cell biology*, 169 (3):425-434.
- Kong M, Kim Y, Lee C. 2011. A strong synergistic epistasis between FAM134B and TNFRSF19 on the susceptibility to vascular dementia. *Psychiatric genetics*, 21 (1):37-41.

- Korolchuk VI, Menzies FM, Rubinsztein DC. 2010. Mechanisms of cross-talk between the ubiquitin-proteasome and autophagy-lysosome systems. *FEBS letters*, 584 (7):1393-1398.
- Kroemer G. 2015. Autophagy: a druggable process that is deregulated in aging and human disease. *The Journal of clinical investigation*, 125 (1):1-4.
- Kroemer G, Mariño G, Levine B. 2010. Autophagy and the integrated stress response. *Molecular cell*, 40 (2):280-293.
- Kuma A, Hatano M, Matsui M, Yamamoto A, Nakaya H, Yoshimori T, Ohsumi Y, Tokuhiya T, Mizushima N. 2004. The role of autophagy during the early neonatal starvation period. *Nature*, 432 (7020):1032-1036.
- Kurth I, Pamminger T, Hennings JC, Soehendra D, Huebner AK, Rotthier A, Baets J, Senderek J, Topaloglu H, Farrell SA, Nürnberg G, Nürnberg P, De Jonghe P, Gal A, Kaether C, Timmerman V, Hübner CA. 2009. Mutations in FAM134B, encoding a newly identified Golgi protein, cause severe sensory and autonomic neuropathy. *Nature genetics*, 41 (11):1179-1181.
- Le Bars D, Gozariu M, Cadden SW. 2001. Animal models of nociception. *Pharmacol Rev*, 53 (4):597-652.
- Lee AS. 2005. The ER chaperone and signaling regulator GRP78/BiP as a monitor of endoplasmic reticulum stress. *Methods (San Diego, Calif)*, 35 (4):373-381.
- Linstedt AD, Foguet M, Renz M, Seelig HP, Glick BS, Hauri HP. 1995. A C-terminally-anchored Golgi protein is inserted into the endoplasmic reticulum and then transported to the Golgi apparatus. *Proceedings of the National Academy of Sciences of the United States of America*, 92 (11):5102-5105.
- Lipatova Z, Segev N. 2015. A Role for Macro-ER-Phagy in ER Quality Control. *PLoS genetics*, 11 (7).
- Lippincott-Schwartz J, Roberts TH, Hirschberg K. 2000. Secretory protein trafficking and organelle dynamics in living cells. *Annual review of cell and developmental biology*, 16:557-589.
- Liu L, Feng D, Chen G, Chen M, Zheng Q, Song P, Ma Q, Zhu C, Wang R, Qi W, Huang L, Xue P, Li B, Wang X, Jin H, Wang J, Yang F, Liu P, Zhu Y, Sui S, Chen Q. 2012. Mitochondrial outer-membrane protein FUNDC1 mediates hypoxia-induced mitophagy in mammalian cells. *Nat Cell Biol*, 14 (2):177-185.
- Lorenz H, Hailey DW, Wunder C, Lippincott-Schwartz J. 2006. The fluorescence protease protection (FPP) assay to determine protein localization and membrane topology. *Nature protocols*, 1 (1):276-279.
- Lynes EM, Simmen T. 2011. Urban planning of the endoplasmic reticulum (ER): how diverse mechanisms segregate the many functions of the ER. *Biochimica et biophysica acta*, 1813 (10):1893-1905.
- Maday S, Holzbaur EL. 2014. Autophagosome biogenesis in primary neurons follows an ordered and spatially regulated pathway. *Developmental cell*, 30 (1):71-85.
- Maiuolo J, Bulotta S, Verderio C, Benfante R, Borgese N. 2011. Selective activation of the transcription factor ATF6 mediates endoplasmic reticulum proliferation triggered by a membrane protein. *Proceedings of the National Academy of Sciences of the United States of America*, 108 (19).
- Maiuri MC, Zalckvar E, Kimchi A, Kroemer G. 2007. Self-eating and self-killing: crosstalk between autophagy and apoptosis. *Nature reviews Molecular cell biology*, 8 (9):741-752.
- Martyn CN, Hughes RA. 1997. Epidemiology of peripheral neuropathy. *Journal of Neurology, Neurosurgery & Psychiatry*, 62 (4):310-318.

- Maruyama H, Kawakami H. 2013. Optineurin and amyotrophic lateral sclerosis. *Geriatrics & gerontology international*, 13 (3):528-532.
- Mason JM, Arndt KM. 2004. Coiled coil domains: stability, specificity, and biological implications. *Chembiochem : a European journal of chemical biology*, 5 (2):170-176.
- Maxfield FR, McGraw TE. 2004. Endocytic recycling. *Nature reviews Molecular cell biology*, 5 (2):121-132.
- Mizushima N, Komatsu M. 2011. Autophagy: renovation of cells and tissues. *Cell*, 147 (4):728-741.
- Mizushima N, Yamamoto A, Matsui M, Yoshimori T, Ohsumi Y. 2004. In vivo analysis of autophagy in response to nutrient starvation using transgenic mice expressing a fluorescent autophagosome marker. *Molecular biology of the cell*, 15 (3):1101-1111.
- Mochida K, Oikawa Y, Kimura Y, Kirisako H, Hirano H, Ohsumi Y, Nakatogawa H. 2015. Receptor-mediated selective autophagy degrades the endoplasmic reticulum and the nucleus. *Nature*, 522 (7556):359-362.
- Moscat J, Diaz-Meco MTT, Wooten MW. 2007. Signal integration and diversification through the p62 scaffold protein. *Trends in biochemical sciences*, 32 (2):95-100.
- Mulder GB, Pritchett K. 2004. Rodent analgesiometry: the hot plate, tail flick and Von Frey hairs. *Contemporary topics in laboratory animal science / American Association for Laboratory Animal Science*, 43 (3):54-55.
- Munro S, Pelham HR. 1986. An Hsp70-like protein in the ER: identity with the 78 kd glucose-regulated protein and immunoglobulin heavy chain binding protein. *Cell*, 46 (2):291-300.
- Murphy SMM, Davidson GL, Brandner S, Houlden H, Reilly MM. 2012. Mutation in FAM134B causing severe hereditary sensory neuropathy. *Journal of neurology, neurosurgery, and psychiatry*, 83 (1):119-120.
- Nakamura N, Rabouille C, Watson R, Nilsson T, Hui N, Slusarewicz P, Kreis TE, Warren G. 1995. Characterization of a cis-Golgi matrix protein, GM130. *The Journal of cell biology*, 131 (6 Pt 2):1715-1726.
- Nakatogawa H, Suzuki K, Kamada Y, Ohsumi Y. 2009. Dynamics and diversity in autophagy mechanisms: lessons from yeast. *Nature reviews Molecular cell biology*, 10 (7):458-467.
- Novak I, Kirkin V, McEwan DG, Zhang J, Wild P, Rozenknop A, Rogov V, Löhr F, Popovic D, Occhipinti A, Reichert AS, Terzic J, Dötsch V, Ney PA, Dikic I. 2010. Nix is a selective autophagy receptor for mitochondrial clearance. *EMBO reports*, 11 (1):45-51.
- Ogata M, Hino S-i, Saito A, Morikawa K, Kondo S, Kanemoto S, Murakami T, Taniguchi M, Tanii I, Yoshinaga K, Shiosaka S, Hammarback JA, Urano F, Imaizumi K. 2006. Autophagy is activated for cell survival after endoplasmic reticulum stress. *Molecular and cellular biology*, 26 (24):9220-9231.
- Ohashi Y, Munro S. 2010. Membrane delivery to the yeast autophagosome from the Golgi-endosomal system. *Molecular biology of the cell*, 21 (22):3998-4008.
- Okunade GW, Miller ML, Azhar M, Andringa A, Sanford LP, Doetschman T, Prasad V, Shull GE. 2007. Loss of the Atp2c1 secretory pathway Ca(2+)-ATPase (SPCA1) in mice causes Golgi stress, apoptosis, and midgestational death in homozygous embryos and squamous cell tumors in adult heterozygotes. *The Journal of biological chemistry*, 282 (36):26517-26527.
- Orso G, Pendin D, Liu S, Tosetto J, Moss TJ, Faust JE, Micaroni M, Egorova A, Martinuzzi A, McNew JA, Daga A. 2009. Homotypic fusion of ER membranes requires the dynamin-like GTPase atlastin. *Nature*, 460 (7258):978-983.

- Pendin D, McNew JA, Daga A. 2011. Balancing ER dynamics: shaping, bending, severing, and mending membranes. *Current opinion in cell biology*, 23 (4):435-442.
- Pickford F, Masliah E, Britschgi M, Lucin K, Narasimhan R, Jaeger PA, Small S, Spencer B, Rockenstein E, Levine B, Wyss-Coray T. 2008. The autophagy-related protein beclin 1 shows reduced expression in early Alzheimer disease and regulates amyloid beta accumulation in mice. *The Journal of clinical investigation*, 118 (6):2190-2199.
- Praefcke GJ, McMahon HT. 2004. The dynamin superfamily: universal membrane tubulation and fission molecules? *Nature reviews Molecular cell biology*, 5 (2):133-147.
- Puhka M, Vihinen H, Joensuu M, Jokitalo E. 2007. Endoplasmic reticulum remains continuous and undergoes sheet-to-tubule transformation during cell division in mammalian cells. *The Journal of cell biology*, 179 (5):895-909.
- Puhka M, Joensuu M, Vihinen H, Belevich I, Jokitalo E. 2012. Progressive sheet-to-tubule transformation is a general mechanism for endoplasmic reticulum partitioning in dividing mammalian cells. *Molecular biology of the cell*, 23 (13):2424-2432.
- Ravikumar B, Moreau K, Jahreiss L, Puri C, Rubinsztein DC. 2010. Plasma membrane contributes to the formation of pre-autophagosomal structures. *Nature cell biology*, 12 (8):747-757.
- Renvoise B, Blackstone C. 2010. Emerging themes of ER organization in the development and maintenance of axons. *Current opinion in neurobiology*, 20 (5).
- Robbins E, Gonatas NK. 1964. The ultrastructure of a mammalian cell during the mitotic cycle. *The Journal of cell biology*, 21:429-463.
- Robinson MS. 1990. Cloning and expression of gamma-adaptin, a component of clathrin-coated vesicles associated with the Golgi apparatus. *The Journal of cell biology*, 111 (6 Pt 1):2319-2326.
- Rogov V, Dotsch V, Johansen T, Kirkin V. 2014. Interactions between autophagy receptors and ubiquitin-like proteins form the molecular basis for selective autophagy. *Molecular cell*, 53 (2):167-78.
- Ron D. 2002. Translational control in the endoplasmic reticulum stress response. *The Journal of clinical investigation*, 110 (10):1383-1388.
- Rotthier A, Baets J, Timmerman V, Janssens K. 2012. Mechanisms of disease in hereditary sensory and autonomic neuropathies. *Nature reviews Neurology*, 8 (2):73-85.
- Rutkowski DT, Arnold SM, Miller CN, Wu J, Li J, Gunnison KM, Mori K, Sadighi Akha AA, Raden D, Kaufman RJ. 2006. Adaptation to ER stress is mediated by differential stabilities of pro-survival and pro-apoptotic mRNAs and proteins. *PLoS biology*, 4 (11):e374.
- Sagiv Y, Legesse-Miller A, Porat A, Elazar Z. 2000. GATE-16, a membrane transport modulator, interacts with NSF and the Golgi v-SNARE GOS-28. *The EMBO journal*, 19 (7):1494-1504.
- Sahu R, Kaushik S, Clement CC, Cannizzo ES, Scharf B, Follenzi A, Potolicchio I, Nieves E, Cuervo AM, Santambrogio L. 2011. Microautophagy of cytosolic proteins by late endosomes. *Developmental cell*, 20 (1):131-139.
- Schuck S, Gallagher CM, Walter P. 2014. ER-phagy mediates selective degradation of endoplasmic reticulum independently of the core autophagy machinery. *Journal of cell science*, 127 (Pt 18):4078-4088.
- Shibata Y, Hu J, Kozlov MM, Rapoport TA. 2009. Mechanisms shaping the membranes of cellular organelles. *Annual review of cell and developmental biology*, 25:329-354.
- Shibata Y, Shemesh T, Prinz W, Palazzo A, Kozlov M, Rapoport T. 2010. Mechanisms determining the morphology of the peripheral ER. *Cell*, 143 (5):774-88.

- Shibata Y, Voss C, Rist JM, Hu J, Rapoport TA, Prinz WA, Voeltz GK. 2008. The reticulon and DP1/Yop1p proteins form immobile oligomers in the tubular endoplasmic reticulum. *The Journal of biological chemistry*, 283 (27):18892-18904.
- Sica V, Galluzzi L, Bravo-San Pedro JMM, Izzo V, Maiuri MC, Kroemer G. 2015. Organelle-Specific Initiation of Autophagy. *Molecular cell*, 59 (4):522-539.
- Sou Y-sS, Waguri S, Iwata J-i, Ueno T, Fujimura T, Hara T, Sawada N, Yamada A, Mizushima N, Uchiyama Y, Kominami E, Tanaka K, Komatsu M. 2008. The Atg8 conjugation system is indispensable for proper development of autophagic isolation membranes in mice. *Molecular biology of the cell*, 19 (11):4762-4775.
- Stolz A, Ernst A, Dikic I. 2014. Cargo recognition and trafficking in selective autophagy. *Nature cell biology*, 16 (6):495-501.
- Tabas I, Ron D. 2011. Integrating the mechanisms of apoptosis induced by endoplasmic reticulum stress. *Nature cell biology*, 13 (3):184-190.
- Taichi H, Kenji N, Makoto M, Akitsugu Y, Yohko N, Rika S-M, Minesuke Y, Kenji M, Ichiro S, Hideyuki O, Noboru M. 2006. Suppression of basal autophagy in neural cells causes neurodegenerative disease in mice. *Nature*, 441 (7095):885-889.
- Tan C-CC, Yu J-TT, Tan M-SS, Jiang T, Zhu X-CC, Tan L. 2014. Autophagy in aging and neurodegenerative diseases: implications for pathogenesis and therapy. *Neurobiology of aging*, 35 (5):941-957.
- Tang WK, Chui CH, Fatima S, Kok SH, Pak KC, Ou TM, Hui KS, Wong MM, Wong J, Law S, Tsao SW, Lam KY, Beh PS, Srivastava G, Chan AS, Ho KP, Tang JC. 2007. Oncogenic properties of a novel gene JK-1 located in chromosome 5p and its overexpression in human esophageal squamous cell carcinoma. *International journal of molecular medicine*, 19 (6):915-923.
- Teyssou E, Takeda T, Lebon V, Boillée S, Doukouré B, Bataillon G, Sazdovitch V, Cazeneuve C, Meininger V, LeGuern E, Salachas F, Seilhean D, Millecamps S. 2013. Mutations in SQSTM1 encoding p62 in amyotrophic lateral sclerosis: genetics and neuropathology. *Acta neuropathologica*, 125 (4):511-522.
- Truett GE, Heeger P, Mynatt RL, Truett AA, Walker JA, Warman ML. 2000. Preparation of PCR-quality mouse genomic DNA with hot sodium hydroxide and tris (HotSHOT). *BioTechniques*, 29 (1):52-54.
- van de Velde HJ, Roebroek AJ, Senden NH, Ramaekers FC, Van de Ven WJ. 1994. NSP-encoded reticulons, neuroendocrine proteins of a novel gene family associated with membranes of the endoplasmic reticulum. *Journal of cell science*, 107 (Pt 9):2403-2416.
- van der Vaart A, Griffith J, Reggiori F. 2010. Exit from the Golgi is required for the expansion of the autophagosomal phagophore in yeast *Saccharomyces cerevisiae*. *Molecular biology of the cell*, 21 (13):2270-2284.
- Voeltz G, Prinz W, Shibata Y, Rist J, Rapoport T. 2006. A class of membrane proteins shaping the tubular endoplasmic reticulum. *Cell*, 124 (3):573-86.
- Voeltz GK, Prinz WA. 2007. Sheets, ribbons and tubules - how organelles get their shape. *Nature reviews Molecular cell biology*, 8 (3):258-264.
- von Muhlinen N, Akutsu M, Ravenhill BJ, Foeglein Á, Bloor S, Rutherford TJ, Freund SM, Komander D, Randow F. 2012. LC3C, bound selectively by a noncanonical LIR motif in NDP52, is required for antibacterial autophagy. *Molecular cell*, 48 (3):329-342.
- Walsh ME, Sloane LB, Fischer KE, Austad SN, Richardson A, Remmen HV. 2014. Use of Nerve Conduction Velocity to Assess Peripheral Nerve Health in Aging Mice. *The Journals of Gerontology Series A: Biological Sciences and Medical Sciences*, 70 (11):1312-1319).

- Walter P, Ron D. 2011. The unfolded protein response: from stress pathway to homeostatic regulation. *Science*, 334 (6059):1081-1086.
- Wang M, Wey S, Zhang Y, Ye R, Lee AS. 2009. Role of the unfolded protein response regulator GRP78/BiP in development, cancer, and neurological disorders. *Antioxidants & redox signaling*, 11 (9):2307-2316.
- Weidberg H, Shvets E, Elazar Z. 2011. Biogenesis and cargo selectivity of autophagosomes. *Annual review of biochemistry*, 80:125-156.
- Weidberg H, Shvets E, Shpilka T, Shimron F, Shinder V, Elazar Z. 2010. LC3 and GATE-16/GABARAP subfamilies are both essential yet act differently in autophagosome biogenesis. *The EMBO journal*, 29 (11):1792-1802.
- Wen T, Ansonoff MA, Pintar JE. 2009. The tail pigmentation pattern of C57BL/6J mice affects nociception/pain quantification in the tail flick test. *European journal of pain (London, England)*, 13 (6):564-567.
- Yamamoto A, Simonsen A. 2011. The elimination of accumulated and aggregated proteins: a role for autophagy in neurodegeneration. *Neurobiology of disease*, 43 (1):17-28.
- Yan R, Shi Q, Hu X, Zhou X. 2006. Reticulon proteins: emerging players in neurodegenerative diseases. *Cellular and molecular life sciences: CMLS*, 63 (7-8):877-889.
- Yang Z, Klionsky DJ. 2010. Eaten alive: a history of macroautophagy. *Nature cell biology*, 12 (9):814-822.
- Yen W-LL, Shintani T, Nair U, Cao Y, Richardson BC, Li Z, Hughson FM, Baba M, Klionsky DJ. 2010. The conserved oligomeric Golgi complex is involved in double-membrane vesicle formation during autophagy. *The Journal of cell biology*, 188 (1):101-114.
- Zhang C, Kho Y-SS, Wang Z, Chiang YT, Ng GK, Shaw P-CC, Wang Y, Qi RZ. 2014. Transmembrane and coiled-coil domain family 1 is a novel protein of the endoplasmic reticulum. *PloS one*, 9 (1):e85206.

Appendix Figures

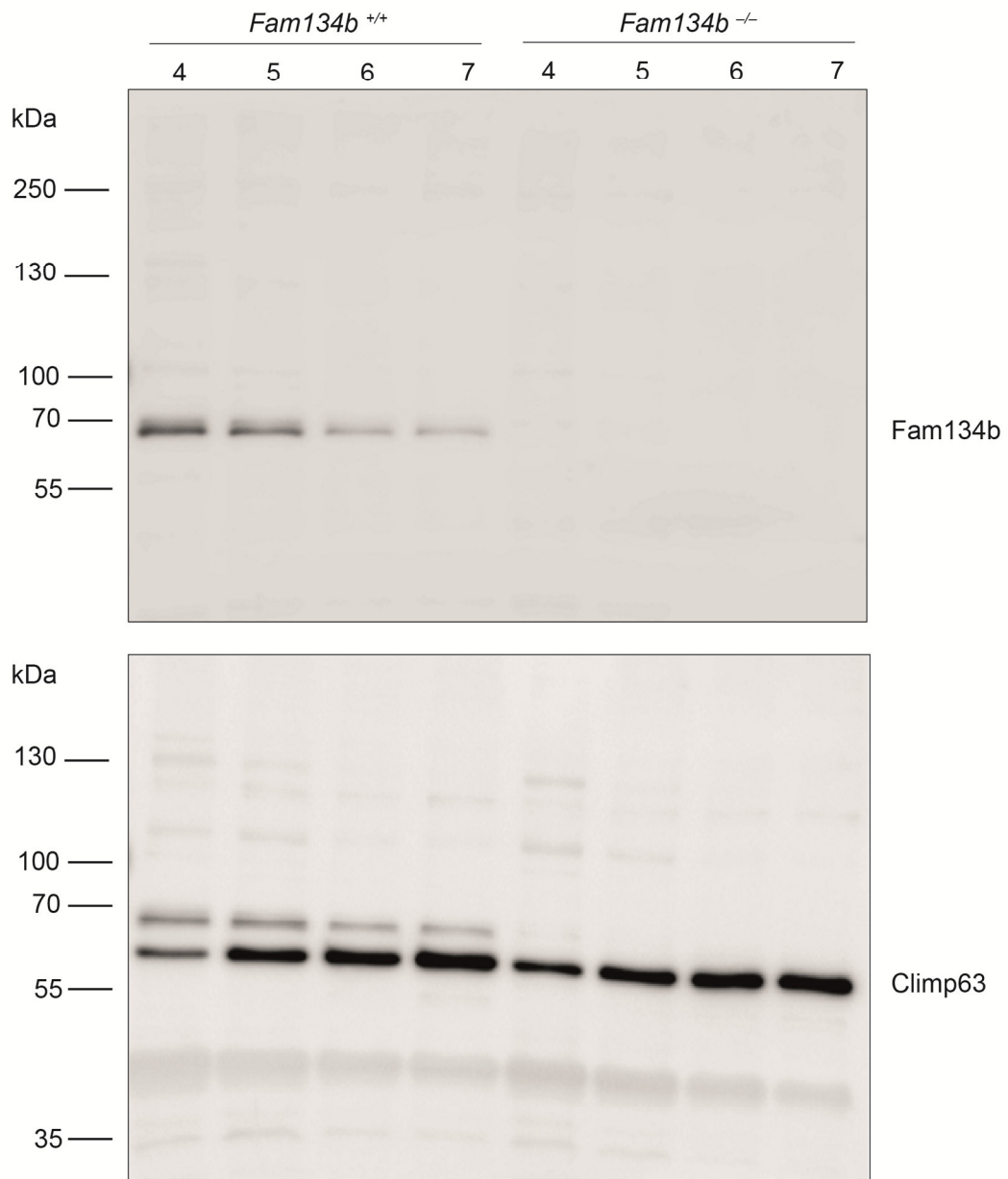


Figure 29: Control blot for subcellular ER-Golgi fractions

In respect to the blot shown in Figure 17 to study Fam134b's subcellular localization, subcellular fractions of wild-type (*Fam134b*^{+/+}) and knockout (*Fam134b*^{-/-}) mouse brain were loaded in an additional experiment on one common SDS-gel to exactly verify the absence of the Fam134b protein band in fractions obtained from knockout brain. Fraction samples of number 4, 5, 6, and 7 of the discontinuous iodixanol gradient (2.5-30%) were separated by SDS-PAGE, transferred to a PVDF membrane and incubated with Fam134b-specific antibody. A subsequent reprobing of the membrane with Climp63-specific antibody gave prove of the presence of comparable amounts of protein in the same number of fraction of wild-type and knockout samples, respectively.

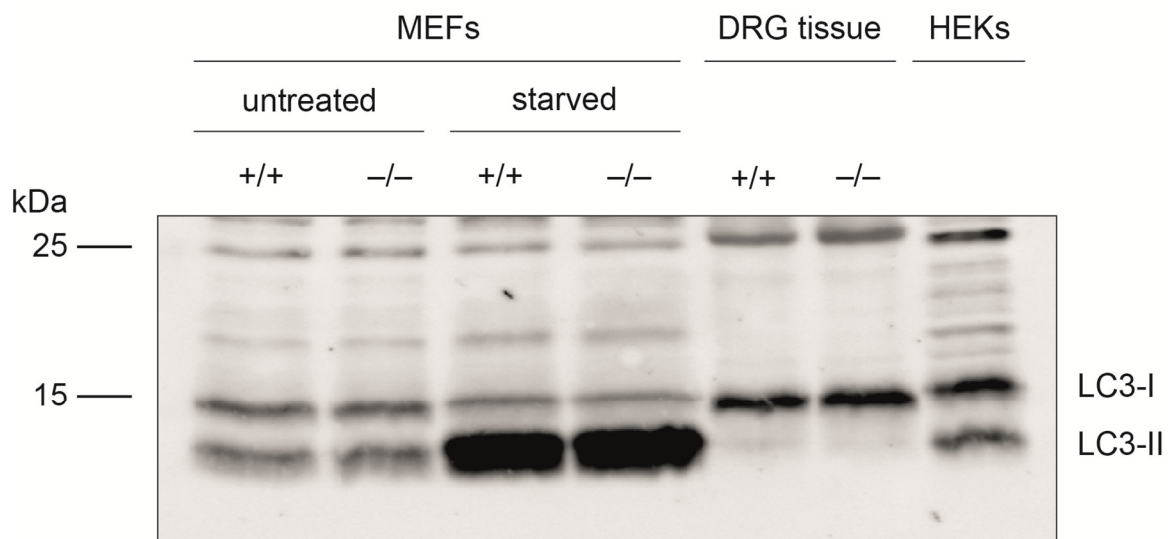


Figure 30: Control blot for LC3 protein expression analysis

Western blot analysis of LC3 protein in lysates of mouse embryonic fibroblasts (MEFs), DRG and brain tissue from wild-type (+/+) and knockout (-/-) mice and of Chloroquine-treated (50 μ M, O/N) HEK293T cells. Protein samples were subjected to SDS-PAGE (15% gel) and processed for immunoblot analysis with antibodies specific for LC3B, which is usually detected both as cytosolic LC3-I protein band and as faster running processed and lipidated LC3-II. In respect of the LC3 bands which are illustrated in Figure 25, this experiment was planned to ensure that LC3-II is not detectable in DRG mouse tissue. For this purpose, MEF cells were starved prior cell lysis to induce LC3-II protein that is present at autophagosomal membranes. Additionally, HEK293T cells that had treated with Chloroquine were loaded on the same gel as positive control for the presence of LC3-II.

Index of Figures

Figure 1: Afferent sensory fiber dysfunction in hereditary sensory and autonomic neuropathies.....	5
Figure 2: Clinical features of FAM134B-mediated HSAN2B	7
Figure 3: Predicted FAM134B protein topology.....	8
Figure 4: Vesicular trafficking between the endomembrane compartments.....	9
Figure 5: Autophagosome formation and initiation in macroautophagic pathways	13
Figure 6: Selective types of autophagy involve autophagy receptor protein function	15
Figure 7: Knockout strategy for <i>Fam134b</i> transgenic mouse generation	19
Figure 8: Protein expression of Fam134b in mouse embryonic fibroblasts.....	32
Figure 9: Sensory function in <i>Fam134b</i> -deficient mice.....	33
Figure 10: Quantification of afferent sensory axon number.....	35
Figure 11: Ultrastructural analysis of DRG somata from mouse tissue sections	36
Figure 12: Ultrastructural analysis of DRG somata from primary neuronal cultures	37
Figure 13: Efferent motor fiber function assessed by CMAP latency.....	38
Figure 14: Ventral horn motor neuron histology and quantification.....	39
Figure 15: Ultrastructural analysis of motoneurons in spinal cord sections	40
Figure 16: Subcellular distribution of immunofluorescent HA-tagged FAM134B ...	42
Figure 17: Subcellular fractionation studies of the ER and Golgi compartment.....	43
Figure 18: FAM134B-LC3 protein interaction studies by co-immunoprecipitation..	45
Figure 19: Multisequence alignment of the LIR motif present in Fam134 proteins ..	46
Figure 20: Co-localization studies of FAM134B and autophagosomes.....	47
Figure 21: FAM134B topology studies by assaying fluorescence protein protection	48
Figure 22: <i>In vitro</i> liposome shaping assay	49
Figure 23: Protein expression studies in mouse neuronal tissue	50
Figure 24: p62-protein expression monitored in DRG cryosections.....	51
Figure 25: Protein expression of LC3 and Grp78 in mouse neuronal tissue.....	52
Figure 26: Protein expression of Fam134b, GM130, Climp63 and LC3 in MEFs	53
Figure 27: Protein co-localization studies of FAM134B, Rtn4 and autophagosomes.....	55
Figure 28: FAM134B protein might function as ER-specific autophagy receptor	65
Figure 29: Control blot for subcellular ER-Golgi fractions	XIII
Figure 30: Control blot for LC3 protein expression analysis	XIV

Index of Tables

Table 1: Cultivated eukaryotic cell lines.....	18
Table 2: List of DNA plasmids.....	19
Table 3: List of commercial primary antibodies.....	19

Ehrenwörtliche Erklärung

Hiermit erkläre ich, dass mir die Promotionsordnung der Medizinischen Fakultät der Friedrich-Schiller-Universität bekannt ist,

ich die Dissertation selbst angefertigt habe und alle von mir benutzten Hilfsmittel, persönlichen Mitteilungen und Quellen in meiner Arbeit angegeben sind,

mich folgende Personen bei der Auswahl und Auswertung des Materials sowie bei der Herstellung des Manuskripts unterstützt haben: Prof. Dr. C.A. Hüber, PD Dr. I. Kurth, Dr. L. Liebmann, Dr. J.C. Hennings,

die Hilfe eines Promotionsberaters nicht in Anspruch genommen wurde und dass Dritte weder unmittelbar noch mittelbar geldwerte Leistungen von mir für Arbeiten erhalten haben, die im Zusammenhang mit dem Inhalt der vorgelegten Dissertation stehen,

dass ich die Dissertation noch nicht als Prüfungsarbeit für eine staatliche oder andere wissenschaftliche Prüfung eingereicht habe und

dass ich die gleiche, eine in wesentlichen Teilen ähnliche oder eine andere Abhandlung nicht bei einer anderen Hochschule als Dissertation eingereicht habe.

Jena, 26.05.2016

Ort, Datum

Unterschrift des Verfassers

Curriculum Vitae

ZUR PERSON

Geboren: 17.10.1987 in Karl-Marx-Stadt

AKADEMISCHER WERDEGANG

Friedrich-Schiller Universität Jena 01/2012 – heute

Promotionsstudium zum doctor rerum naturalium (Dr. rer. nat.)

- Teilnahme am DFG-geförderten Graduiertenprogramm:
Research Training Group 1715: Molecular signatures of adaptive stress responses

Friedrich-Schiller Universität Jena 10/2009 – 10/2011

Master of Science (M.Sc.), Molecular Medicine

- Thema der Abschlussarbeit:
PTEN oxidation in FLT3 ITD-expressing cells and mechanisms underlying FLT3 ITD-induced ROS-production

Technische Universität Dresden 10/2006 – 09/2009

Bachelor of Science (B.Sc.), Molekulare Biotechnologie

- Thema der Abschlussarbeit:
Mechanismen der Regulation der Genexpression von Trefoil Factor 1 in MCF-7-Zellen durch selektive Östrogenrezeptor-Modulatoren und Phytoöstrogene

SCHULISCHE AUSBILDUNG

Albert-Schweitzer-Gymnasium in Limbach-Oberfrohna 08/1998 – 07/2006

Abitur (Note: 1,3)

ENGAGEMENT

Biotechnologischen Studenteninitiative (btS) e.V. 06/2011 – heute

Aktive btS-Mitgliedschaft

DFG-gefördertes Graduiertenkolleg RTG1715 01/2012 – 09/2015

Ehrenamtliche Sprechertätigkeit

Dr. FSU - der Doktorandenrat der FSU Jena 12/2013 – 09/2014

Ehrenamtliche Gremienarbeit

Akademisches Auslandsamt der TU Dresden
Tutorin

10/2008 – 08/2009

Fachschaftsrat (FSR) Biologie und Studentenrat der TU Dresden
Ehrenamtliche Gremienarbeit

11/2007 – 10/2008

BESONDERE KENNTNISSE

Zertifikat in Versuchstierkunde: Teilnahme am Übungskurs zum Erlernen tierexperimenteller Methoden an Maus und Ratte (Re.-Nr.02-109/12)

WISSENSCHAFTLICHE PUBLIKATIONEN

Heinrich T, Hübner CA, Kurth I.

Isolation and Primary Cell Culture of Mouse Dorsal Root Ganglion Neurons

Bio-protocol 6(7): e1785.

Khaminets A*, Heinrich T*, Mari M, Grumati P, Huebner AK, Akutsu M, Liebmann L, Stolz A, Nietzsche S, Koch N, Mauthe M, Katona I, Qualmann B, Weis J, Reggiori F, Kurth I, Hübner CA, Dikic I. (*co-first authors)

Regulation of endoplasmic reticulum turnover by selective autophagy.

Nature. 2015, 522(7556):354-8.

Leipold E, Liebmann L, Korenke GC, Heinrich T, Gießelmann S, Baets J, Ebbinghaus M, Goral RO, Stöckberg T, Hennings JC, Bergmann M, Altmüller J, Thiele H, Wetzel A, Nürnberg P, Timmerman V, De Jonghe P, Blum R, Schaible HG, Weis J, Heinemann SH, Hübner CA, Kurth I.

A de novo gain-of-function mutation in SCN11A causes loss of pain perception.

Nature Genetics. 2013, 45:1399-1404.

Godfrey R, Arora D, Bauer R, Stopp S, Müller JP, Heinrich T, Böhmer SA, Dagnell M, Schnetzke U, Scholl S, Ostman A, Böhmer FD.

Cell transformation by FLT3 ITD in acute myeloid leukemia involves oxidative inactivation of the tumor suppressor protein-tyrosine phosphatase DEP-1/ PTPRJ.

Blood. 2012 119(19):4499-511.

Jena, 26.05.2016

Danksagung

Herrn Prof. C.A. Hübner danke ich für die Überlassung des Themas, die vielen Ratschläge und Anregungen sowie für die ausgezeichneten Arbeitsmöglichkeiten in den Laboratorien des Institutes für Humangenetik des Universitätsklinikums der FSU Jena.

Bei Herrn PD Dr. Ingo Kurth möchte ich mich für die Betreuung, seine Geduld und die ständige Hilfs- und Diskussionsbereitschaft bedanken.

Außerdem danke ich Herrn Prof. R. Wetzker, für die Zusammenarbeit und die Begutachtung der Dissertation, die im Rahmen der DFG-geförderten „Research Training Group 1715“ angefertigt worden ist.

Mein ganz besonderer Dank gilt allen Mitarbeitern der Arbeitsgruppe „Funktionelle Genetik“. Ich danke Antje, Lutz und Christopher für die große Unterstützung bei allen wissenschaftlichen und technischen Fragestellungen. Ebenso danke ich Dir - Christoph - für deine Hilfe insbesondere zu Beginn meiner Zeit am Institut. Nicht zuletzt danke ich Melanie und Martin für Motivation, Ablenkung und Freundschaft. Ebenso herzlich danke ich Katrin, Sebastian, Mukhran und Hartmut, auf deren Hilfe ich mich immer verlassen konnte. Allen weiteren Mitgliedern unserer Arbeitsgruppe sei ebenfalls für die Zusammenarbeit und das freundliche Arbeitsklima gedankt.

Desweiteren bedanke ich mich bei allen Kooperationspartnern und allen nicht namentlich aufgeführten Mitarbeitern des Instituts für Humangenetik. Allen RTG-Doktoranden gebührt Dank für die angenehme Atmosphäre bei unseren Seminaren, Workshops und gemeinsamen Ausflügen.

Von ganzem Herzen danke ich abschließend meiner Familie, insbesondere meinen Eltern, sowie Nico und meinen Freunden wie beispielsweise Jenny und Anne, für ihre unendliche Geduld und liebevolle Unterstützung.

„Leider läßt sich eine wahrhafte Dankbarkeit mit Worten nicht ausdrücken.“

Johann Wolfgang von Goethe